A search for optical counterparts of the complex Vela X system

Enos Takalani Marubini, B.Sc. (Hons.)

Dissertation submitted in partial fulfilment of the requirements for the degree Master of Science in Physics at the Potchefstroom Campus of the North-West University

Supervisor: Dr. R. R. Sefako
Co-supervisor: Dr. C. Venter

December 2012

Acknowledgement

First of all I would like to thank God.
I would like to extend my gratitude to my supervisors Dr. R.R. Sefako and Dr. C. Venter for their time, commitment and positive support contributing to the success of this dissertation. I also acknowledge the NRF for their financial support, and thank the support staff at the Centre for Space Research for the warm welcome I have received from day one. I would also like to thank Prof. Okkie de Jager who agreed to work with me, although God remembered him before the completion of the dissertation. *"May his soul rest in peace"*. I would furthermore like to thank the SAAO staff for my stay during the observations and for the use of the SAAO 1.0 m telescope. Thanks to Jaco Mentz who performed the optical observations in 2010. I thank my mother, Mrs. T.E. Marubini, for her encouragement and support. My brothers: Joseph, Freddy, Aaron, and Fhulufhelo – thank you for being there and for your concern regarding my progress. Fulufhedzani Ramalisa and Unarine Marubini, you stood by me during hard times and difficult situations. I would like to thank the Potchefstroom Student Christian Fellowship (PSCF), colleagues and friends. Lastly, I would like to thank my friends Dr. M.P. Mulaudzi, Edwin Magidimisha, and Bothwell Nyoni.

Abstract

The pulsar wind nebula (PWN) associated with the Vela pulsar, Vela X, is a complex system visible in radio, X-ray and γ-ray wavelengths, but not in the optical wavelength. Knowledge of the brightness and structure of the PWN in optical is important in order to constrain the morphology as well as the underlying particle spectrum, the B-field properties, and particle energy losses associated with this extended source. Optical observations of the Vela X system at Sutherland with the SAAO 1.0 m telescope did not yield any significant detection. Similar observations with *HST, NTT,* and *VLT* could only give upper limits to the surface brightness in the vicinity of this system (Mignani et al., 2003). Since we find no visible optical counterparts to the PWN radio lobes within the field of view of our observations, we are inhibited from probing the change in source morphology as a function of energy. Using all these observations mentioned above, we investigate whether or not the radio synchrotron component can be smoothly extrapolated to the optical band, which would have implications for the particle injection spectrum. We derive νF_ν upper limits of $\sim 10^{-7}$ erg s^{-1} cm^{-2} for the B and V bands from Sutherland observations. We find that our upper limits do not constrain any broadband spectral model for Vela X. The question of whether the underlying particle injection spectrum consists of a single component or multiple components could therefore not be fully addressed. Deeper optical observations, specifically targeting the cocoon region southwest of the pulsar, may yet detect a very faint optical source and therefore may advance our understanding of this complex multiwavelength object.

Keywords: pulsar wind nebulae — pulsars — supernova remnants — Vela X — optical observations — SAAO 1.0 m telescope

Opsomming

Die pulsarwindnewel (PWN) wat met die Vela pulsar geassosieer word, Vela X, is n ingewikkelde sisteem wat sigbaar is in radio-, X-straal-, en gammastraal-golflengtes, maar nie in die optiese band nie. Dit is belangrik om die helderheid en struktuur van hierdie PWN te ondersoek, aangesien dit beperkinge kan plaas op die morfologie, onderliggende deeltjiespektrum, eienskappe van die B-veld, asook die deeltjie-energieverliese van hierdie uitgebreide bron. Optiese waarnemings van die Vela X sisteem by Sutherland met die SAAO 1.0 m teleskoop het nie n beduidende ontdekking tot gevolg gehad nie. Soortgelyke waarnemings met *HST, NTT* en *VLT* kon slegs bogrense lewer m.b.t. die oppervlakhelderheid in die omgewing van hierdie sisteem (Mignani et al., 2003). Omdat ons geen optiese ewebeeld vir die PWN radio-lobbe binne die sigveld van ons waarnemings vind nie, kan ons nie die verandering in bronmorfologie as funksie van energie bestudeer nie. Deur van al hierdie waarnemings gebruik te maak, het ons ondersoek ingestel of die radio-sinkrotronkomponent glad gekstrapoleer kan word tot die optiese band. Dit sou implikasies sou h vir die deeltjie-insetspektrum. Ons het bogrense van $\nu F_\nu \sim 10^{-7}$ erg s^{-1} cm^{-2} vir die B- en V-bande van ons Sutherland-waarnemings afgelei. Ons vind dat ons bogrense geen beperking plaas op enige breband-model vir Vela X nie. Die vraag of die onderliggende deeltjie-insetspektrum uit een of meer komponente bestaan kon dus nie volledig aangespreek word nie. Dieper optiese waarnemings wat spesifiek op die kokon-gebied suidwes van die pulsar fokus, mag moontlik n dowwe optiese bron waarneem en daardeur ons begrip van hierdie ingewikkelde multigolflengte-voorwerp uitbrei.

Sleutelwoorde: pulsarwindnewels pulsare supernovareste Vela X optiese waarnemings SAAO 1.0 m teleskoop

Nomenclature

ATCA	Australia Telescope Compact Array
ACIS	Advanced CCD Imaging Spectrometer
ASCA	Advanced Satellite for Cosmology and Astrophysics
AGILE	Astro-rivelatore Gamma a Immagini Leggero
CANGAROO	Collaboration of Australia and Nippon (Japan) for a Gamma Ray Observatory in the Outback
CCD	Charged coupled device
CGRO	Compton Gamma Ray Observatory
CMB	Cosmic microwave background
CTA	Cherenkov Telescope Array
DSS	Digital Sky Survey
EM	Electromagnetic
EUV	Extreme ultraviolet
FUV	Far ultraviolet
FUSE	Far Ultraviolet Spectroscopic Explorer
HE	High energy
HEAO	High Energy Astrophysics Observatory
H.E.S.S.	High Energy Stereoscopic System
HST	Hubble Space Telescope
IC	Inverse Compton
IR	Infrared
IPC	Imaging Proportional Counter
ISM	Interstellar medium
LAT	Large Area Telescope
LEDs	Low-energy detectors
MHD	Magnetohydrodynamic
MOST	Molongo Observatory Synthesis Telescope
NS	Neutron star
NTT	New Technology Telescope
NUV	Near ultraviolet
OSSE	Oriented Scintillation Spectrometer Experiment
PWN	Pulsar wind nebula
PSF	Point spread function
PSPC	Position Sensitive Proportional Counter
ROSAT	Röntgen Satellite
SAAO	South African Astronomical Observatory
SED	Spectral energy distribution
SPEAR	Spectroscopy of Plasma Evolution from Astrophysical Radiation

SNR	Supernova remnant
SR	Synchrotron radiation
SSAS	Second Small Astronomy Satellite
SSC	Synchrotron Self-Compton
SSI	Sky Survey Instrument
UV	Ultraviolet
VHE	Very high energy
VLT	Very Large Telescope
WMAP	Wilkinson Microwave Anistropy Probe

Contents

List of Figures

List of Tables

Chapter 1

Introduction

Pulsar wind nebulae (PWNe) are composed of charged particles that have been accelerated to relativistic speeds inside the embedded pulsar's magnetosphere, as well as at the termination shock formed by the wind of outflowing particles. The particles next interact with the ambient magnetic and soft photon fields, and radiate across the electromagnetic (EM) spectrum (see Section 1.4 and Section 1.5). A particularly intriguing and nearby example is Vela X, which is the subject of this dissertation. The High Energy Stereoscopic System (H.E.S.S.) has uncovered nearly 70 very-high-energy (VHE) sources, 34 of them being PWNe, including Vela X (Wakely & Horan, 2012). In the high-energy (HE) band, *Fermi Large Area Telescope (LAT)* has firmly identified four PWNe: (1) the Crab Nebula, (2) Vela X, (3) the PWN inside MSH15−52, and (4) HESS J1825−137, and plausibly also HESS J1023−5746 (Ackermann et al., 2011; Nolan et al., 2012). Vela X has also been observed in the radio, X-ray, and infrared (IR) bands (see Chapter 2). Notably, optical detection of Vela X is still lacking (Section 1.6).

In this chapter, we provide a brief overview of several topics relevant to our study of the Vela X plerion. First, we review stellar evolution (Section 1.1), followed by supernovae (SNe) and supernova remnants (SNRs, Section 1.2) including their creation, classification and evolution. Next we discuss pulsars (Section 1.3) as well as PWNe (Section 1.4), including their formation characteristics and evolution, followed by an overview of relevant radiation mechanisms (Section 1.5), including synchrotron radiation (SR) and inverse Compton scattering (ICS). Lastly, we discuss our problem statement (Section 1.6), as well as our aims and objectives (Section 1.7), and give an outline of the rest of the dissertation (Section 1.8).

1.1 Stellar Evolution

In the study of the structure and evolution of stars, there are three phases that are to be considered: (1) Formation of stars of different masses from the gas in the interstellar medium (ISM); (2) structural changes in the star as the nuclear reactions that power the star evolve in time; and (3) end products of stellar evolution after they have reached a steady state (Padmanabhan, 2001).

Stars are formed by mass accumulation and eventually gravitational collapse, which occurs when density perturbations in the natal cloud become unstable. In protostar formation, the Jeans model relies on gravitational instabilities to initiate collapse. The Jeans mass $M_{\rm J}$ separates configurations that are stable ($M_{\rm J} > M$) from those that are unstable ($M > M_{\rm J}$). From Newtonian theory, $M_{\rm J}$ can be expressed as (Bowers & Deeming, 1984)

$$M_{\rm J} = \left(\frac{4\pi m_{\rm H} n}{3}\right)\left(\frac{\pi v_{\rm s}}{G\rho}\right)^{3/2}, \tag{1.1}$$

where n is the total baryon number density, $v_{\rm s}$ is the local adiabatic speed of sound, and ρ is the mass density. In other words, a cloud of mass M can be condensed provided its average density exceeds the Jeans density (Phillips, 1997)

$$\rho_{\rm J} = \frac{3}{4\pi M^2}\left(\frac{3kT}{2G\bar{m}}\right)^3, \tag{1.2}$$

where $\bar{m}$ is average stellar mass.

The structure of the star must evolve over time scales comparable with the thermonuclear reaction time scale. The essential ingredients of stellar evolution are the following: (1) exhaustion of the nuclear fuel in the stellar core; (2) contraction of the core; (3) expansion of the envelope; and (4) degenerate or nondegenerate burning of fuel in the core and in the shell. The evolution of the main sequence stars consists of the gradual conversion of hydrogen to helium in the stellar cores, along with slow expansion of the stars (for high-mass stars). The core temperature rises during the compressional heating and ignite hydrogen-burning thermonuclear reactions. As the process continues the star reaches a state where the energy lost to radiation is balanced by that produced by the thermonuclear burning of hydrogen (Hartle, 2003). The conversion of hydrogen into helium is reflected by a 'motion' of the star to the left and upwards in the Hertzsprung-Russell (HR) diagram (luminosity versus temperature; see, e.g., Tayler, 1994).

The proton-proton chain operating in low-mass stars has a relatively low temperature sensitivity, so that the radius changes gradually compared to that of high-mass stars. The core contracts, the envelope expands, with the temperature being sufficient to ignite a helium shell, and a helium flash occurs. During this process, the helium combustion stabilizes in the core (Padmanabhan, 2001). Eventually a significant fraction of the hydrogen in the core of the star is exhausted and there is no longer enough thermonuclear fuel to compensate for the energy lost to radiation. Compression ensues, and the core temperature rises until the reaction which burns helium to make other elements, ignites.

In addition, stars may also fuse hydrogen into helium using the carbon-nitrogen-oxygen (CNO) cycle. The CNO cycle starts with a carbon nucleus and transforms it into a nitrogen nucleus. This is in turn transformed into an oxygen nucleus, and then back to a carbon nucleus. In the end, carbon remains unchanged, but during this process four hydrogen nuclei are fused to make a helium nucleus, plus energy, similar to the case of the proton-proton chain. The CNO cycle requires a temperature higher than $\sim 2 \times 10^7$ K because it starts with a carbon nucleus combining with a hydrogen nucleus (having a relatively high Coulomb barrier due to its higher charge compared to that of a hydrogen atom) (Seeds & Backman, 2008). After the star has converted some of its hydrogen into helium, a discontinuity of chemical composition may result and the star may become a red giant, until the mixing currents made the star homogeneous (Tayler, 1994).

Heavy-element fusion happens when the star has exhausted its hydrogen fuel and fuses other types of nuclear fuel such as helium and carbon. Since these nuclei have higher positive charges, their Coulomb barriers are even higher, and for the nuclear reaction to take place, a temperature

of $\sim 10^8$ K is required. A helium nucleus is called an alpha particle, and these reactions are known as the triple-alpha process, since they involve three helium nuclei (Seeds & Backman, 2008).

The life of a star is characterised by the contracting force of gravity and the expansion forces (radiation pressure) of gases which are heated by reactions that form nuclei and in the process release energy. After some time the helium will be exhausted. Compressional heating will lead to a new stage of thermonuclear burning. The fusion process cannot continue indefinitely. Iron (^{56}Fe) has the highest binding energy per nucleon. The nuclei of iron or others near it can therefore not be burned (fused) to release energy. The iron peak nuclei are thus the ashes of thermonuclear burning (Hartle, 2003).

The study of stellar evolution has revealed that stellar end products differ in nature, depending on the mass of the star. These are as follows: (1) white dwarfs; (2) neutron stars (NSs); and (3) black holes (Padmanabhan, 2001).

Theoretical models show that a star that begins its life with a mass as much as ~ 8 solar masses should lose mass fast enough to reduce this to below 1.4 solar masses (the Chandrasekar limit, which is the maximum mass that can be supported by degenerate electron pressure) and will eventually collapse to form a white dwarf. White dwarf stars are very hot and have a very low luminosity, implying that they have a small surface area. The size of a white dwarf is comparable to that of the earth, with a density of about 2×10^6 g cm^{-3}. Degenerate matter is a very good conductor of heat, so as the heat flows to the surface and escapes into space, the white dwarf becomes fainter and cooler, and finally moves downwards to the right in the HR diagram.

If a star ends up being heavier than 1.4 solar masses, degenerate electron pressure cannot maintain a steady state, and degenerate neutron pressure provides the stabilizing force, forming a NS. Cameron (1959) integrated the general relativistic equations of hydrodynamic equilibrium neutron gas. His results showed that there was an upper limit of about 2 solar masses, and the corresponding upper limit to the proper mass is about 3 solar masses, for the maximum mass of a NS. He also found a lower limit of about 0.05 solar masses, below which the NS is unstable against transformation into an iron star. An NS is therefore a star of about 1 to 2 solar masses compressed into a radius of about 10 km, with a high density such that the matter is stable only as a fluid of neutrons (Padmanabhan, 2001).

Black holes form when the star's nuclear fuel is exhausted, and the eventual stellar mass exceeds ~ 2 solar masses, so that neither electron nor neutron degenerate pressure can support the star against gravitational collapse. Black holes are singularities in spacetime from which nothing can escape, not even light (classically speaking;Hartle, 2003). The size of a black hole depends on the mass of the collapsed object. The Schwarzschild radius is defined by

$$R_{\rm sch} = \frac{2GM}{c^2}, \tag{1.3}$$

and sets the distance to the black hole's event horizon, a one-way surface beyond which no matter or photons can escape. For example, for a collapsed star with mass equal to 10 solar masses, the Schwarzschild radius is 30 km. The accretion of matter into a black hole is accompanied by X-ray radiation (Phillips, 1997).

Interestingly, Stephen Hawking in 1974 discovered that black holes shine like a blackbody with a temperature inversely proportional to their mass, when invoking the annihilation of particles and antiparticles close to the event horizon, being created from the zero energy vacuum of empty space

during quantum fluctuations. This temperature ($T_{\rm BH}$) is very small and negligible for solar mass size and supermassive black holes (Hartle, 2003):

$$T_{\rm BH} = 6.2 \times 10^{-8} \left(\frac{M_\odot}{M} \right) \text{ K}. \tag{1.4}$$

1.2 Supernovae and Supernova Remnants

Some of the most energetic explosive events known in the universe are SNe. SNe represent a transitional phase in a star's life. SNe play a central role in modern astrophysics, as they are important for the chemical evolution of the universe, as well as being sources of energy for the ISM. SNe are divided into two categories according the explosion process in which they originate: (1) core-collapse SNe; and (2) thermonuclear SNe (Vink, 2012). A core-collapse SN occurs when a supergiant star collapses suddenly at the end of its life. The elements expected in the core of the star and outer layers are: iron-group elements, as well as silicon group elements at the core, and oxygen, neon, magnesium, carbon, helium, as well as unprocessed hydrogen-rich material in the outer layers. Conversely, thermonuclear SNe are due to stars with masses close to the Chandrasekhar limit, meaning that the explosion energy originates from explosive nuclear burning rather than gravitational energy liberated during the collapse of a stellar core. While many SNRs have been observed in nearby galaxies, SNe are relatively rare events in our own galaxy: only 2–3 occur per century (Van den Bergh & McClure, 1994).

SNRs are classified based on their morphology and are grouped into three classes: (1) shell-type SNRs, where the morphology is characterised by a limb brightening shell; (2) plerions, where the nebular morphology is bright in the centre, and does not show a shell; and (3) composite SNRs, where energetic pulsars with ages less than $\sim$ 20 000 yr are expected to have blown a PWN, while they are still surrounded by the SNR shell (Vink, 2012).

1.2.1 Creation of an SNR

Core collapse occurs at the end of a massive star's (e.g., main sequence stars with masses of about 8 solar masses) life. Before it collapses, the star consists of different layers containing the products of the different consecutive nuclear burning stages. Gravitational collapse happens when a star's nuclear fuel is exhausted and it is no longer supported against gravity by the release of nuclear energy. If the star is particularly massive, its core will collapse, during which process the star will release a huge amount of energy (Vink, 2012). SNe are therefore extremely luminous and cause a burst of radiation that often briefly outshines an entire galaxy, before fading from view over several weeks or months. During this short interval, an SN can radiate as much energy as the Sun is expected to emit over its entire life span (Giacobbe, 2005). The explosion expels much or all of a star's material at a velocity of up to 30 000 km/s (10% of the speed of light), causing a blast wave that ejects the star's envelope into interstellar space (Schawinski et al., 2008). This shock wave sweeps up an expanding shell of gas and dust which is called an SNR (Vink, 2012).

In contrast to core-collapse SNe, in thermonuclear SNe the explosion energy derives from explosive nuclear burning occurring in Type Ia systems (Section 1.2.2) rather than from gravitational collapse. A white dwarf star may accumulate sufficient material from a stellar companion (either through accretion or via a merger) to raise its core temperature enough to ignite carbon fusion, at which point it undergoes runaway nuclear fusion, completely disrupting it. The models for

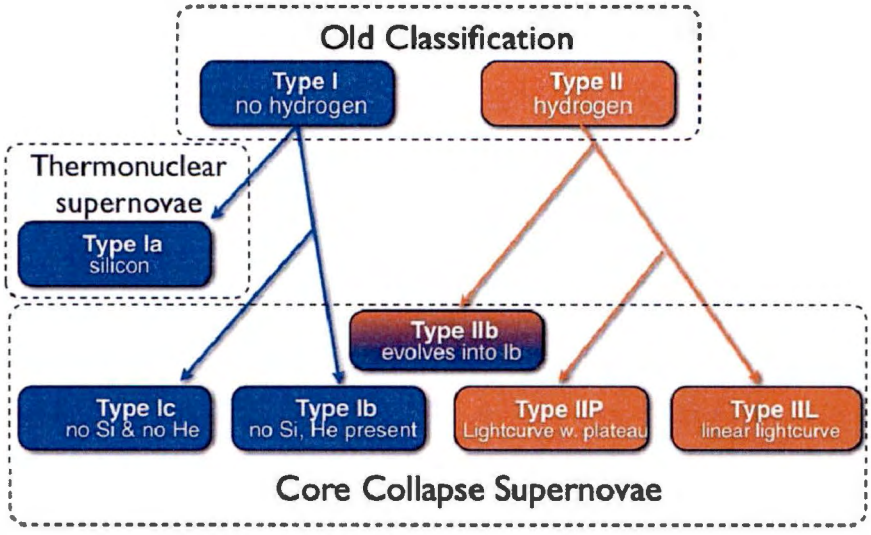

Figure 1.1: Classification of SNe based on their optical spectroscopy and light curve shape as well as formation process. From Vink (2012).

thermonuclear explosion can be divided into three classes: (1) detonation models, where explosive nucleosynthesis occurs due to the compression and heating of the plasma by a shock wave moving through a star; (2) deflagration models, where the burning front proceeds slower than the local sound speed and the nuclear fusion in the burning front is sustained by convective motions that mix unburnt material into the hot burning zone; and (3) delayed detonation models, where the explosion starts as a deflagration and changes to a detonation wave, burning the remainder of the white dwarf into an intermediate mass element such as silicon (Vink, 2012).

1.2.2 Classification of SNe

There are several types of SNe. The old classification scheme of SNe into Type I and Type II was first introduced by Minkowski (1941) on the grounds of their optical spectra. Type I SNe show no hydrogen lines in their spectra, whereas these lines are present in Type II SNe spectra. Later, these types were subdivided based on their spectral characteristics (Turatto, 2003). For Type I, subtype Ia shows no helium in its spectrum, but exhibits characteristic absorption features, and in its later phase, emission lines from elements in the iron group. Type Ib SNe do not have obvious hydrogen lines, but they develop conspicuous He I lines after maximum light (Branch et al., 1982), while in Type Ic there are no hydrogen nor helium lines visible, but in their later phase, oxygen and calcium lines become visible. SNe of Types Ib and Ic are thought to originate from massive progenitor stars which have been stripped of their outer layers by companion stars.

SNe of Type II may be further distinguished both on account of their light curves and their spectra. Members of subtype IIP ("Plateau"), sometimes referred to as "normal" SN II, show a plateau in their light curves when the luminosity declines after maximum for about $2-3$ months. Subtype IIL ("linear") members, on the other hand, exhibit a linear decline of brightness after maximum. Type IIn SNe eventually show narrow emission lines in their spectra. Type IIb members are intermediate between Type Ib and Type II (Vink, 2012).

A new classification of SNe has been developed based on the fact that SNe are triggered in two ways: either by turning off or suddenly turning on the production of energy through nuclear

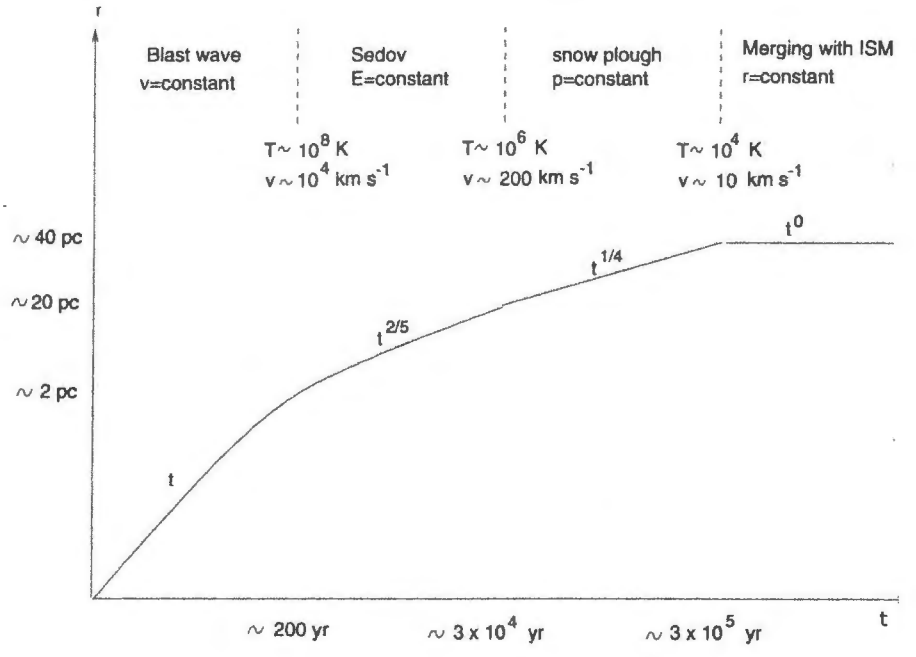

Figure 1.2: The radius of the SN shell as a function of time during different evolutionary phases. From Padmanabhan (2001).

fusion. Stellar cores which have exhausted their nuclear fuel collapse when their masses exceed the Chandrasekhar limit, while accreting white dwarfs ignite as they approach this limit. All the SNe events of Type IIb, IIP, IIL, Type Ib, Ic are the result of the core collapse of massive stars while events of Type Ia result from a thermonuclear SN (see Figure 1.1).

1.2.3 Evolutionary Stages of an SNR

An SNR passes through the following stages as it expands (Padmanabhan, 2001):

1. *Free expansion* of the ejecta, until they sweep up their own mass in circumstellar or ISM material. This stage can last tens of years to a few hundred years depending on the density of the surrounding gas.

2. *Sedov-Taylor phase*: Sweeping up of a shell of shocked circumstellar and interstellar gas, which is well modelled by a self-similar analytic solution. Strong X-ray emission traces the strong shock waves and hot shocked gas.

3. *Pressure-driven snowplow phase*: Cooling of the shell to form a thin (< 1 pc), dense ($1 - 100$ atoms cm^{-3}) shell surrounding the hot (few million kelvin) interior. The shell can be clearly seen in optical emission from recombined ionized hydrogen and ionized oxygen atoms.

4. *Momentum-driven snowplow phase*: The dense shell continues to expand because of its own momentum, while the interior cools down. This phase is best observed in the radio emission from neutral hydrogen atoms.

5. *Merging with the surrounding ISM.* When the SNR slows to the speed of the random velocities in the surrounding medium, after roughly a million years, it will merge into the general turbulent flow, contributing its remaining kinetic energy to the turbulence (see Figure 1.2).

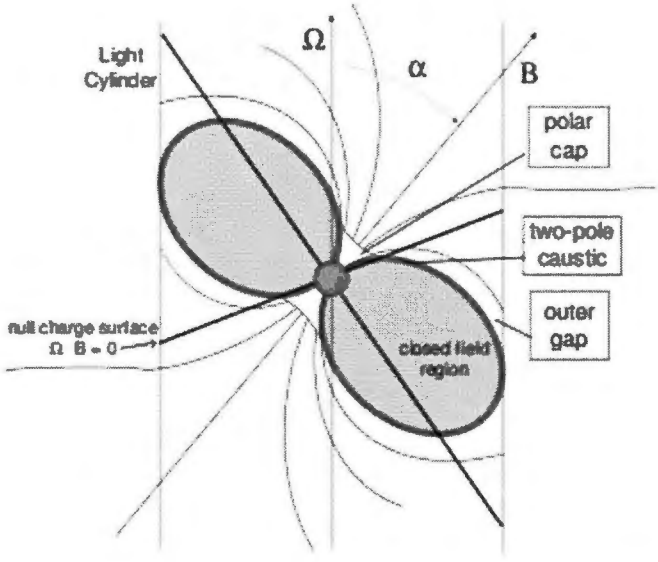

Figure 1.3: Schematic 2D view of the HE emission geometry of several proposed pulsar models. The closed field region is indicated by a grey fill. From Kaspi et al. (2006).

1.3 Pulsars

Baade & Zwicky (1934) proposed that an SN represents the transition of an ordinary star to an NS, which consists mainly of neutrons, having a very small radius and an extremely high density. Pulsars with characteristic ages of $< 10^5$ years are mostly found near SNRs, whereas older pulsars are not near these, because their SNRs have become invisible or the SN explosions expelled the pulsars with enough speed that they have escaped from their parent SNRs (Condon & Ransom, 2010). The outburst of a core-collapse SN (following the exhaustion of the star's nulcear fuel) blows away the entire outer envelope of the star, and leaves an ultracompact core. The collapse to an NS is possible for stars whose original mass is greater than about $8 - 10$ solar masses, while for progenitor masses below $6 - 8$ solar masses, the result will be a white dwarf (Mészáros, 1992) (see Section 1.1).

The first radio pulsar was discovered by Jocelyn Bell and Antony Hewish at Cambridge in 1967 (Hewish et al., 1968). The radio pulsar population presently comprises $\sim$ 2 000 objects with spin periods of 1.4 ms to 11.85 s (Manchester et al., 2005).

Pulsars are rapidly rotating NSs with strong magnetic fields and are born inside SNRs. They are sources of EM emission and relativistic particles. The structure of their magnetic field is such that it contains open and closed field lines, with the outermost closed field lines defining the light cylinder (where the corotation speed equals the speed of light), while the open field lines define the polar cap region of the pulsar (see Figure 1.3). The pulsar period P, together with the energy loss rate, gives some information about the pulsar's age. Most of the pulsars are found to be older than 10^5 years but still much younger than our galaxy ($\sim 10^{10}$ yr).

Pulsars emit radiation with a well-defined periodicity, and constantly lose energy because of a variety of radiation mechanisms (e.g., SR and curvature radiation) as well as particle acceleration.

The energy is supplied from the rotational kinetic energy of the pulsar and is given by

$$\dot{E} = -4\pi^2 I \frac{\dot{P}}{P^3}, \tag{1.5}$$

where I is the NS's moment of inertia. As a result, the angular velocity of the pulsar will be decreasing (and P increasing) over time. The age of the NS is inferred from P and $\dot{P}$ ($\dot{P} \equiv dP/dt$), following some assumptions. Suppose a pulsar spins down from an initial spin period P_0 such that

$$\dot{\Omega} = -k\Omega^n, \tag{1.6}$$

where $\Omega = 2\pi/P$, and n is the braking index, then for $n = 3$ the characteristic age of a pulsar is

$$\tau_c = \frac{P}{2\dot{P}}, \tag{1.7}$$

with P_0 being much smaller than P. The surface magnetic field strength of an NS can be inferred in the case of a dipole magnetic field, by setting equation (1.5) equal to the magnetic dipole radiation loss rate. The surface magnetic field strength is then given by

$$B_p \sim 3.2 \times 10^{19} (P\dot{P})^{1/2}\ G, \tag{1.8}$$

where P is in seconds. The magnetic field ranges from 10^8 G for recycled or millisecond pulsars to $> 10^{15}$ G for magnetars (Gaensler & Slane, 2006).

Given their rotational energy as well the outflow of a wind of relativistic particles from their magnetospheres, pulsars are thought to be the energy sources responsible for powering PWNe.

1.4 PWNe

PWNe are fascinating astrophysical sources visible across the EM spectrum. Observations of these sources aid our understanding regarding acceleration mechanisms and radiation processes inside these nebulae (Qiao et al., 2009a).

1.4.1 Formation of PWNe

The structure and evolution of filled-centre SNRs, also known as plerions, is a rich subject that involves many physical processes from hydrodynamics to HE particle acceleration and radiation (Weiler & Panagia, 1978). The term 'plerion', meaning 'filled centre', was coined by Weiler & Panagia (1978). Plerions are powered by the rotational energy of young pulsars which inject a relativistic wind containing HE particles and a magnetic field into the surrounding medium, blowing a 'bubble' which one observes as nebulous glowing objects. There are some factors that contribute to the shape and the spectrum of a PWN, including the angular distribution, magnetization, and energy spectrum of the wind streaming from the pulsar magnetosphere, as well as the pulsar velocity and the properties of the ambient medium (Kargaltsev, 2004).

In plerions, the PWN is inside an expanding SNR. The pulsar wind is highly over-pressured compared to its environment, and the PWN expands rapidly, moving supersonically and driving a shock into the stellar ejecta. Plerions thus form when the relativistic wind from a pulsar is

confined by a more slowly expanding ($V_{\rm exp}$ <<c) SNR surrounding the nebula. The spin-down energy of the pulsar may then be dissipated in a termination shock which accelerates the particles and randomizes their pitch angles. The PWN initially remains centred on the pulsar (Gaensler & Slane, 2006). However, if the expanding PWN at later times interact with a medium having a non-homogeneous density profile, the PWN may acquire an asymmetric shape and become removed from the SNR centre (see Section 1.4.4).

Plerions typically emit a broad-band spectrum of synchrotron emission from radio to X-ray wavelengths which is due to relativistic electrons and positrons supplied by the central pulsar, as well as an inverse Compton (IC) component in the γ-ray band (see Section 1.5). In the case of the Crab nebula, the emission at TeV energies can be explained as ICS of the SR and background photon fields by the relativistic particles in the plerion. Calculations of such synchrotron-self-Compton spectra provide a very good fit to the observed γ-ray spectrum of the Crab (De Jager & Harding, 1992).

1.4.2 Defining Characteristics of Plerions

The following are the defining characteristics of plerions (Weiler & Panagia, 1978):
(1) Filled-centre or blob-like form.
(2) A flat radio spectral index between 0 and -0.3.
(3) A well-organized magnetic field.
(4) High integrated linear polarization at high radio frequencies.
Weiler & Panagia (1980) added Vela X, part of the Vela SNR, as a member of this of source class. Three more properties have been added by De Jager & Djannati-Ataï (2008):
(5) Formation of a torus and jet near the pulsar, the direction of the jet being aligned with the direction of the pulsar spin axis, while the torus shows an underluminous region inside a characteristic scale radius $r_s \approx 10^{17}\mathrm{cm} - 10^{18}\mathrm{cm}$, where r_s is the pulsar wind (termination) shock radius (see Section 1.4.5).
(6) Evidence for reacceleration of particles from the region between the pulsar light cylinder and r_s, leading to a hard X-ray spectrum with a photon index of 1.5 to 2.0 near r_s.
(7) Evidence for synchrotron cooling (spectral steepening) at $r > r_s$, with the size of the PWN decreasing with increasing photon energies, as observed in the Crab and several other PWNe. The photon indices of the cooled spectra range between 2.0 and 2.5.

It is difficult to detect most of these diffuse sources in the optical due to interstellar absorption.

1.4.3 Evolution of PWNe

The evolution of PWNe depends on the following factors: (1) the structure of the SN; (2) the nature of the surrounding medium; (3) the evolution of the pulsar spin-down power; and (4) the space velocity of the pulsar. The evolution of the PWN can also be divided into two phases, important for observational appearance, as follows: initially, the PWN expands into the freely expanding SN ejecta. Later, the SNR interacts with the surrounding medium, and the inward motion of the reverse shock front is driven by this interaction, which may impact the PWN's evolution.

1.4.4 Interaction of PWN with the SNR Reverse Shock

When the SNR sweeps up mass from the ISM or circumstellar medium, it evolves into the Sedov-Taylor phase in which energy is conserved and is distributed between kinetic and thermal energy. The region of interaction between the SNR and its environment becomes a complex structure which consists of a forward shock where surrounding gas is compressed and heated, as well as a reverse shock where ejecta are decelerated. The reverse shock results from the low pressure inside the SN shell which implies the propagation of a strong inward shock wave, while the blast wave moves into the circumstellar medium (McKee, 1974). At first the reverse shock expands outward behind the forward shock, but after some time moves inward. The two shocks are separated by a contact discontinuity at which an instability can form. If in the absence of a pulsar or PWN, the SNR is expanding into a constant-density medium, the reverse shock reaches the centre of the SNR in a time

$$t_{\rm sedov} \approx 7 \left(\frac{M_{\rm ej}}{10 M_{\odot}}\right)^{5/6} \left(\frac{E_{\rm SN}}{10^{51}{\rm ergs}}\right)^{-1/2} \left(\frac{n_0}{1\ {\rm cm}^{-3}}\right)^{-1/3}, \tag{1.9}$$

where n_0 is the number density of the ambient gas. The SNR interior is entirely filled with shock-heated ejecta, and the SNR is in a fully self-similar state. The reverse shock compresses the PWN by a large factor, which responds with an increase in pressure and expansion. The crushing of the PWN produces Rayleigh-Taylor instabilities, which can produce a chaotic, filamentary structure and blending of thermal and nonthermal material within the PWN (see Gaensler & Slane, 2006, and references therein).

The effect of the reverse shock for SNRs propagating into an inhomogeneous ISM becomes important for evolved PWNe. Following the passage of the reverse shock into the PWN, the latter will expand subsonically, settling to a radius which is 25% of the SNR forward shock radius (Van der Swaluw et al., 2001). Van der Swaluw et al. (2001) showed that an inhomogeneous ISM pressure will result in the reverse shock returning to the PWN at different times of its evolution history, which can shift the position of the PWN, as observed for Vela X and G18.0-0.7 (the latter is associated with PSR B1823-13; Blondin et al., 2001). If SNRs generally occur inside an inhomogenous ambient medium (e.g., molecular clouds), we can expect to see several offset PWNe.

1.4.5 Tori and Jets

The well-known optical wisps in the Crab nebula are believed to mark the pulsar wind shock radius, where the pressure from the unshocked (upstream) pulsar wind balances the (downstream) nebula pressure (Kennel & Coroniti, 1984b). The high-resolution X-ray images of *Chandra* contributed significantly to the study of PWNe by showing that the presence of a torus and a perpendicular jet is common to PWNe (Ng & Romani, 2004), with an underluminous region in the inner part of these tori marking the PWN shock radius. Ng & Romani (2004) inferred the geometry of several of these structures, which established the orientation of the pulsar spin axis (aligned with the X-ray jet) on the sky.

1.5 Radiation Mechanisms

PWNe are thought to radiate via the mechanisms of SR and ICS of soft photons. The synchrotron brightness is a result of a convolution of the electron injection spectrum (relativistic wind from the

pulsar) and the nebular magnetic field strength, whereas the same electrons also scatter ambient photons into the HE to ultra-high-energy γ-ray range via ICS. Both components should be observed to understand the dynamics of the pulsar wind. Below we discuss SR and ICS.

1.5.1 SR: Particles Spiralling Magnetic Field Lines

The spectral energy distribution (SED) of a PWN typically consists of two components. The lower-energy component, spanning the radio to X-ray wavelengths is due to SR, while the HE one is due to ICS (see Section 1.5.2). During SR, charged particles (e.g., electrons) spiral around magnetic lines of force. Energetic electrons spiral very rapidly at speeds nearly equal to the speed of light.

Consider an energetic electron spiralling around a magnetic field line with a pitch angle α. The total SR energy loss rate is given by:

$$\dot{E}_{\rm SR} = \frac{2(r_0 \gamma B \nu_\perp)^2}{3c}, \tag{1.10}$$

where $\nu_\perp$ is the electron speed perpendicular to the B-field, and γ is the electron's Lorentz factor (Blumenthal & Gould, 1970). The electron speed may be written as $\beta_\perp c$. When averaging over α for an isotropic distribution of velocities, we obtain $\langle \beta_\perp^2 \rangle = \frac{2}{3}\beta^2$, so that the total radiated power is

$$P_{\rm tot} = \frac{4}{3}\sigma_{\rm T} c \beta^2 \gamma^2 U_{\rm B}, \tag{1.11}$$

where $\sigma_{\rm T} = 8\pi r_0^2/3$ is the Thomson cross section, $r_0 = e^2/m_e c^2$, $U_{\rm B} = B^2/8\pi$ is the magnetic energy density, and e is the electron charge. The SR single-particle spectrum is characterised by a critical frequency near which the spectrum reaches a maximum (Rybicki & Lightman, 1979):

$$w_{\rm c} = \frac{3}{2}\gamma^3 w_{\rm B} \sin\alpha = \frac{3}{2} e \frac{B \sin\alpha}{m_e c} \gamma^2, \tag{1.12}$$

with ω_B the gyration frequency of rotation

$$w_{\rm B} = \frac{eB}{\gamma m_e c}. \tag{1.13}$$

The power emitted per frequency by a single electron is given by (Rybicki & Lightman, 1979)

$$P(w) = \frac{\sqrt{3}}{2\pi} \frac{e^3 B \sin\alpha}{m_e c^2} F(x), \tag{1.14}$$

with

$$F(x) = x \int_x^\infty K_{\frac{5}{3}}(\xi) d\xi, \tag{1.15}$$

where $x \equiv w/w_{\rm c}$, $K_{5/3}$ is the modified Bessel function of order 5/3, and the function $F(x)$ has the

following approximate forms for small and large values of x (e.g., Erber, 1966):

$$F(x) \sim \frac{4\pi}{\sqrt{3}\Gamma\left(\frac{1}{3}\right)}\left(\frac{x}{2}\right)^{1/3}, \quad x \ll 1, \tag{1.16}$$

$$F(x) \sim \left(\frac{\pi}{2}\right)^{1/2} e^{-x} x^{1/2}, \quad x \gg 1. \tag{1.17}$$

The spectral maximum occurs at $0.29\omega_c$ (Longair, 1994).

If the number density $N(E)$ of electrons with energies in the range $(E, E+dE)$ can be expressed as a power law

$$N(E)dE = CE^{-p}dE, \quad E_1 < E < E_2, \tag{1.18}$$

the total SR power radiated by these particles is given by

$$P_{\rm tot}(\omega) \propto \omega^{-(p-1)/2} \propto \omega^s, \tag{1.19}$$

with $s = (p-1)/2$ the index of the energy spectrum. This means that

$$\frac{dN_\gamma}{dE} \propto \omega^{-(p+1)/2}, \tag{1.20}$$

similar to equation (1.32).

1.5.2 ICS: Upscattering of Soft Photons by Relativistic Electrons

Another important mechanism of radiation in HE astrophysics is known as ICS, i.e. the scattering process where a low-energy photon is scattered by an electron, and as a result the scattered photon will have a larger frequency (Cutnell & Johnson, 1995).

Consider the case of the Thomson limit, where

$$\gamma\varepsilon \ll m_e c^2, \tag{1.21}$$

where γ is the electron Lorentz factor, and ε is the soft photon energy. The mean energy of the Compton-scattered photon ϵ_1 for an isotropic photon gas is given by (Blumenthal & Gould, 1970)

$$\langle\epsilon_1\rangle = \frac{4}{3}\gamma^2\langle\epsilon\rangle, \tag{1.22}$$

where $\langle\epsilon\rangle$ is the mean energy of the soft photons. The resulting total energy loss rate of a single electron is given by the expression (Rybicki & Lightman, 1979)

$$-\frac{dE_e}{dt} = \frac{4}{3}\sigma_T c\gamma^2 U_{\rm iso}, \tag{1.23}$$

where $U_{\rm iso}$ is the energy density of the photon field, and σ_T is the Thompson interaction cross section equal to $6.65 \times 10^{-25}{\rm cm}^2$, similar to the expression for SR (see equation [1.11]). The interaction

cross section changes for the Klein-Nishina (K-N) regime to be discussed below (see Figure 1.4). The general IC spectrum in the Thompson limit is given by

$$\frac{dN_{\gamma,\epsilon}}{dtd\epsilon_1} = \frac{\pi r_0^2\, c\, n(\epsilon)d\epsilon}{2\gamma^4\epsilon^2}\left(2\epsilon_1 \ln\frac{\epsilon_1}{4\gamma^2\epsilon} + \epsilon_1 + 4\gamma^2\epsilon - \frac{\epsilon_1^2}{2\gamma^2\epsilon}\right). \tag{1.24}$$

This expression can be useful for the case where the electron energy distribution is a power law, and $n(\epsilon)$ is the photon number density associated with a blackbody distribution.

In the K-N limit, we have

$$\gamma\varepsilon \gg m_e c^2, \tag{1.25}$$

and the scattered photon energy is

$$\epsilon_1 \sim \gamma m_e c^2. \tag{1.26}$$

In the extreme K-N limit, the loss rate of the electron is (Blumenthal & Gould, 1970)

$$\frac{dE_e}{dt} \rightarrow \frac{1}{6}\pi r_e^2 \frac{(m_e ckT)^2}{\hbar^3}\left[\ln\left(\frac{4\gamma kT}{m_e c^2}\right) - 1.98\right], \tag{1.27}$$

where k is the Boltzmann constant. The general equation for the scattered photon spectrum per electron is given by (Jones, 1968; Blumenthal & Gould, 1970)

$$\frac{dN_{\gamma,\epsilon}}{dtdE_1} = \frac{2\pi r_0^2 m_e c^3 n(\epsilon)d\epsilon}{\gamma\epsilon}\left[2q\ln q + (1+2q)(1-q) + \frac{1}{2}\frac{(\Gamma_e q)^2}{1+\Gamma_e q}(1-q)\right], \tag{1.28}$$

where $E_1 = \epsilon_1/\gamma m_e c^2$ and Γ_e is the dimensionless parameter

$$\Gamma_e = \frac{4\gamma}{m_e c^2}, \tag{1.29}$$

and

$$q = \frac{E_1}{\Gamma_e(1-E_1)}. \tag{1.30}$$

The Thompson limit corresponds to $\Gamma_e \ll 1$ and $E_1 \ll 1$, when the energy of the photon is much smaller than the energy of the incoming electron.

If the electron spectrum is given by a power law

$$N_e(\gamma) = K_e\gamma^{-p}, \quad \gamma_0 < \gamma < \gamma_m, \tag{1.31}$$

where γ_0 and γ_m are the cutoffs of the distribution, the first order of correction to the spectrum in the Thompson limit shows that

$$\frac{dN_{\rm tot}}{dtd\epsilon_1} \propto \epsilon_1^{-(p+1)/2}, \tag{1.32}$$

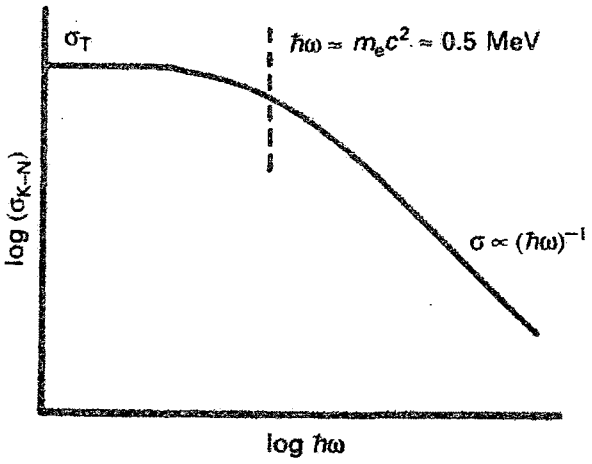

Figure 1.4: A schematic diagram showing the dependence of the ICS interaction cross section on soft photon energy. From Longair (1994).

while the total Compton spectrum in the extreme K-N limit is given by

$$\frac{dN_{\rm tot}}{dtd\epsilon_1} \propto \epsilon_1^{-(p+1)}. \tag{1.33}$$

In the extreme K-N limit, dE_e/dt increases only logarithmically with E_e (or γ) and is proportional to T_{BB}^2, where T_{BB} is the blackbody temperature, while in the Thomson limit $dE_e/dt \propto E_e^2 T_{BB}^2$. It should, however, be noted that the extreme K-N and Thomson energy loss rates have different meanings. In the case of the Thomson limit, the electron loses a small fraction of its energy in each Compton collision. In the extreme K-N limit, at very high energies, the electron loses its energy in discrete amounts which are a sizable fraction of its initial energy (Blumenthal & Gould, 1970).

1.6 Problem Statement

The PWN associated with the Vela pulsar is a bright source in the radio, X-ray and γ-ray bands, but not in the optical waveband. In the past, Ögelman et al. (1989) claimed detection of an optical counterpart to the compact X-ray nebula. However, Mignani et al. (2003) obtained much deeper upper limits using the *Hubble Space Telescope (HST)*. In this study, we want to attempt to resolve Vela X using a new analysis technique. If we find the optical counterpart, we will be able to investigate possible morphological changes between the radio and optical lobes. This investigation should contribute to our understanding of the dynamic Vela X compact nebula. In addition, we also want to ascertain whether the lepton spectrum responsible for producing the radio synchrotron lobe also extends into the optical domain. Knowledge of the brightness and structure of the Vela PWN is important in order to constrain the underlying particle spectrum associated with this extended source. The results should help to test whether the electron particle population consists of a single or multiple components. In particular, we want to investigate how the lepton ($e^{\pm}$) spectra responsible for the radio and optical SR emission connect.

1.7 Aims and Objectives

The optical Vela X nebula is still elusive. There are no wide field of view (FoV) observations of the synchrotron emission between radio and the X-ray energy available. Therefore, we do not know how the morphology changes with energy, or how the lepton spectra responsible for radio and optical SR components connect. We will search the extant data from the Digital Sloan Survey (DSS) to try and extract the optical morphology. We will compare the optical images with those obtained with *Chandra ACIS* to search for an extended emission pattern that could be identified as counterparts of the radio nebula elements. In addition, we will perform observations using 1.0 m South African Astronomical Observatory (SAAO) telescope. We will consider a large FoV so that the entire Vela X nebula will have been covered. To cover such a view we will construct a mosaic consisting of $3 \times 3 = 9$ images around the pulsar, each consisting of $70 \times 72 = 5\ 040$ pixels. The image will be constructed by removing stars with high intensity compared to the background level of the optical image. We will compare the smoothed optical image with the radio, X-ray, and γ-ray images, to study the multiwavelength properties of the Vela PWN and the SNR, using a different technique from the ones performed previously by Ögelman et al. (1989) and Mignani et al. (2003). If our observations indicate a smooth transition between radio and X-rays component, it would mean that we are dealing with a single particle population, whereas a spectral depression between radio and X-rays may be a hint for a two particle population scenario.

1.8 Outline of Dissertation

In Chapter 1 we gave a background on the stellar evolution, the creation, classification and evolution of SNRs, followed by a brief overview of pulsars. We also discussed the formation of PWNe, characteristics of plerions, evolution of PWNe and their interaction with the SNR reverse shock, and the occurence of tori and jets in PWNe. We next discussed radiation mechanisms, including SR and ICS. Lastly, we summarised our problem statement, aims and objectives and the outline of the thesis. Chapter 2 deals with the Vela X plerion, including its discovery and the identification controversy surrounding Vela X, multiwavelength observations of the Vela PWN, and modelling of the Vela plerion. In Chapter 3, we study the multiwavelength properties of the Vela system, including discussion of the Vela SNR as well as the Vela pulsar. In Chapter 4, we present our optical observations and data analysis. Our results are discussed in Chapter 5, and Chapter 6 deals with the discussion and conclusion.

Chapter 2

The Vela X Plerion

The Vela PWN is a nearby astronomical system which can be studied over a wide range of wavelengths, since it is a bright source in the radio, X-ray, and γ-ray bands. In this chapter, we will give an overview of the discovery of, and identification controversy surrounding, Vela X: whether it is a plerion or part of the Vela SNR shell. We will also collect various multiwavelength observations of this PWN, including measurements in the radio, infrared (IR), optical, ultraviolet (UV), X-ray, and γ-ray wavebands. Lastly, we will discuss the broadband modelling of the plerion, involving either a leptonic or hadronic scenario, after which will follow the conclusions.

2.1 Discovery and Identification Controversy of Vela X

The Vela Constellation is visible from the Southern Hemisphere. The name derives from the Latin word meaning "sail". The Vela stellar group used to form part of a larger constellation, Argo Navis. This constellation was named after the mythological ship on which Argonauts, led by the Greek hero Jason, sailed home after their journey in search of the golden fleece protected by a sleepless dragon. Later the Constellation Argo Navis was divided into four parts by the French astronomer Nicolas Louis de Lacaille: Carina (the keel), Vela (the sail), Puppis (the stern), and Pyxis (the compass) (Allen, 1963).

Using a pencil-beam aerial, McGee et al. (1955) surveyed the sky between a declination of $-17°$ and $-49°$ at 400 MHz. They observed an extended source in the direction of the Vela Puppis region. The two Mills Cross telescopes at the Fleurs Field Station near Sydney were used to observe the Vela Puppis region at 3.5 m (Rishbeth, 1958). Strong nonthermal sources near the Galactic Equator were detected. The brightest of these were designated Vela X, Vela Y, and Vela Z. Vela X was the brightest object and was tentatively associated with Stromlo 16, an Hα filamentary nebulosity. At a wavelength of 15 m, Vela X, Vela Y, and Vela Z were unresolved (Rishbeth, 1958). Using the Rishbeth (1958) results as well as observations at 960 MHz (Wilson & Bolton, 1960), Harris (1962) adopted a flat spectral index of $\alpha = 0.00 \pm 0.15$ for the Vela X radio spectrum, $S \propto \nu^{\alpha}$, where S is the flux density, ν is the frequency, and α is spectral index.

Milne (1968a) believed the Vela X, Vela Y, and Vela Z sources to be the Vela SNR associated with the optical filamentary nebula Stromlo 16 near the centre of the large Gum Nebula (Milne & Manchester, 1986) and adopted a source distance of 0.5 kpc (the modern distance for the Vela pulsar is assumed to be $\sim$ 290 pc; see Section 3.2.2). These sources span an area of about eight square degrees. He inferred an integrated spectrum with a spectral index of $\alpha = -0.3 \pm 0.1$ for a power-law fit to the whole region, including Vela X, Vela Y, and Vela Z, but $\alpha = -0.3 \pm 0.2$ for

the differential spectrum of Vela X only. Using polarization measurements, Milne (1968a) noted that a circumferential B-field configuration may be a possible interpretation. However, Davies & Gardner (1970) commented that the derived B-field is rather uncertain because of rapid changes in polarization angle.

Milne (1968b) performed an optical observation of two filaments in Stromlo 16 (Vela X). He suggested that Vela X be identified with the Vela SNR on the basis of three arguments: (1) the existence of electron temperature stratification, also seen in other SNRs; (2) the upper limit for the filaments' mass approaching the mass that is expected to have been swept up by the expansion of the SNR to its present size; (3) the spectra exhibiting a collisionally excited nature.

As part of a Galactic Plane survey at 2.7 GHz using the 64 m Parkes Radio Telescope, Day et al. (1972) reobserved the Vela complex, including Vela X, Vela Y, and Vela Z. His map showed more details, but was in good general agreement with the results of Milne (1968a). There was no contribution from unrelated extragalactic background sources to the flux of the Vela source. Milne (1980) found that the total intensity and polarization at 2.7 GHz and 5 GHz were fairly uniformly distributed. There were some regions which showed a uniformly directed polarization, indicating an ordered magnetic field. At 2.7 GHz, the map by the Parkes 64 m Radio Telescope was consistent with the map obtained by Day et al. (1972). Milne (1980) suggested a power-law spectrum with $\alpha = -0.4$ for frequencies above 400 MHz. The average spectral index obtained over these two frequencies was found to be $\alpha_{\rm av} = -0.33$ (Milne, 1980).

Weiler & Panagia (1980) argued that because the remnant is large and near the Galactic Plane, it had not been easy to obtain accurate integrated flux density measurements at many frequencies, and for that reason the spectral index was uncertain, with estimates ranging from $\alpha = -0.3$ to -0.5 for Vela XYZ (Green, 1974; Milne, 1980; Clark & Caswell, 1976). However, a different spectral index was obtained for different parts of the SNR, e.g., Poveda & Woltjer (1968) found a spectral index of $\alpha = 0.0 \pm 0.2$ for Vela X and $\alpha = -0.4 \pm 0.2$ for Vela Y. Milne (1968a) found $\alpha = -0.3 \pm 0.1$ for Vela X, $\alpha = -0.6 \pm 0.4$ for Vela Y and Vela Z, and $\alpha = -0.3 \pm 0.2$ for the integrated emission from Vela XYZ. Weiler & Panagia (1980) considered Vela XYZ as composed of two parts, obtaining a flat spectrum ($\alpha = -0.08 \pm 0.10$) for Vela X, and a steeper spectrum ($\alpha = -0.65 \pm 0.22$) for Vela YZ. They also found that the spectral index $\alpha = -0.08$ does not vary much over Vela X. Such a flat spectrum is more reminiscent of the spectra found for filled-centre or plerionic SNRs such as the Crab Nebula ($\alpha = -0.26$) or 3C 58 ($\alpha = -0.1$) than for shell-type SNRs (which have an average index of $\alpha \sim -0.45$; Weiler & Panagia, 1980).

Radio observations of linear polarization revealed that all parts of the remnant are nonthermal sources of synchrotron emission (Milne, 1968a). Vela X is highly polarized with the polarization percentage exceeding 20% at 2 650 MHz, while the polarization of Vela YZ is weak. Vela X exhibits a blob-like morpholgy, being the brightest in the centre with a decreasing radio intensity in all directions towards the edges, with an overall size of 3.6 degrees in the right ascension direction, and 2 degrees in the declination direction (see Weiler & Panagia, 1980, and references therein).

In the optical, a large diffuse nebulosity which is brightest near Vela X and the Vela pulsar was found (Elliott et al., 1976). There is also a hard X-ray source which is concentrated near the pulsar (J0835−4510; Kellogg et al., 1973). Weiler & Panagia (1980) estimated that the total luminosity of the broadband electromagnetic spectrum is about 1% of the pulsar spin-down luminosity. This means that the pulsar has adequate rotational energy to power Vela X.

In view of the above, Weiler & Panagia (1980) proposed that Vela X should be considered

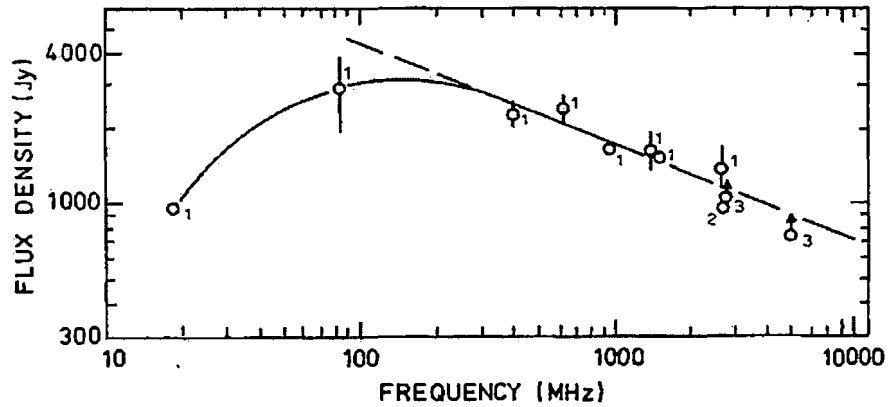

Figure 2.1: Radio spectrum of Vela. The straight line corresponds to a power-law fit with a spectral index of $\alpha = -0.4$. Absorption has been suggested to occur below 200 MHz. From Milne (1980).

a "plerion", a phrase coined by Weiler & Panagia (1978) which derives from the Greek word $\pi\lambda\eta\rho\eta s$ meaning 'filled' (refering to filled-centre SNRs). Vela X therefore exhibits the following characteristics of plerions summarized by Weiler & Panagia (1980): (1) a filled-centre or blob-like morphology; (2) a flat radio spectral index ($\alpha = 0$ to -0.3); (3) a well organized magnetic field; and (4) a high integrated linear polarization at high radio frequencies.

Milne (1980) fitted the measured radio flux density of the Vela region with a power-law spectrum with $\alpha = -0.4$ for frequencies above 400 MHz (Figure 2.1). This is quite steeper than the $\alpha \sim 0.0$ found by Weiler & Panagia (1980). Below this frequency there is a fall-off in the spectrum, which Milne (1980) pressumed to be due to free-free absorption. Milne (1980) also noted that the data points at 2.7 GHz and 5 GHz excluded Vela Y and Vela Z.

Milne & Manchester (1986) have doubted that Vela X is a pulsar-driven component of the SNR based on the variation of spectral index relative to the rest of the SNR, and argued that it was simply an enhanced portion of the shell emission. They presented three arguments, namely: (1) the pulsar is not located at the centre of the radio emission, but is offset from Vela X's peak by $\sim 40'$; (2) in comparison with the Crab Nebula, the X-ray emission of Vela X is very weak; rather, the nebula is comparable in luminosity to that of the X-ray nebula surrounding the radio pulsar PSR B1055−52, which has no radio remnant. The Vela X radio nebula might therefore be expected to be much weaker than observed; (3) Weiler & Panagia (1980) determined a spectral index for Vela X of $\alpha = -0.08 \pm 0.10$ also using observations at 85 MHz (Rishbeth, 1958), but these data were of relatively poor resolution and sensitivity compared with that of later data. Milne & Manchester (1986) suggested that the 85 MHz data were affected by free-free absorption occurring in the SNR, and that if these 85 MHz data were corrected for this effect, there would be no significant difference between the radio spectral index of Vela X and that of the rest of the shell. They also noted that Weiler & Panagia (1980) did not include the measurements at 408 MHz and 635 MHz by Milne (1968a), which showed that the spectral index of Vela X varies between $\alpha = -0.3$ and -0.4 (at least for frequencies above 635 MHz), which is not very different from the index of the shell.

Dwarakanath (1991) attempted to solve the identification problem by using data in the range 34.5 MHz to 5 GHz. These data have typical errors of 10%, and a flux density contamination by background sources of $\leq$ 2%. Figure 2.2 shows the Vela XYZ region in radio/X-rays. The harder X-ray emission (dashed contour), believed to be nonthermal, stretches from the pulsar

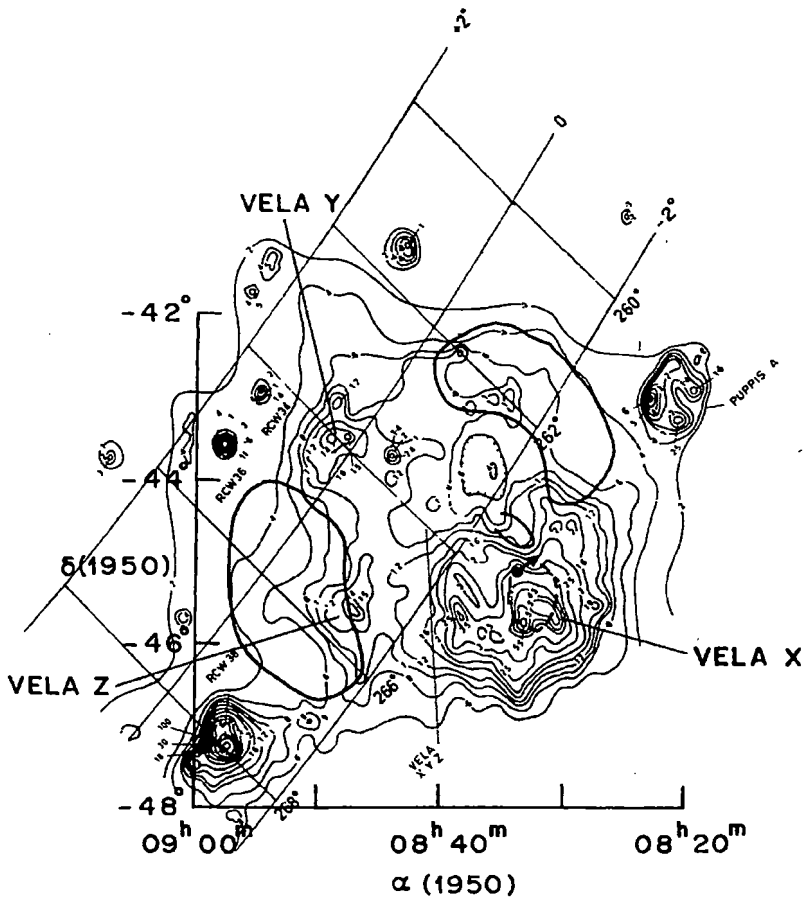

Figure 2.2: The 2.7 GHz map of Vela X, Vela Y, Vela Z, and Puppis A by Dwarakanath (1991). The thick solid lines indicate boundaries of significant thermal X-ray emission in the 0.2 keV−1.0 keV energy range (Kahn et al., 1985). The dashed line marks the boundary of the region from where non-thermal X-ray emission in the range of 1.4 keV−3.5 keV has been observed (Harnden et al., 1985). The filled circle indicates the position of the Vela pulsar PSR J0833−4510. The arrow indicates the pulsar's direction of proper motion observed by Bailes et al. (1989).

PSR J0833−4510 (shown by a filled circle) towards the peak of emission of Vela X. The extended X-ray emission (thick solid contour), believed to be thermal, roughly follows the boundary of the radio remnant, with no X-ray emission observed in the vicinity of Vela Y. According to Dwarakanath (1991), the controversy regarding Vela X's classification was based on the Vela SNR radio morphology, spectral index, polarization at high radio frequencies, the presence of nonthermal X-rays, and the apparent association of the pulsar PSR J0833−4510 with the remnant. Weiler & Sramek (1988) confirmed the radio flux density spectral index of $\alpha = -0.08$ for Vela X (Weiler & Panagia, 1980), which is flatter than that of Vela Y and Vela Z. Dwarakanath (1991) obtained a flat spectral index of $\alpha = -0.16 \pm 0.02$ for Vela X and $\alpha = -0.53 \pm 0.03$ for Vela Y and Vela Z. He also noted that there is negligible free-free absorption at 85 MHz. The pulsar is indeed 40′ away from Vela X, and this cannot be explained by proper motion measurements (see Section 3.2.2). However, this offset may be explained by asymmetrical expansion of the nebula due to inhomogeneities in the ambient medium. Dwarakanath (1991) concluded that the Vela SNR therefore has a hybrid morphology (an outer shell and a central plerion).

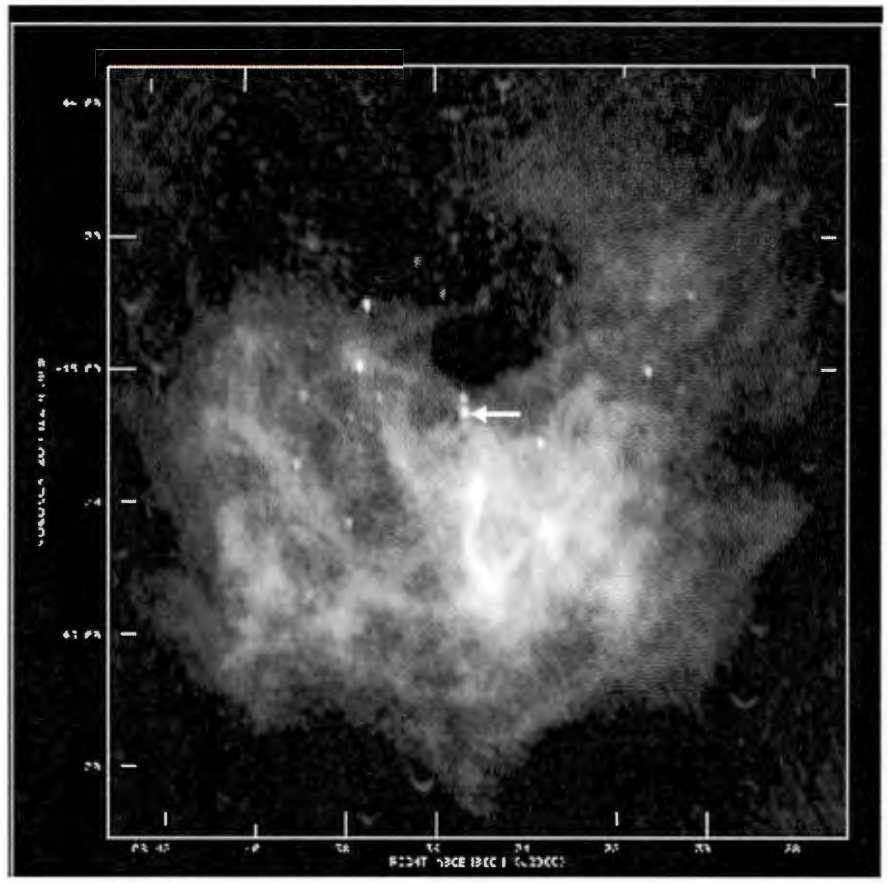

Figure 2.3: The radio continuum image of the Vela X remnant at 90 cm by Frail et al. (1997). The position of the Vela pulsar is indicated by a white arrow.

Milne (1995) observed the Vela X SNR at 8.4 GHz, and found prominent radio filaments with a width of $\sim 2'.5$ unrelated to the optical ones. These filaments were highly polarized, having magnetic fields pointing along them. He also maintained that the spectral index was very constant across the SNR, in the range of $\alpha = -0.4$ to $\alpha = -0.8$.

Using the VLA, Frail et al. (1997) found that the morphology of Vela X consists a of network of fine, overlapping, linear, synchrotron-emitting filaments throughout the nebula. These are ubiquitous in pulsar-powered nebulae such as the Crab and 3C 58. The brightest filament lies south of the pulsar, extending towards the centre of Vela X. The observed filament was thought to be the radio counterpart of an X-ray feature found by Markwardt & Ögelman (1995) (see Section 3.1.3). However, the radio feature (average width = $2.8'$) is systematically offset to the eastern direction relative to the X-ray jet-like feature (average width = $12'$). The magnetic field furthermore is oriented along this filament (Milne, 1995). Figure 2.3 shows the entire Vela X region as observed at 90 cm, exhibiting a network of fine, overlapping filaments. Frail et al. (1997) argued that the mesh of filamentary structures of Vela X suggested that the radio counterpart to the X-ray cocoon (see Section 3.1.3) was indeed pulsar-driven. They also noted that jet-like structures are commonly observed in PWNe, and suggested that the observed bright filament may represent the funneling of spin-down power from the Vela pulsar to Vela X. They argued that this may provide a solution to the question of how the offset pulsar may sustain the Vela X plerion.

Bock et al. (1998) performed a multiwavelength study of the Vela SNR including high-resolution

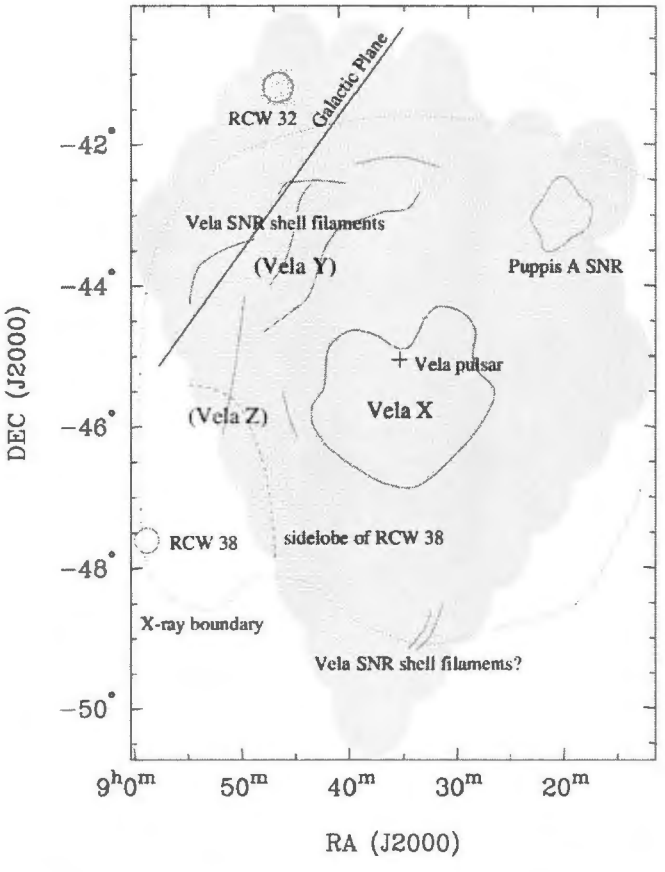

Figure 2.4: A cartoon showing key features in the Vela X region. The radio peaks of Vela X, Vela Y, and Vela Z are marked (Bock et al., 1998).

radio data at 843 MHz, and were able to show beyond question that Vela X is a pulsar-powered nebula, on the basis that there are significant morphological differences between the nebula and the SNR shell. They even argued that Vela X could be viewed as the Galactic archetype of plerions. Bock et al. (1998) found shell filaments oriented perpendicularly to the radial direction towards the SNR centre, also having Hα and X-ray counterparts. In contrast, they found a filamentary structure within the plerion which is more nebulous, generally having a north-south alignment. The shell and the nebula may therefore be conclusively identified. Figure 2.4 is a cartoon version of the Vela region, indicating several radio features, including the Vela X nebula and Vela SNR shell filaments, and the Puppis A SNR. Using their higher resolution image, Bock et al. (1998) argued that the identification of the bright radio filament with the X-ray jet by Frail et al. (1997) might be less firm, since it was indistinguishable from other nearby radio filaments, and its flux density may have been overestimated.

Alvarez et al. (2001) reanalysed published data in order to evaluate the distribution of the spectral index over the Vela SNR. They were able to obtain spectral indices for Vela X, Vela Y, and Vela Z individually for the first time, finding $\alpha_X = -0.39 \pm 0.03$ between frequencies ranging from 85.7 MHz to 8.4 GHz, and $\alpha_Y = -0.70 \pm 0.10$ and $\alpha_Z = -0.81 \pm 0.16$ between frequencies ranging from 85.7 MHz to 2.7 GHz. Table 2.1 compares the results of Alvarez et al. (2001) for α_X with those from other authors, and Table 2.2 does the same for Vela Y and Vela Z. Alvarez et al. (2001) deduced that the α_X given by Milne (1968a) is similar to their own, but the first value has

a large uncertainty. The values of Weiler & Panagia (1980) and Dwarakanath (1991) for α_X are significantly larger than these found by Alvarez et al. (2001) and Milne (1968a). However, Alvarez et al. (2001) caution the reader that these results were derived from peak flux densities, rather than from integrated flux densities. Alvarez et al. (2001) do agree with Weiler & Panagia (1980) and Dwarakanath (1991) that α_Y and α_Z are lower than α_X, finding comparable values for α_Y and α_Z. Alvarez et al. (2001) lastly constructed a map of the spatial distribution of the spectral index over the Vela SNR region. This map exhibits a circular symmetry, with α decreasing as one moves away from Vela X. This is consistent with the picture where the SNR has a spherical geometry and roughly constant spectral index, with the central Vela X source superposed, having a harder steep spectrum.

Dodson et al. (2003b) reported that they had observed (at GHz frequencies) the true extent of two radio lobes to the north and south of the pulsar (enveloping the X-ray nebula), as well as the morphology of the highly-polarized radio nebula which is associated with the Vela pulsar. The wound-up toroidal magnetic field structure revealed by the polarization data, together with the symmetric morphology around the projected spin axis of the pulsar, argues strongly for a pulsar-driven nature of this nebula. Hales et al. (2004) note that the spectral energy distribution (SED) and overall morphology observed at high radio frequencies resemble that of the other plerions, arguing for the case that the nebula derives its energy from the pulsar.

2.2 Multiwavelength Observations of the Vela PWN Region

2.2.1 Radio

The strong nonthermal radio sources Vela X, Vela Y, and Vela Z were detected near the Galactic Plane (Rishbeth, 1958). Milne (1968a, 1980); Milne & Manchester (1986); Milne (1995) found an average spectral index of ~ -0.3 to -0.6 for both Vela X and the full Vela region. By contrast, Weiler & Panagia (1980) found $\alpha_X = -0.08$ for Vela X, which does not vary much over the extent of this source, and which is much flatter than the indices of Vela Y and Vela Z. Dwarakanath (1991) confirmed these results and obtained a flat spectral index of $\alpha_X = -0.16 \pm 0.02$ for Vela X, and $\alpha = -0.53 \pm 0.03$ for Vela Y and Vela Z. Alvarez et al. (2001) obtained spectral indices for Vela X, Vela Y, and Vela Z individually for the first time, finding $\alpha_X = -0.39 \pm 0.03$ between frequencies ranging from 85.7 MHz to 8.4 GHz, and $\alpha_Y = -0.70 \pm 0.10$ and $\alpha_Z = -0.81 \pm 0.16$

Table 2.1: Summary of determinations of the spectral index of Vela X; see Alvarez et al. (2001).

α_X	β_X+2	ν (MHz)	Reference
+0.0		19.7, 85.7, 960	Wilson (1963)
	-0.3 ± 02	85 – 1440	Milne (1968a)
	−0.4	635, 1 410, 2 650	Milne (1968a)
	-0.08 ± 0.02	85.5 – 5 000	Weiler & Panagia (1980)
	-0.35 ± 0.05	408 – 2 650	Milne & Manchester (1986)
-0.16 ± 0.02		34.5 – 5 000	Dwarakanath (1991)
	−0.10	34.5 – 408	Dwarakanath (1991)
-0.6 ± 0.2		2 700, 5 000, 8 400	Milne (1995)
-0.39 ± 0.03		85.7 – 8 400	Alvarez et al. (2001)
+0.1		26 000 – 36 000	Hales et al. (2004)
-0.50 ± 0.05		23 000 – 94 000	Abdo et al. (2010)

Table 2.2: Summary of the determination of the spectral indices of Vela Y, Vela Z, and Vela YZ; from Alvarez et al. (2001).

α_Y	$\beta_Y + 2$	α_Z	$\beta_Y + 2$	α_{YZ}	ν (MHz)	Reference
				-0.5	19.7, 85.7, 960	Wilson (1963)
	-0.6 ± 0.4		-0.6 ± 0.4		85–1 440	Milne (1968a)
	-0.4		-0.4		635, 1 410, 2 650	Milne (1968a)
				-0.65 ± 0.22	408–2 650	Weiler & Panagia (1980)
	-0.35 ± 0.05		-0.35 ± 0.05		408–2 650	Milne & Manchester (1986)
	-0.45		-0.5		34.5–408	Dwarakanath (1991)
				0.53 ± 0.03	34.5–2 700	Dwarakanath (1991)
-0.70 ± 0.10		-0.81 ± 0.16			85.7–2 700	Alvarez et al. (2001)

between 85.7 MHz and 2.7 GHz. Although these indices are softer than those of Weiler & Panagia (1980) and Dwarakanath (1991), they do support the distinct nature of Vela X on the one hand, and Vela YZ on the other.

Bietenholz et al. (1991) reported the discovery of a localized elongated ridge of highly polarized (~70%) radio emission in a direction northeast of the Vela pulsar, subtending an angle of 50° at the pulsar position. The feature has a concave shape towards the pulsar, with a steep spectrum ($\alpha \sim -0.6$) between 1.5 GHz and 5 GHz. Based on the physical and geometric properties, Bietenholz et al. (1991) argued that this feature is associated with the Vela pulsar and is not part of the larger-scale radio emission of Vela X. It furthermore lies outside of the X-ray synchrotron nebula (see Section 2.2.3). This observed feature has the following attributes in common with those seen in the Crab: (1) similar morpholgy; (2) located at a similar distance to from the pulsar; and (3) high polarization. It is thus similar to the wisps observed in the Crab Nebula, probably associated with the outflow of particles from the pulsar. They also suggested that this feature is a part of the shock produced by the termination of the relativistic magnetohydrodynamic pulsar wind into the ambient medium.

Dubner et al. (1998) compared the HI radio emission to the Molongo Observatory Synthesis Telescope (MOST) radio continuum emission at 843 MHz. They found a good correlation between the main ridge of the HI shell and the outermost arched radio filaments. No evidence was found for strong inhomogeneities in HI near the Vela X position, arguing against the idea that interstellar medium (ISM) inhomogeneities influenced the nebula morphology.

Frail et al. (1997) found a bright radio filament in Vela X that lies due south of PSR J0833–4510, beginning about 13′ from the pulsar and terminating 35′ farther south at the continuum maximum of Vela X.

Bock et al. (2002) observed Vela X at high resolution and a frequency of 1.4 GHz using the Australia Telescope Compact Array (ATCA). They found that the linearly polarized emission was only partially correlated with total intensity. Several depolarization features have also been observed, some of which have been identified with foregound Hα filaments.

Lewis et al. (2002); Dodson et al. (2003b) used the ATCA and found two radio lobes (at 1.4 GHz – 8.5 GHz) oriented about the spin axis of the pulsar, starting at the edge of the X-ray emission (Helfand et al., 2001; Dodson et al., 2003b), and extending to three times its size. The northern lobe exhibits a bright edge, while the southern lobe is more diffuse. The emission from the two lobes is typically 70% linearly polarised and has a spectral index of $\alpha = -0.5$ between 2.4 GHz and 5 GHz, which implies that the emission is due to synchrotron radiation. (Dodson et al. (2003b) however find $\alpha = -0.3$ in the 1.4 GHz – 5 GHz range.) The morphology is inconsistent with either a bow-shock or a static-shock PWN. The radio lobes lie around the spin axis, in agreement with models where the emission is driven by particles from magnetic poles. The intensity, polarization,

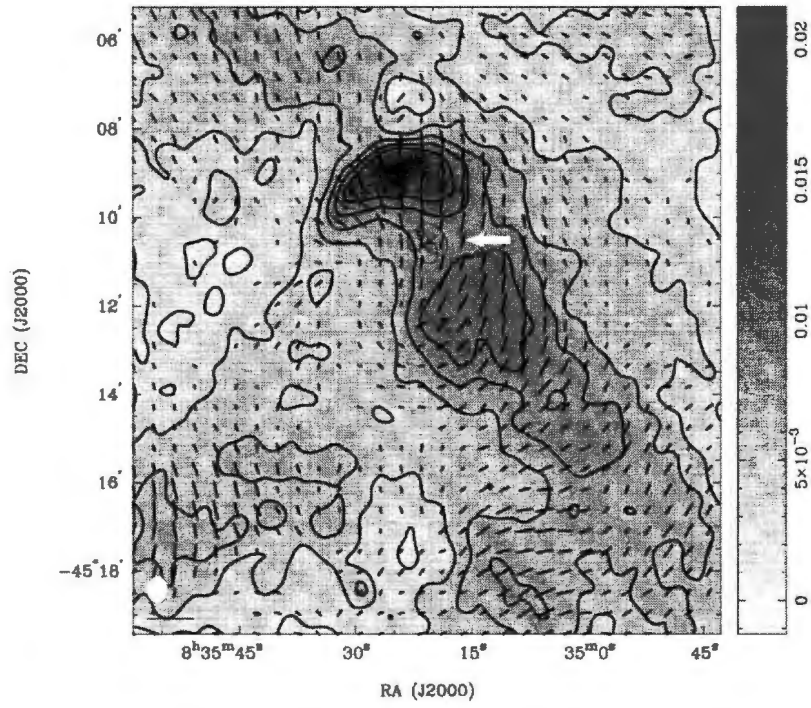

Figure 2.5: Total intensity map around Vela X at 2.4 GeV, with polarised **E**-vectors indicated. The length of the white bar at the bottom left represents 10 mJy. The image is corrected for primary beam response and the FR-II galaxy has been removed. A wireframe model of the X-ray emission is overlaid (indicated by a white arrow). Adapted from Dodson et al. (2003b).

and spectral index characteristics of the lobes are different from those of the Vela X region, leading Lewis et al. (2002) to propose that the compact nebula is directly driven by the pulsar, while Vela X has a longer formation history.

The radio emission of the Vela PWN is mostly from the two lobes around the pulsar which are different in size and brightness (Dodson et al., 2003b). Figure 2.5 shows the total intensity of the 2.4 GHz radio emission around the pulsar. The small wireframe model around the pulsar indicates the X-ray emission, while the lines indicate the polarisation **E**-vectors as observed by *Chandra*. The extension towards the south as seen in Figure 2.5 was found to be unpolarised, and confirms its different character when compared to that of the nebula. Dodson et al. (2003b) noted that the most striking feature when comparing the X-ray and radio emission is that the radio emission starts at a distance from the radio nebula centre where X-ray emission terminates.

Hales et al. (2004) studied the differences between the SED of the Vela PWN and the brightest filaments at 26 GHz – 36 GHz using the *Cosmic Background Imager (CBI)*. They found a strong compact source ($5'.9 \times 4'.1$) around the Vela pulsar associated with the radio PWN as described by Dodson et al. (2003a). Furthermore, the orientation of the 31 GHz PWN is in agreement with that of the radio lobes observed at higher resolution and at lower radio frequencies. The filaments are at a very low level at 31 GHz compared to lower frequencies. Hales et al. (2004) found that the spectral index of the radio PWN is flatter than the rest of Vela X (even marginally positive with a value $\alpha = 0.10 \pm 0.06$), while the filamentary structure has a negative spectral index of

$\alpha = -0.28 \pm 0.09$. Their spectral indices for the filamentary structure are in good agreement with that found by Alvarez et al. (2001) for the whole of Vela X. This implies distinct acceleration processes for particles in the PWN and the filaments. Hales et al. (2004) also noted that there was a filament seen southeast from the PWN, ending in an anchor-like feature, which was situated in the direction of the proper motion and spin axis of the pulsar. They found that the SED and morphology of Vela X are similar to those of plerions in general, and this led them to suggest that Vela X might be powered by the pulsar.

Abdo et al. (2010) examined archival *Wilkinson Microwave Anistropy Probe (WMAP)* sky maps, and found a prominent excess in the all-sky images at 23, 33, 41, 61, and 94 GHz for the Vela X region. This source separates into an eastern and western sub-region at higher frequencies and higher resolution. These sub-regions lie well south of the Vela pulsar. This concentrated area is furthermore consistent with the 0.4 GHz all-sky maps of Haslam et al. (1982). Abdo et al. (2010) estimated a flux density spectral index of $\alpha = -0.50 \pm 0.05$ for Vela X (see Figure 2.9), which is comparable to but steeper than $\alpha = -0.39 \pm 0.03$ measured for frequencies between 0.03 GHz to 8 GHz for a much larger region (Alvarez et al., 2001).

2.2.2 IR, Optical, and UV

Ögelman et al. (1989) claimed a marginal detection of an optical counterpart to the compact X-ray nebula using the ESO 2.2 m telescope. They noted that a diffuse nebula centred on the Vela pulsar was distinguishable in the V and B filters, and clearly saw several wisplike structures. Assuming that the compact nebula was not contained within the CCD boundaries at the northern side, and that it had a size of $3'.5$(N–S) by $2'$ (E–W), Ögelman et al. (1989) found upper limits of 15.8 ± 0.3 mag in V and 16.1 ± 0.3 in B. Alternatively, assuming that the nebula was the excess of size $1'.5$ located near the pulsar, upper limits of 17.3 ± 0.5 mag in V and 18.1 ± 0.5 mag in B were found. (However, Mignani et al. (2003) obtained much deeper upper limits using the *Hubble Space Telescope (HST)* – see below.)

Sefako (2002) used data from the South African Astronomical Observatory (SAAO) 1.0-m

Table 2.3: 3σ upper limits to the surface optical brightness of the X-ray PWN structures (Mignani et al., 2003).

			Observed		Extinction-corrected[a]	
Telescope	Instrument	Filter	mag arcsec^{-2}	Flux[b]	mag arcsec^{-2}	Flux[b]
HST	WFPC2	555W	28.1	0.21	27.9	0.25
			28.5 – 28.0	0.15 – 0.23	28.3 – 27.8	0.18 – 0.28
	WFPC2	675W	27.5	0.55	27.3	0.66
			27.8	0.38	27.7	0.46
	WFPC2	814W	27.7	0.65	27.6	0.71
			28.1	0.45	28.0	0.49
NTT	EMMI-B	U	26.4	0.54	26.1	0.69
		B	27.4	0.47	27.1	0.62
	EMMI-R	V	27.1	0.53	26.9	0.64
		R	26.7	0.59	26.5	0.71
VLT	FORS1	R	27.0	0.45	26.8	0.54
		I	26.1	0.81	26.0	0.90

[a]Using $A_v = 0.2$ to correct for interstellar reddening.
[b]10^{-30} ergs cm^{-2} s^{-1} Hz^{-1} arcsec^{-2}

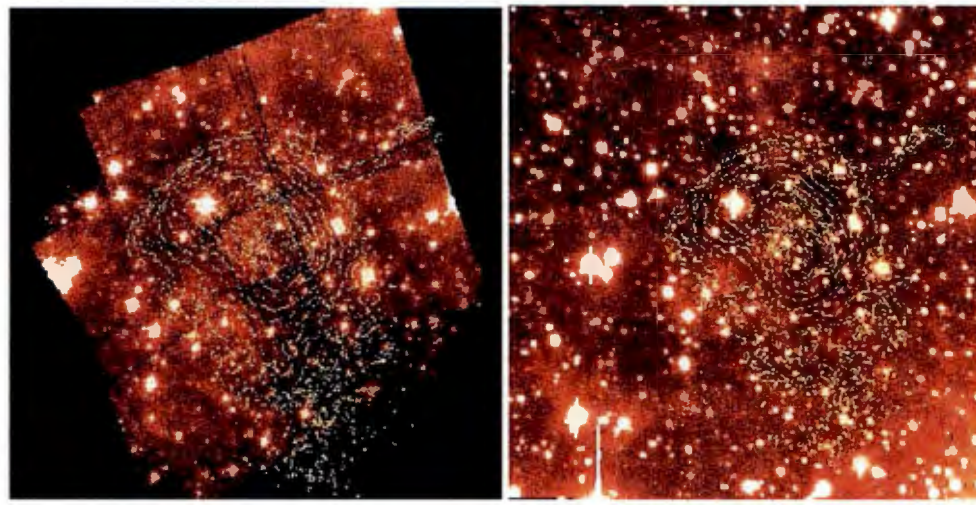

Figure 2.6: This figure shows a combined WFPC2/555W image of the Vela pulsar field. The pulsar position is located within the innermost contour. The right panel indicates a combined $UBVR$ image of the Vela pulsar field obtained from the NTT/EMMI observations. The overlayed contours correspond to the X-ray intensity maps (log scale) obtained from the *Chandra* ACIS image (1 keV to 8 keV). From Mignani et al. (2003).

telescope to study the Vela compact nebula. He compared his results with those of Ögelman et al. (1989). He obtained an optical plerionic excess for Vela, and also observed an Hα feature at the bow shock of Vela. He found an apparent excess around the pulsar position in the R band, although the jets were not as clearly visible as in the X-rays. Sefako (2002) found four prominent regions with significant excess counts: (1) the first two regions appeared to be aligned with the southern X-ray arc; (2) the other region appeared to be aligned with the X-ray jet towards the birthplace position; (3) the last region lay on the outer arc of the X-ray nebula. He found that there is a consistency in the emission process from the R to B band around the position of the pulsar, due to the good agreement between their results and those of Ögelman et al. (1989). For the region on the outer arc of the X-ray nebula, there was possibly a different emission mechanism in the R band vs. the B and V bands, because this region is only visible in the R band but not in the V and B bands covered by Ögelman et al. (1989). He obtained a flux intensity range of $F_R = 0.42 \pm 0.09$ mJy for a $1'.5 \times 0'.8$ (northsouth vs. eastwest) region, and $F_R = 1.36 \pm 0.40$ mJy for a $3'.5 \times 2'.0$ region, and $F_R = 1.04 \pm 0.26$ mJy for a $2'.0 \times 2'.0$ region. He found that the R band flux is consistent with an extrapolation of the X-ray spectrum to optical frequencies (excluding the Hα feature).

Mignani et al. (2003) analysed deep optical observations performed with *HST* WFPC2, *ESO* New Technology Telescope (NTT) and the Very Large Telescope (VLT) and compared their results with those obtained with the *Chandra* ACIS to search for extended optical emission that could be correlated with structures of the X-ray nebula elements (see Figure 2.6). They noted that there were some features seen in the optical images, but they found no correspondence to the X-ray features, nor any other symmetric features with respect to the axis of symmetry of the X-ray PWN. This led them to conclude that the diffuse optical emission was more likely associated with filaments in the host Vela SNR, and thus they did not detect the optical Vela PWN. Mignani et al. (2003) computed upper limits of 28.1 *HST* mag arcsec^{-2} for the inner nebula and $28.0 - 28.5$ *HST* mag arcsec^{-2} for the outer nebula. They found that the upper limit for the outer nebula was

slightly position-dependent. Correcting these upper limits for the interstellar reddening, assuming an extinction of $A_V = 0.2$, yielded 27.9 *HST* mag arcsec^{-2} for the inner nebula and 27.8 – 28.3 *HST* mag arcsec^{-2} for the outer nebula (assuming an area of 10 arcsec^2). Mignani et al. (2003) applied the same procedure to the WFPC2 images (675W and 814W) as well as the NTT ($UBVR$) and VLT (VI) data, but no evidence for a compact optical nebula was obtained in all of these data sets. The computed upper limits are summarized in Table 2.3. Mignani et al. (2003) concluded that a slightly deeper optical observation would allow the detection of the inner and outer arc as well as the other brightest elements of the inner PWN. However, deeper optical observations would be needed to detect emission from the full Vela PWN.

Danilenko et al. (2011) speculated that the γ-ray source in the Vela field may be a relic PWN distorted by the passage of the remnant reverse shock propagating in an inhomogeneous medium. They analysed archival mid-infrared data from the *Spitzer Space Telescope* for various channels with effective wavelengths ranging from 3.6 μm to 160 μm. They resolved a knot-like source northwest of the pulsar, and a faint counterjet extended by a few arcseconds southeast of the pulsar. The latter was clearly detected in the near-IR (Shibanov et al., 2003). These features may be associated with the PWN. Danilenko et al. (2011) found no counterparts to the X-ray torus-like structure with jets and arcs in the 3.6 μm image. The pulsar and its inner PWN were not detected at 8μm. Danilenko et al. (2011) found coincidence of the complicated eastern X-ray and radio boundary with the western boundary of the extended mid-IR emission, which suggested that they likely saw an interface between the pulsar wind and the SNR ejecta supported by a pressure balance between these two members of the remnant.

2.2.3 X-rays

Kellogg et al. (1973) observed the Vela X region and detected the X-ray source 2U 0832−45 above the 9σ level, centred on the pulsar PSR J0833−4510, and less than 1°.2 in extent using the *Uhuru* satellite. They detected marginal X-ray emission from two other localized regions within the radio complex, but did not observe diffuse emission from the Vela X-ray nebula in the *Uhuru* energy range as was detected previously below 2 keV (Seward et al., 1971). Kellogg et al. (1973) suggested that the X-ray source at the pulsar position was being excited by the rotational energy loss of the pulsar. They obtained a power law with a photon index $\Gamma = 2.1 \pm 0.3$ for the 2−10 keV range, while the extended nebula below 2 keV is fit by a power law of index 3.2 ± 0.5 (Seward et al., 1971). (Table 2.4 summarises X-ray characteristics of the Vela PWN as seen by various authors.)

Smith (1978) observed Vela X using the *Sky Survey Instrument* (*SSI*) on board *Ariel V*. The 1.6 keV to 16 keV emission revealed both an extended ($\sim 2°$) source centred on the pulsar and corresponding to the X-ray source 2U 0832−45 (Kellogg et al., 1973), and a discrete source in the vicinity of the pulsar. While the power-law fit with $\Gamma = 2.1^{+0.3}_{-0.4}$ was consistent with the spectrum measured by Kellogg et al. (1973), the flux was $\sim$ 5 times higher (see also Pravdo et al., 1976, 1978). The low efficiency of X-ray emission (compared to the pulsar's rotational energy loss rate) suggested a relatively low magnetic field in Vela nebula ($\sim 2 \times 10^{-5}$ G).

Pravdo et al. (1978) observed a small portion of the Galactic Plane using the *OSO 8* cosmic X-ray spectroscopy experiment. The X-ray source 4U 0833−45 associated with the Vela pulsar was observed at a flux which is double that reported by Kellogg et al. (1973), and its spectrum was fitted by a power law with an index of $\Gamma = 2.17^{+0.08}_{-0.04}$ in the range 2 keV to 40 keV. Pravdo et al. (1978) also noted that the lack of X-ray pulsations at the radio period, the nonthermal power-law

spectrum, and the source distribution in this region suggested that an extended synchrotron source exists around the Vela pulsar within a radius of $\sim 1°$.

Mason & Culhane (1978) investigated the X-ray source associated with PSR J0833−4510, using data from the *Copernicus* and *Ariel V* satellites. They observed an enhancement in surface brightness within $6'$ of the pulsar, and also confirmed that the X-ray emission was extended. They suggested that the spectrum of the emission originating in the neighbourhood of the pulsar was less steep than that of the entire extended source. The larger X-ray surface brightness of the central region, together with a possible harder spectrum, were indicative of synchrotron radiation from electrons accelerated by the Vela pulsar and distributed throughout the extended 2° source.

Harnden et al. (1979) observed the Vela pulsar region using the *Einstein* observatory's IPC instrument. They found that the observed field was filled with soft X-ray emission in the 0.1 keV to 0.28 keV energy range, and also found a discrete source of harder X-ray emission between 0.5 keV to 3.0 keV at the pulsar position (no pulsations). The HRI instrument revealed an $\sim 8''$ nebula centred on the pulsar, its emission strongly peaked at the pulsar position.

Knight et al. (1982) observed the region around the Vela pulsar in the energy range 15 keV to 11 MeV using the UCSD/MIT Hard X-ray and Low-Energy γ-ray Experiment on *HEAO 1*. Their 3σ upper limit was below the low-energy extrapolation of the pulsed spectrum above 50 MeV observed by the *COS B* satellite.

Table 2.4: Spectral indices inferred for different regions of Vela X from X-ray observations.

Size	Γ	Energy range (keV)	Reference
Extended nebula (5°)	3.2 ± 0.5	$\sim 0.3 - 2$	Seward et al. (1971)
$< 1°.2$	2.1 ± 0.3	$2 - 10$	Kellogg et al. (1973)
2°	$2.1^{+0.3}_{-0.4}$	$1.6 - 16$	Smith (1978)
$\sim 1°$	$2.17^{+0.08}_{-0.04}$	$2 - 40$	Pravdo et al. (1978)
$1'$	1.7 ± 0.2	$0.2 - 4.0$	Harnden & Grant (1983)
$\sim 1'$	1.7 ± 0.2	$0.03 - 2.4$	Ögelman & Zimmermann (1989)
$25'$	2.17 ± 0.13	$2.5 - 25$	Willmore et al. (1992)
$6'$	1.74 ± 0.08	$2.5 - 25$	Willmore et al. (1992)
Outer jet	1.3 ± 0.1	$1 - 8$	Pavlov et al. (2003)
Inner jet	1.09	$1 - 8$	Pavlov et al. (2003)
Inner counterjet	1.2	$1 - 8$	Pavlov et al. (2003)
Outer counterjet	$\approx 1.2 - 1.5.$	$1 - 8$	Pavlov et al. (2003)
$12' - 15'$	1.66 ± 0.01	$3 - 12.5$	Mangano et al. (2005)
	2.01 ± 0.05	$12.5 - 200$	Mangano et al. (2005)
Beyond $8'$	1.90 ± 0.06	$3 - 10$	
$0'.5 - 1'.0$	1.60 ± 0.02	$3 - 10$	Mangano et al. (2005)
$1'.0 - 1'.5$	1.61 ± 0.03		
$1'.5 - 2'.0$	1.50 ± 0.05		
PDS field of view (1.3°)	2.00 ± 0.05	$15 - 200$	
Upper cocoon region	2.13 ± 0.03	$0.2 - 6.6$	LaMassa et al. (2008)
Lower cocoon region	1.90 ± 0.02		LaMassa et al. (2008)
Northern cocoon region	$1.97^{+0.06}_{-0.05}$	$2 - 10$	Abdo et al. (2010)
Southern cocoon region	2.15 ± 0.10	$2 - 10$	Abdo et al. (2010)
Average of northern and southern region	2.06 ± 0.05	$2 - 10$	Abdo et al. (2010)
$\sim 6'$	2.00 ± 0.04	$20 - 40$	Mattana et al. (2011)
$\sim 1°.3$	2.15 ± 0.15	$20 - 300$	Mattana et al. (2011)

Harnden & Grant (1983) observed the Vela pulsar with the *Einstein* X-ray observatory. They fitted a power-law spectrum with photon index 1.7 ± 0.2, which was incompatible with the thermal plasma model which adequately described the emission from regions of the remnant. They found no evidence for pulsations, with the pulsation upper limit being 5×10^{-13} erg cm^{-2} s^{-1} at 0.2 keV to 4 keV.

Harnden et al. (1985) studied the Vela pulsar and its surrounding region using the imaging detectors of the *Einstein* X-ray observatory (0.1 keV to 4.5 keV). They found the following structures: (1) a relatively bright, asymmetrical 1° nebula of diffuse emission about the pulsar extending toward Vela X; (2) a $\sim 1'$ compact nebula of hard emission that lies between the pulsar and radio feature of Vela X; and (3) thermal emission from the entire $\sim 5°$ Vela SNR. They fitted a power law with a spectral index of $\Gamma = 1.7 \pm 0.2$ in the immediate vicinity of the pulsar, pointing to SR close to the pulsar.

Using the IPC instrument of the *Einstein* observatory, Kahn et al. (1985) found that there was a region of bright, hard X-rays (1° diameter) south of the Vela pulsar, consistent with nonthermal SR.

Ögelman & Zimmermann (1989) observed the vicinity of the Vela pulsar in the range 0.03 keV to 2.4 keV using the imaging *EXOSAT* telescope. Their X-ray map confirmed the *Einstein* results exhibiting a pointlike source centred on the pulsar (no pulsations), a compact nebula with $\sim 1'$ (they found $20''$) radius around the pulsar, and an emission region extending from the pulsar in the southwestern direction out to $\geq 3'$. In addition, they also detected a pointlike source $3'.8$ to the southwest of the pulsar. The spectrum of the compact nebula was found to be consistent with a power law with index $\Gamma = 1.7 \pm 0.2$.

Willmore et al. (1992) reported the first hard X-ray images between the energy 2.5 keV to 25 keV of the Vela SNR using a coded mask telescope flown on the *Spacelab* 2 mission. They found that the Vela pulsar was surrounded by an elongated region of diffuse X-ray emission, with a maximum extension of about 1° to the northeast and southwest, roughly aligned along the direction they thought were the pulsar spin axis (see Manchester, 1987). However, later observations showed that the spin axis is actually oriented $\sim 90°$ from this axis (Helfand et al., 2001). Willmore et al. (1992) suggested that this region, which overlaps the peak of the Vela X radio source, is a synchrotron nebula with an estimated total emission of 9×10^{-11} erg cm^{-2} s^{-1} (accounting for $\sim 48\%$ of the total emission in the 4 keV to 25 keV band). Willmore et al. (1992) determined the pulse-height spectrum of the pulsar, as well as the spectrum of the nebula using data from an annular region about the pulsar of radius $25'$; the summed spectra yielded a total spectral index of 2.17 ± 0.13, which was consistent with the result obtained by Pravdo et al. (1978). They also found a power law with $\Gamma = 1.74 \pm 0.08$ for a circle of $\sim 6'$ surrounding the pulsar. Willmore et al. (1992) argued for the identification of the 1° extended emission with a synchrotron nebula on the basis of the following arguments: (1) the X-ray emission seemed to be elongated along the direction of the pulsar rotational axis inferred by Manchester (1987), and was symmetric on either side of the pulsar; (2) its total luminosity was approximately equal to the spin-down power of the pulsar; (3) it looked different from the shell emission, and had a harder spectrum; and (4) the size was consistent with a reasonable value for the diffusion coefficient of energetic electrons near the pulsar.

Markwardt & Ögelman (1995) observed the Vela pulsar using the *ROSAT* X-ray telescope's *Position Sensitive Proportional Counter* (*PSPC*) instrument in the hard X-ray band between 0.9 keV and 2.0 keV. They found that an X-ray emitting "jet" (cocoon) began at the pulsar, with a size of

$45' \times 12'$, extending toward the south-southwest. (They originally thought that the jet extended along the pulsar spin axis, but this was later disproved by Helfand et al. (2001).) Their observations were the first to reveal that the cocoon feature was narrow, collimated, and highly symmetrical. They noted that a weaker region of diffuse emission was also present, connecting the pulsar to its apparent birthplace $\sim 8'$ to the southeast. Markwardt & Ögelman (1995) modelled the jet as emission from an optically thin thermal plasma, or as continuum emission with a power-law energy distribution, but the thermal spectral model was preferred. They found that the cocoon luminosity was 4×10^{36} erg s^{-1}, or almost 50% of the current pulsar spin-down energy. Markwardt & Ögelman (1995) noted that pulsar jets may re-energize the SNR (i.e., possibly altering its shape), and that one-sided or asymmetric jets may accelerate the NS following the supernova explosion, leading to a relatively large proper motion.

Markwardt & Ögelman (1997) observed the Vela pulsar and its surroundings using *ROSAT*, and found a collimated X-ray feature of about $45'$ in length, which was interpreted as being the cocoon of a one-sided jet from the Vela pulsar. They reported *Advanced Satellite for Cosmology and Astrophysics* (*ASCA*) observations of the Vela pulsar jet at its head, the part that is thought to interact with the Vela SNR. Markwardt & Ögelman (1997) noted that the head was clearly detected, and the cocoon's X-ray spectrum was similar to the spectrum of the surrounding Vela SNR, extending to X-ray energies of 7 keV. The lower-energy component was thermal and had a temperature of 0.29 ± 0.03 keV at a 1σ significance level. They also found that the higher-energy component had a thermal temperature of ~ 4 keV or could be described by a power law with a photon index of ~ 2.0. Markwardt & Ögelman (1997) concluded that the jet had to be entraining material in its length in order to generate a large mass flow rate.

Pavlov et al. (2001) observed the Vela PWN around the Vela pulsar using the Advanced CCD Imaging Spectrometer aboard the *Chandra X-ray Observatory*. The study revealed its complex morphology, which is reminiscent of that of the Crab PWN. Comparison of the two observations performed seven months apart revealed changes of up to 30% in the surface brightness of the PWN features. Displacement of the arcs and southwest knot, brightening of the southeast jet, dimming of the northeast knot, and brightening/dimming of the diffuse emission towards the northeast and southeast were apparent. They found some evidence for hardness ratio changes in the southeast jet of up to $\sim 30\%$ at 3.6σ significance level. They noted that it was not easy to conclude as to whether the apparent shifts of the arcs and southwest knot were associated with a steady motion of matter, or whether these were manifestations of wave phenomena, or caused by some instabilities in the post-shock relativistic plasma. They speculated that the similarity of the Vela and the Crab PWN morphologies suggested that their respective variabilities were driven by the same physical processes. However, Pavlov et al. (2001) also argued that the distinct behaviour of the various Vela PWN elements suggested that several different processes were responsible for this PWN's variability; e.g., the apparent motion of the arcs may have been caused by wave processes, while the brightness variations of the jet may have been associated with large-scale inhomogeneities of the polar outflows.

Helfand et al. (2001) observed the Vela pulsar and its environment at high resolution using *Chandra*. They found a well-resolved synchrotron nebula with a toroidal morphology similar to the one observed in the Crab nebula, as well as an axial, Crab-like jet. Figure 2.7 shows an image constructed from two observations that were centred on the Vela pulsar and summed, with the bright source representing the Vela pulsar, having an extent roughly consistent with the local point

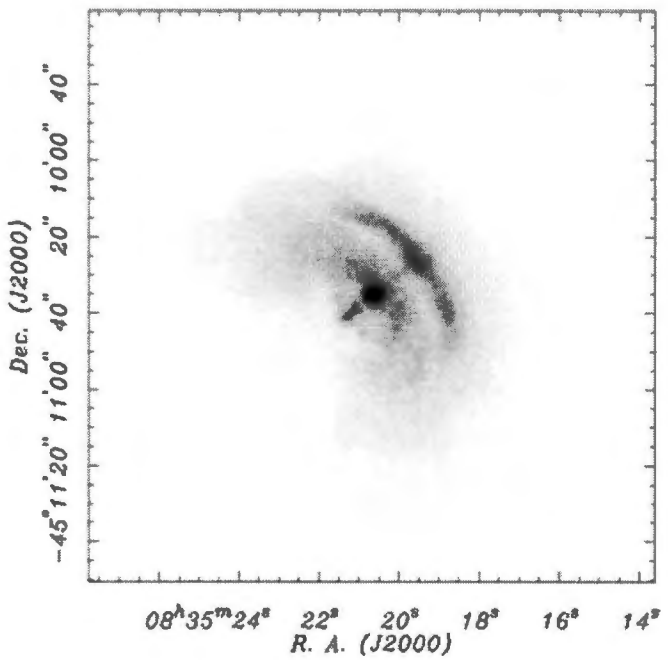

Figure 2.7: The close-up view by *Chandra* of the region surrounding the Vela pulsar. The image is centred on the pulsar and scaled to highlight the surrounding nebular emission. A toroidal structure and a perpendicular jet similar to that seen in the Crab nebula are evident, as well as a faint halo of emission likely associated with the post-shock pulsar wind. From Helfand et al. (2001).

spread function (PSF). From the pulsar position, towards the southeast, there was a linear jet-like feature with a length of $\sim 10''$. There was also evidence for a counter jet in the opposite direction. These jets had a position angle of 130° measured east of north, and were aligned to within $8° \pm 5°$ with the pulsar's proper motion vector (see Section 3.2.2). In addition, two arcs as well as diffuse emission in a "kidney-bean" shape were visible. The X-ray jet noted by Markwardt & Ögelman (1995) was overresolved, while diffuse thermal emission from the SNR was also observed. The inclination angle of the axis of the equatorial torus with respect to the line of sight was the same as that of the rotation axis of the pulsar as previously inferred from the polarization of the radio pulse. They found that the bright radio filament detected by Bietenholz et al. (1991) revealed no corresponding enhancement in X-rays. The integrated X-ray luminosity of the nebula between 0.1 keV to 10 keV was $3.5 \times 10^{32}\ d_{250}^2$ ergs s^{-1}, corresponding to 4.9×10^{-5} of the pulsar's spin-down luminosity (with $d_{250} = d/250$ pc). Helfand et al. (2001) noted that there was no significant change in count rates between the two observations, nor was there any measurable change in the count rate associated with the jet-like feature. They found that the outer arc appeared to increase in brightness by about 5% during the second observation. Helfand et al. (2001) constrained the size of the nebula to be $2''.6 \times 52''.7$, the outer arc was $20'' \times 10''$ NE−SW, and the jet was $10''$ long (SE−NW). They noted that the *Chandra* observations did not support a bow-shock interpretation, but instead favoured a physical model in which the entire structure is a synchrotron nebula, similar to the Crab, but with an important difference in the magnetization parameter (which is $\sigma \sim 1$ in this case, but expected to be $\sigma \ll 1$ for the Crab; see also Section 2.3).

Pavlov et al. (2003) observed the Vela PWN using the *Chandra X-Ray Observatory*. They

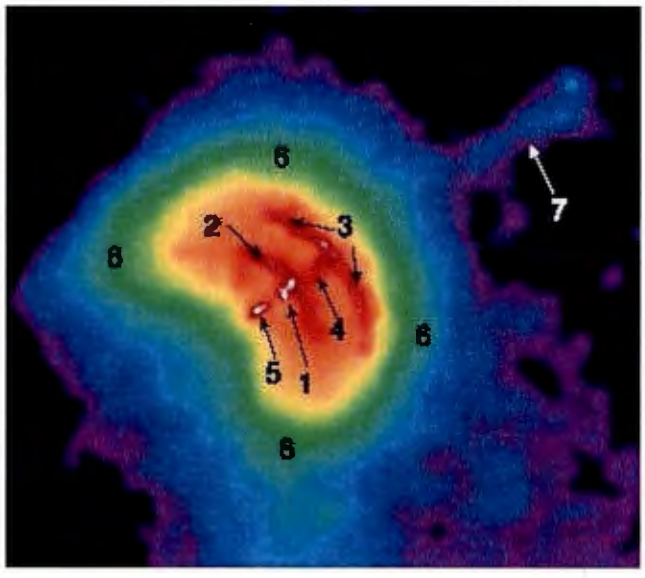

Figure 2.8: *Chandra ACIS-S3* image of the Vela PWN showing the following structural features: (1) the Vela pulsar; (2) the inner arc; (3) the outer arc; (4) the inner jet; (5) the counterjet; (6) the shell; and (7) the outer jet. From Pavlov et al. (2003).

obtained a complex, variable PWN structure, which included the central pulsar as well as inner and outer arcs (see Figure 2.8). They found that the jet was symmetrical with respect to the direction of the pulsar's proper motion, with a counterjet in the opposite direction embedded in diffuse nebular emission. The jet consisted of a bright $8''$ long inner jet between the pulsar and the outer arc, the inner counterjet, and a dim, curved outer jet extending out to $\sim 1'.7$ (brightened at its end) in approximately the same direction. The outer jet was approximately seven times brighter than the outer counterjet. This might indicate that particles from the outer jet were approaching us, while those of the outer counterjet were receding. Pavlov et al. (2003) found three types of variability in the outer jet: (1) the outer jet shifted from side to side, bending and apparently twisting; (2) the blobs moved outward along this jet; and (3) the blobs changed in brightness and eventually disappeared. The variation of the blobs over a timescale of days to weeks suggested a flow velocity of about 0.3 c–0.7 c. They obtained a power-law spectrum for the outer jet, with a photon index of $\Gamma = 1.3 \pm 0.1$, as well as average values of $\Gamma = 1.09$ and $\Gamma = 1.20$ for the inner jet and counterjet (in the 1 keV to 8 keV range). Pavlov et al. (2003) noted that the X-ray emission of the outer jet could be interpreted as synchrotron radiation of ultrarelativistic electrons/positrons with energies of up to $\sim$ 200 TeV moving in a magnetic field of about 100 μG. Pavlov et al. (2003) speculated that the outer jet was associated with a polar outflow of relativistic particles from the pulsar magnetosphere. They also observed a faint, strongly bent extension of the outer jet for the first time. They suggested that the bending of the jet could be caused by the combined action of a wind within the Vela SNR as well as ram pressure due to the pulsar's proper motion. Pavlov et al. (2003) found another feature in the image: a dim $\sim 2'$ outer counterjet, which exhibited a power-law spectrum with $\Gamma \approx 1.2 - 1.5$. They lastly observed diffuse emission from an extended region southwest of the jet and counterjet, and argued that the relativistic particles responsible for this radiation were apparently supplied by the outer jet. Pavlov et al. (2003) lastly suggested that

one may circumvent the problem of bright field stars and SNR filaments by observing the PWN in polarized light, which might result in a significant detection of the optical Vela nebula. They also noted that optical and radio polarization measurements would be helpful to constrain the pulsar's magnetic field, as well as its energetics.

Shibanov et al. (2003) detected the Vela pulsar in the near-IR using *VLT / ISAAC*. They found two faint objects in the $1''.5$ vicinity of the pulsar, which were projected on the southeast counterjet and the northwest jet of the PWN detected in X-rays. Both of them were extremely red (as seen in the IR band) and had no counterpart in the optical range. They marginally observed a thin, extended structure aligned with the inner arc of the X-ray PWN in the J_s band, and its brightness was consistent with the X-ray PWN spectrum.

Mangano et al. (2005) reported on the spectral analysis of the Vela plerion which they observed using *BeppoSAX* and *XMM-Newton* in the 3 keV to 200 keV range. They found that the hard X-ray emission above 15 keV was extended over a region having a $12' - 15'$ radius, which corresponded to a size of about $1.0 - 1.3$ pc for a source distance of 290 pc. A single power law did not give an acceptable fit to the combined dataset. A broken power law, with photon indices of $\Gamma_1 = 1.66 \pm 0.01$ (below $E < E_b$) and $\Gamma_2 = 2.01 \pm 0.05$ up to about 200 keV, and a break energy of $E_b = 12.5$ keV, gave an acceptable fit. Mangano et al. (2005) observed diffuse and asymmetric emission beyond an $8'$ radius in the southeastern and southwestern directions, which is possibly correlated with the radio structure (Dodson et al., 2003a). From 3 annuli (3 keV to 10 keV) between radii $(0'.5 - 1'.0, 1'.0 - 1'.5, 1'.5 - 2'.0)$ they found an average spectral index of $\Gamma = 1.60 \pm 0.02$, compared to $\Gamma = 1.9$ for distances beyond $8'$. Mangano et al. (2005) fitted the PDS spectrum in the energy range 15 keV to 200 keV and obtained a photon index of $\Gamma = 2.00 \pm 0.05$, which indicated that a spectral steepening occurs at higher energies. They found that the SED of the Vela PWN in the 3 keV to 200 keV range was only marginally consistent with the *EGRET* upper limits reported by Kanbach et al. (1994) when they extrapolated their fit to the combined MECS–PDS dataset to the *EGRET* range. The plerion spectrum should therefore show another break or cut-off in the 200 keV to 10 MeV range (for an alternative interpretation invoking two electron populations, see Figure 2.9). The discrepancy with the X-ray data of Willmore et al. (1992) was explained by them having a smaller source extension, with an extraction radius of $4'$. Mangano et al. (2005) found that their measured luminosity was more than a factor two higher than that inferred from *OSSE* results. The discrepancy with the *OSSE* results was possibly because of a systematic effect in the *OSSE* instrument due to its wider field of view. Lastly, they reported that the upper limits for the optical nebula (Mignani et al., 2003) were consistent with the low-frequency extrapolation of the inner plerion spectrum.

LaMassa et al. (2008) used *XMM-Newton* archival data covering the southern portion of the Vela PWN, and analysed the X-ray properties of the collimated X-ray filament (cocoon) extending south-southwest from the pulsar to the centre of Vela X. They found a two-component spectrum consisting of a thermal and a nonthermal component, the latter having a spectral index of $\Gamma = 2.30 \pm 0.04$. They also constructed spectra for the upper and lower regions of the portion of the cocoon covered by their observations. They found a variation in spectral index, with $\Gamma_{\rm upper} = 2.13 \pm 0.03$ and $\Gamma_{\rm lower} = 1.90 \pm 0.02$, consistent with the findings of Markwardt & Ögelman (1997). This is counterintuitive, since the spectrum is steepening with distance, rather than softening due to energy losses suffered by the radiating particles, and may be caused by the crushing of the cocoon against the PWN, leading to adiabatic heating that hardens the spectrum (however, see

results of Abdo et al. (2010) below). Their analysis showed enhanced abundances of Oxygen (O), Neon (Ne), and Magnesium (Mg) within the cocoon, indicating the presence of ejecta-rich material resulting from the propagation of the SNR reverse shock. This was consistent with Vela X being a disrupted PWN: the Vela radio nebula extended southward of the pulsar, suggesting that the northern portion had been disturbed by an interaction with the SNR reverse shock.

Abdo et al. (2010) noted that the spectral extraction regions of several of the older X-ray and soft γ-ray observations (Harnden et al., 1985; Levine et al., 1984; De Jager et al., 1996b; Mangano et al., 2005) were centred on the Vela pulsar, such that the bright inner PWN contaminated the low-surface-brightness extended nebula, and artificially hardened the total spectrum. They therefore reanalysed *ASCA* data and found a thermal component with $kT = 0.51^{+0.05}_{-0.04}$ keV, plus a power law (2 keV to 10 keV) with index $\Gamma = 1.97^{+0.06}_{-0.05}$ in the north and $\Gamma = 2.15 \pm 0.10$ in the south. This steepening of the photon index with distance from the pulsar provided weak evidence for aging of the electron population as it moved along the cocoon. The average index for the northern and southern region was $\Gamma = 2.06 \pm 0.05$ and the 2 keV to 10 keV flux was $(6.7 \pm 0.4) \times 10^{-11}$ erg cm^{-2} s^{-1} (see lower panel of Figure 2.9).

Mattana et al. (2011) reported on the *INTEGRAL* discovery of extended emission beyond the inner PWN above 18 keV. They also found a 110σ pointlike source at the pulsar position. The extended emission followed the structure found by Willmore et al. (1992). They also found that the northern side was without known counterparts in other wavebands, and it appeared larger and more significant than the southern one, which in turn was partially coincident with the "cocoon". They inferred a single power law with photon index $\Gamma_{\rm ISGRI} = 2.00 \pm 0.04$ and a flux $F = (4.76 \pm 0.09) \times 10^{-11}$ erg cm^{-2} s^{-1} for a pointlike source between 20 keV and 40 keV. They found that the spectrum was about 50 times higher than the phase-averaged one of the Vela pulsar at 20 keV, which implied that the *IBIS/ISGRI* emission was dominated by the nebula. They also used data from the *INTEGRAL* spectrometer *SPI* and fitted a power-law model with photon index of $\Gamma_{\rm SPI} = 2.15 \pm 0.15$, compatible within the errors with the *IBIS/ISGRI* spectrum, but with a higher flux of $F = (9.1 \pm 0.6) \times 10^{-11}$ erg cm^{-2} s^{-1} in the energy range 20 keV to 40 keV. This index was compatible with that found by Mangano et al. (2005) using *BeppoSax* ($\Gamma = 2.00 \pm 0.05$). Mattana et al. (2011) also found a broken power law, with a break at $\sim$ 25 keV, describing emission within $6'$ from the pulsar after including the *Suzaku XIS* data. They found that the change of slope around 25 keV was compatible with the standard value of 0.5 expected from a cooling break occurring for an electron distribution continuously injected for the last $\sim$ 2 000 years. (Electrons older than $\sim$ 2 000 years will therefore have escaped from the region within $6'$ from the pulsar.) Lastly, they noted that the northern emission might be due to fresh particles injected after the passage of the reverse shock, with $B > 10$ μG for this region.

2.2.4 γ-rays

Grenier et al. (1988) used the *COS-B* dataset of the Vela pulsar, encompassing the energies 50 MeV to 5 GeV, and obtained upper limits for the unpulsed flux ranging between $6\% - 9\%$ of the pulsed flux. Kanbach et al. (1994) used the *Energetic Gamma Ray Experiment* (*EGRET*) to observe the Vela pulsar and obtained upper limits to the unpulsed flux, between 300 MeV and 4 GeV, ranging from $2\% - 51\%$ of the pulsed flux.

De Jager et al. (1996a,b); Strickman et al. (1996) detected soft γ-rays from the Vela SNR at a significant level of $\sim 9\sigma$ using the *Oriented Scintillation Spectrometer Experiment* (*OSSE*)

instrument on board the *Compton Gamma Ray Observatory* (*CGRO*) satellite. They obtained an unpulsed spectrum after subtracting the pulsed one from the total spectrum, and fitted this unpulsed spectrum between 0.061 MeV and $\sim$ 0.4 MeV using a power law with a steep photon index of $\sim 1.6 \pm 0.3$. This result was consistent with an extrapolation of the $\sim E^{-1.7}$ spectrum of the 1′ compact nebula as observed between optical and 25 keV energies with imaging instruments. De Jager et al. (1995) reanalyzed *EGRET* data, and found upper limits which constrained the cutoff energy of the power law to $\leq$ 30 MeV. De Jager et al. (1996b) observed that the unpulsed spectrum dominated the pulsed spectrum significantly in the *OSSE* range, while the *EGRET* observations revealed no significant unpulsed emission. De Jager et al. (1995) noted that the electrons therefore had to escape from the compact nebula before losing all energy to radiation. No spectral break resulting from synchrotron losses was observed between $\sim$1 eV and 0.4 MeV, although several arguments indicated that this spectrum should cut off below 40 MeV.

Strickman et al. (1996) also scanned the Vela pulsar region using the *HEAO A-4* detector. They found a spectrum which was inconsistent with the one observed by *OSSE*. They concluded that the total Vela spectrum (corresponding to the extended nebula) had a spectral index of ~ 2.2 below $\sim$ 20 keV, and steepened significantly above $\sim$ 20 keV, to a spectral index of $\Gamma = 2.7$, but then hardened above $\sim$ 60 keV to meet the *OSSE* spectrum with $\Gamma = 1.8$ (corresponding to the 1′ compact nebula). Strickman et al. (1996) noted that if they extrapolated the *EINSTEIN* spectrum to the *OSSE* 0.1 MeV range, the expected flux at 100 keV was 3.6×10^{-3} cm^{-2} s^{-1}, which agreed with the amplitude of the *OSSE* spectrum, but with a larger error on the extrapolated flux.

Yoshikoshi et al. (1997) observed the Vela pulsar region at TeV energies using the 3.8 m CANGAROO-I imaging atmospheric Cherenkov telescope. They detected an integral flux of $(2.9 \pm 0.5 \pm 0.4) \times 10^{-12}$ photons cm^{-2} s^{-1} (where the first error represents the statistical error on the fit parameters, and the second one is the systematic uncertainty) above 2.5 ± 1.0 TeV at the 5.8σ level, with the photon index of the power-law spectrum being 2.5, and the maximum γ-ray energy was 10 TeV. These results were non-variable over two years. The γ-ray emission region was offset by about 0°.13 to the southeast of the Vela pulsar position. Dazeley et al. (2001), however, later disputed these results.

Enomoto et al. (2006) observed the Vela pulsar region with the 10 m CANGAROO-III stereoscopic imaging atmospheric system. They found no evidence of γ-ray emission from either the pulsar position or the previously reported position offset by 0°.13 from the pulsar, and their resulting upper limit was a factor of five less the previously reported by Yoshikoshi et al. (1997), assuming an $E^{-2.5}$ spectrum. They also reported TeV emission above 600 GeV from the PWN at a

Table 2.5: Spectral indices inferred for Vela X using γ-ray observations.

Size	Γ	Energy range	Reference
1′	1.6 ± 0.3	0.061 – 0.4 MeV	De Jager et al. (1996a,b), Strickman et al. (1996)
$\sim 5°$ FoV	2.2	$\leq$ 20 keV	Strickman et al. (1996)
$1°.2 \times 20°$ FoV	2.7	$\geq$ 20 keV	Strickman et al. (1996)
$3°.8 \times 11°.4$ FoV	1.8	$>\sim$ 60 keV	Strickman et al. (1996)
$\sim 3°$ FoV	2.5	$> 2.5 \pm 1.0$ TeV	Yoshikoshi et al. (1997)
$0°.48 \times 0°.36$	$1.45 \pm 0.09 \pm 0.2$	550 GeV – 65 TeV	Aharonian et al. (2006a)
$1°.5 \times 1°$	1.67 ± 0.25	100 MeV – 3 GeV	Pellizzoni et al. (2010)
$0°.88 \pm 0°.12$	$2.41 \pm 0.09 \pm 0.15$	200 MeV – 20 GeV	Abdo et al. (2010)

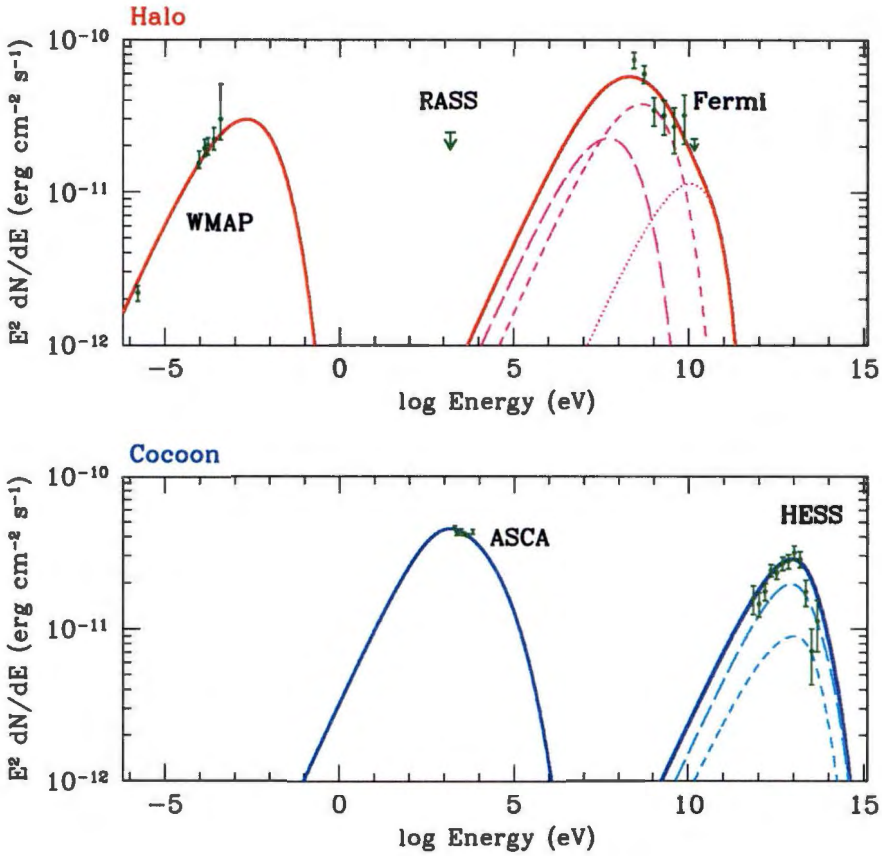

Figure 2.9: SED of regions within Vela X from radio to VHE γ-rays. The upper graph shows emission from the low-energy electron population, including an X-ray upper limit. Lower graph: SR and IC components resulting from the HE electron population (cocoon). From Abdo et al. (2010).

4σ level, peaking $\sim 0°.5$ south of the pulsar position and having an extension of $\sim 0°.6$, consistent with the H.E.S.S. report (below).

Aharonian et al. (2006a) observed the Vela X region to the south of the Vela pulsar using the High Energy Stereoscopic System (H.E.S.S.), and fitted a spectrum between 550 GeV and 65 TeV with a photon index of $\Gamma = 1.45 \pm 0.09_{stat} \pm 0.2_{sys}$ and an exponential cutoff at an energy of $13.8 \pm 2.3_{stat} \pm 4.1_{sys}$ TeV for an integration region of $0°.8$. They also obtained an integral flux above 1 TeV of $(1.28 \pm 0.17 \pm 0.38) \times 10^{-11}$ cm^{-2} s^{-1}. The best-fit intrinsic size of the VHE source was $0°.48 \times 0°.36$ (i.e., 58×43 arcmin^2 vs. the X-ray size of 42×12 arcmin^2; Markwardt & Ögelman, 1995). The major axis of the source was at a position angle of $41° \pm 7°$. This source furthermore coincided with the hard X-ray emission observed by *ASCA* and *ROSAT* and Section 2.2.3). Aharonian et al. (2006a) claimed that their results represented the first measurement of a peak in the SED from a VHE source, and that this emission was likely associated with inverse Compton radiation.

Yoshikoshi et al. (2009) reanalysed data from observations of the Vela pulsar region made with CANGAROO-I in response to the new H.E.S.S. results on Vela X. The H.E.S.S. detection of strong diffuse TeV γ-ray emission differed morphologically from the CANGAROO-I source. Yoshikoshi et al. (2009) detected Vela X at a 4.5σ significance, and deduced that their new results were morphologically and positionally comparable to the earlier ones, although the H.E.S.S. source

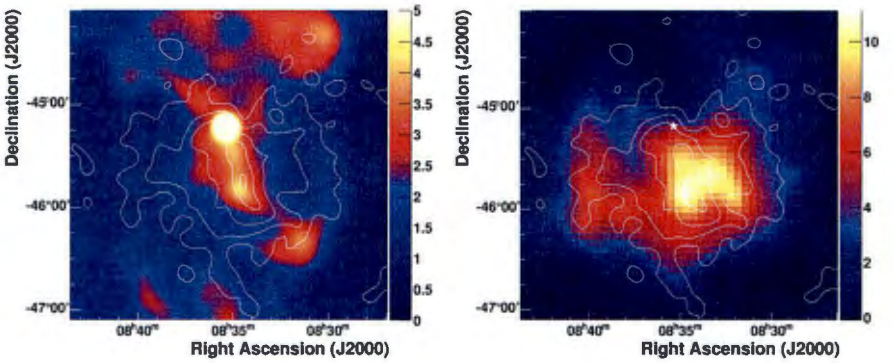

Figure 2.10: Left: Gaussian-smoothed *ROSAT* skymap at energies $E >$ 1.3 keV. Right: radio skymap at 2.4 GHz as measured by the *Parkes* telescope. White contours correspond to VHE γ-ray surface brightness contours. From Abramowski et al. (2012).

emission was more diffuse than that of CANGAROO-I, and the peak emission was slightly offset. This is due in part to the different energy thresholds of the two telescopes. Yoshikoshi et al. (2009) concluded that the γ-ray integral flux from the 1993 – 1995 data of CANGAROO-I, for the same region as defined by H.E.S.S., was $F(> 4.0 \pm 1.6 \text{ TeV}) = (3.28 \pm 0.92) \times 10^{-12}$ photons cm^{-2} s^{-1}, which is statistically consistent with the integral flux obtained by the latter.

Pellizzoni et al. (2010) detected the Vela PWN in the energy range from 100 MeV to 3 GeV using *Astro-rivelatore Gamma a Immagini Leggero* (*AGILE*). They defined the off-pulse window for the Vela pulsar to be 0.65 to 1.05 in normalized phase, and searched for faint emission in this window, thereby excluding the bright pulsed emission. Pellizzoni et al. (2010) detected the source AGL J0834−4539 at $\sim 5.9\sigma$ significance with a flux of $(3.5 \pm 0.7) \times 10^{-7}$ cm^{-2} s^{-1} above 100 MeV, located $\sim 0.5°$ southwest of the pulsar, having an extent of $1°.5 \times 1°$. This source was positionally coincident with the H.E.S.S. source, and was therefore identified with the Vela X PWN, also exhibiting a similar brightness profile. They fitted a power-law spectrum with a photon index of 1.67 ± 0.25 and their spectral points were a factor two below the previous *EGRET* upper limits (Kanbach et al., 1994). Pellizzoni et al. (2010) lastly noted that the *AGILE* measurements implied multiple electron populations responsible for the broadband SED, as suggested by De Jager et al. (2008) in the context of leptonic models (see Section 2.3).

Abdo et al. (2010) detected γ-ray emission in the 200 MeV to 20 GeV range at the 14σ level from a $2° \times 3°$ area south of the Vela pulsar using the *Fermi* Large Array Telescope (LAT), and identified this source with the Vela X PWN. The flux was significantly spatially extended with a best-fit radius of $0°.88 \pm 0°.12$ for a uniform disc morphology. The spectrum was well described by a power law with a spectral index of $2.41 \pm 0.09 \pm 0.15$, giving an integral flux above 100 MeV of $(4.73 \pm 0.63 \pm 1.32) \times 10^{-7}$ cm^{-2} s^{-1} (see Figure 2.9). These results (in addition to the fact that the LAT source morphology did not correspond well to the H.E.S.S. one) also favoured a scenario where two distinct electron populations are responsible for the multiwavelength SED.

Abramowski et al. (2012) re-observed Vela X with H.E.S.S. including larger offsets from the cocoon to probe the extent of the nonthermal emission at TeV energies and also to investigate its spectral properties. They used a multivariate analysis method to select γ-ray events, as well as the so-called On/Off background method to estimate the background from separate observations pointing away from Vela X and toward source free regions. They found a γ-ray excess above

0.75 TeV for the total source extending out to a radius of °.2 having a significance of 27.9σ, and in the ring between the radii 0°.8 and 1°.2 around the central position a 7.5σ significance level was measured. Abramowski et al. (2012) found that the spectra of the inner region and ring were consistent and may be described by a power law with a index $\Gamma = 1.32 \pm 0.06_{stat} \pm 0.12_{sys}$ and an exponential cutoff energy of $14.0 \pm 1.6_{stat} \pm 2.6 sys$ TeV. They found no significant spectral variations within Vela X, suggesting that particle escape and/or reacceleration may be taking place. The source extent has also been revised: the VHE profile along the major axis is well fit by a single Gaussian of width $0°.52 \pm 0°.02$ while the profile along the minor axis is fit by two Gaussians of width $0°.60 \pm 0°.04$ and $0°.12 \pm 0°.02$. The VHE morphology therefore now seems to be intermediate between the X-ray cocoon and radio morphologies (see Figure 2.10). This may be explained by two distinct electron populations, one being responsible for the radio and part of the VHE emission, and the other giving rise to the X-ray as well as a part of the VHE emission. Comparison of this new VHE morphology with that measured by *Fermi* LAT implies some revision of the two-population leptonic model of De Jager et al. (2008).

2.3 Modelling of the Vela Plerion

Using *OSSE* data, De Jager et al. (1996a) constrained the pulsar magnetic field using several arguments, including the lack of a spectral break between the optical and 0.4 MeV energy range, the symmetrical shape of the compact nebula at radius $1'$, and the survival of electrons from the expected birthplace of the pulsar. Using these arguments, they found an average PWN B-field of $\langle B \rangle = 30 - 100$ μG. This is close to the equipartition B-field $B_{\rm eq} \sim 60$ μG. They also found that $W_{\rm particle} \sim 0.5 W_{\rm pulsar}$, where $W_{\rm particle}$ is the total energy of the particles, and $W_{\rm pulsar}$ is the total energy of the pulsar. Roughly ~ 0.5 of the spin-down power is therefore converted into electrons/positrons, and only about $\sim 0.2\%$ of energy in electrons is radiated away. These electrons therefore escape from the compact nebula before losing much of their energy to SR. The extension of the compact nebula SR spectrum to an energy of about 0.4 MeV implied electron energies of up to $\sim 3 \times 10^{14}$ eV, which is a factor 10 below the maximum acceleration energy of 3.5×10^{15} eV set by the polar cap vacuum potential. This furthermore implied that the acceleration mechanism should be relatively efficient for particles to attain up to 10% of the available potential drop.

Blondin et al. (2001) considered the evolution of a PWN inside an SNR, and constructed a simple model based on the expanding pulsar bubble solution (Chevalier, 1977) and the self-similar driven wave (Chevalier, 1982). They carried out one- and two-dimensional, two-fluid simulations of the crushing and re-expansion phases of a PWN. They used two different values for γ (adiabatic index) such that the pulsar wind was modeled with $\gamma = 4/3$, and the supernova ejecta and circumstellar gas was modeled with $\gamma = 5/3$. They allowed for a power-law outer density profile as well as a density gradient in the surrounding thermal medium. They showed that: (1) the crushing and reexpansion phases of the PWN are subject to Rayleigh-Taylor instabilities that result in the mixing of thermal and nonthermal fluids; and (2) asymmetries in the surrounding interstellar medium give rise to asymmetries in the position of the PWN relative to the pulsar and explosion site (forming a so-called "offset PWN"). They found that the displacement of the PWN from the pulsar can be explained in their model without the need for directed power from the pulsar. They also found that the asymmetries in the placement of radio PWNe relative to their pulsars are likely to be common in this phase, since the interstellar medium is generally inhomogeneous. Blondin et al.

(2001) noted that Vela X is likely to be in a post-reverse-shock phase in the Vela SNR. The overall appearance of Vela X is chaotic, in keeping with the expected instabilities during the crushing and reexpansion phases of their model. Blondin et al. (2001) furthermore expected that for their reverse-shock model, the pressure in the PWN should be comparable to the pressure in the hot gas in the Vela remnant; observations indicate that this is approximately the case.

Helfand et al. (2001) proposed an explanation for the X-ray structure of the Vela synchrotron nebula, where the bright X-ray arcs are the shocked termination of a relativistic equatorial pulsar wind, and are contained within the surrounding kidney-bean-shaped synchrotron nebula comprising the postshock, but still relativistic, flow. They allowed the magnetization parameter (σ) to be of order unity, consistent with the simplest magnetohydrodynamic (MHD) transport of the magnetic field from the pulsar to the PWN, with $B \leq 4 \times 10^{-4}$ G. They applied the model of Kennel & Coroniti (1984a), originally developed for the Crab, to Vela. In this model, a relativistic pulsar wind terminates in a MHD shock, which produce the nonthermal distribution of particles as well as the postshock magnetic field, forming the synchrotron nebula. The Helfand et al. (2001) model provides a plausible explanation for the toroidal arcs and outer nebula, but it cannot explain the jet and counterjet.

Sefako & De Jager (2003) presented a model for the SR from the Vela compact nebula enabling them to derive pulsar/plerion parameters such as the pair production multiplicity M (number of secondary pairs spawned by a single accelerating primary) and wind magnetization parameter σ. They found that $300 < M < 700$, whereas the magnetization parameter is constrained to lie between $0.05 < \sigma < 0.5$. Sefako & De Jager (2003) noted that M was too small to be explained by curvature radiation losses in the open magnetosphere of Vela, and noted that the presence of optical pulsed photons could modify this predicted multiplicity. Mangano et al. (2005) obtained an X-ray luminosity which was higher than that assumed by Sefako & De Jager (2003), implying a higher number of particles and consequently a higher value of M for the Vela plerion.

Bednarek & Bartosik (2003) investigated radiation processes inside SNRs which are powered by young pulsars using a model for particle acceleration inside PWNe where heavy nuclei may carry a significant part of the energy lost by the pulsar, excite waves just beyond the pulsar wind shock, and lastly transfer this energy to positrons via resonant scattering. They constructed a time-dependent radiation model where the injection spectra of relativistic leptons and nuclei depend on the pulsar evolution, and these particles are in turn injected into the expanding surrounding nebula. The central pulsar's parameters are influenced by the pulsar's rotational energy loss, while the nebular parameters are detemined by the SNR's intial kinetic energy, the pulsar's energy supply, and the surrounding medium properties. By taking into account radiation (SR, IC, and bremsstrahlung) and adiabatic energy losses (also collisional losses and fragmentation of nuclei) as well as particle escape from the nebula, they obtained steady-state spectra of leptons and nuclei, and calculated the multiwavelength photon spectrum produced by these, comparing the latter with broadband observations of several PWNe. In the case of Vela, they first injected leptons into the inner nebula with average B-field of 40 μG, and then into the large-scale SNR where the B-field is $\sim$ 5 μG, obtaining an SR and IC (mostly due to CMB scattering, with the contribution from Synchrotron Self-Compton radiation on the nebular SR photons being negligible) spectrum from each region. They found that the HE γ-ray emission is mainly due to leptons in the SNR (because of enhanced containment there), while the contribution from the decay of neutral pions produced during the collision of nuclei is significantly lower in this model, becoming only significant around $\sim$10 TeV.

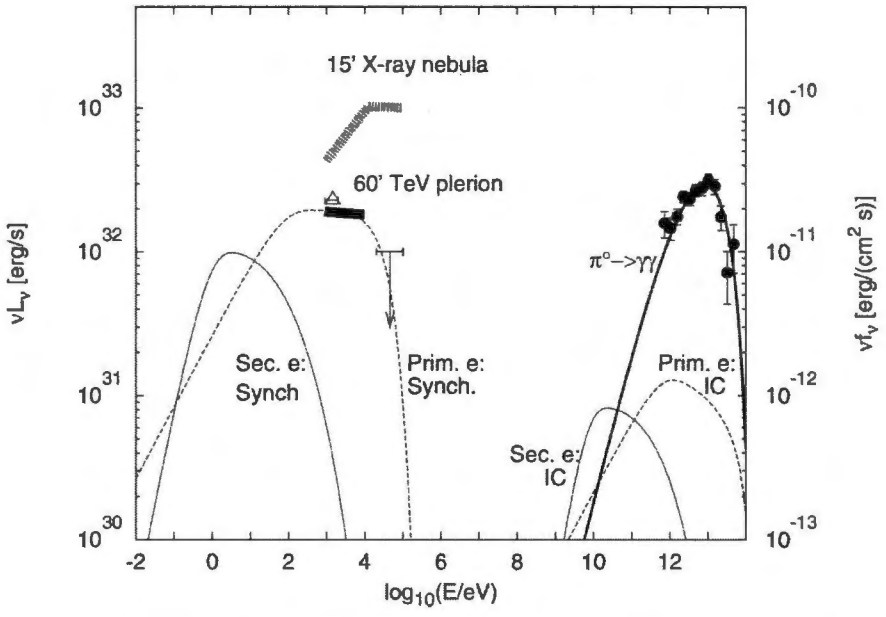

Figure 2.11: Hadronic model: SED which includes the γ-ray emission from π^0 decay, as well as SR and IC emission from primary and secondary electrons in a 10 μG field. The downward pointing arrow is a 90% upper limit from INTEGRAL ISGRI data (20 keV to 60 keV) from the TeV plerion. The broad dashed curve indicates the combined *XMM-Newton* and *BeppoSAX* spectrum from the compact nebula (Mangano et al., 2005), the open triangle is the *ROSAT* measurement as given by Markwardt & Ögelman (1995), and the thick solid line represents extended hard X-ray emission observed by *ASCA*. From Horns et al. (2006) .

Horns et al. (2006) invoked a hadronic scenario to model the Vela PWN (where protons or heavier nuclei interact to give π^0 particles, which in turn decay into γ-rays, e.g. $p + p \rightarrow \pi^0 + ... \rightarrow 2\gamma$...). They found that the total required energy in the protons ranges from $10^{48} - 10^{49}$ erg, where the lower value corresponds to an iron-loaded and the higher value to a proton-loaded wind. This energy is approximately equal to the integrated spin-down luminosity of the pulsar (which is $5 \times 10^{48} - 5 \times 10^{49}$ erg, for a braking index $n_b = 1.4 \pm 0.2$). They suggested that secondary electrons resulting from the inelastic (proton-proton) interactions may produce SR in the optical to soft X-ray band. Horns et al. (2006) assumed the magnetic field to be constrained to $\approx$10 μG in order to avoid significant energy losses due to escaping particles. They noted that the presence of a thermal X-ray emitting plasma was consistent with a plasma density of 0.6 cm^{-3}. (However, LaMassa et al. (2008) found a thermal particle density at the head of the cocoon of only 0.1 cm^{-3}, implying that the γ-ray flux due to proton-proton interactions should be less by a factor 6.) Horns et al. (2006) furthermore assumed that the differential injection spectrum of the hadrons is close to a mono-energetic distribution. They also included a radiatively-cooled primary electron component that originated from the pulsar wind with a total energy of 10^{45} erg. This particle population may contribute to the IC and SR radiation components. See Figure 2.11 for their calculated spectra.

De Jager (2007) criticized the hadronic scenario on three counts: (1) Horns et al. (2006) assumed $B = 10$ μG yielding an SR loss timescale of 400 yrs, much smaller than the timescale of $\sim$ 3 000 yrs for the SNR reverse shock to crush the PWN; (2) the assumed volume filled by hadrons was underestimated, and the revised ion energy budget exceeds the total integrated rotational energy

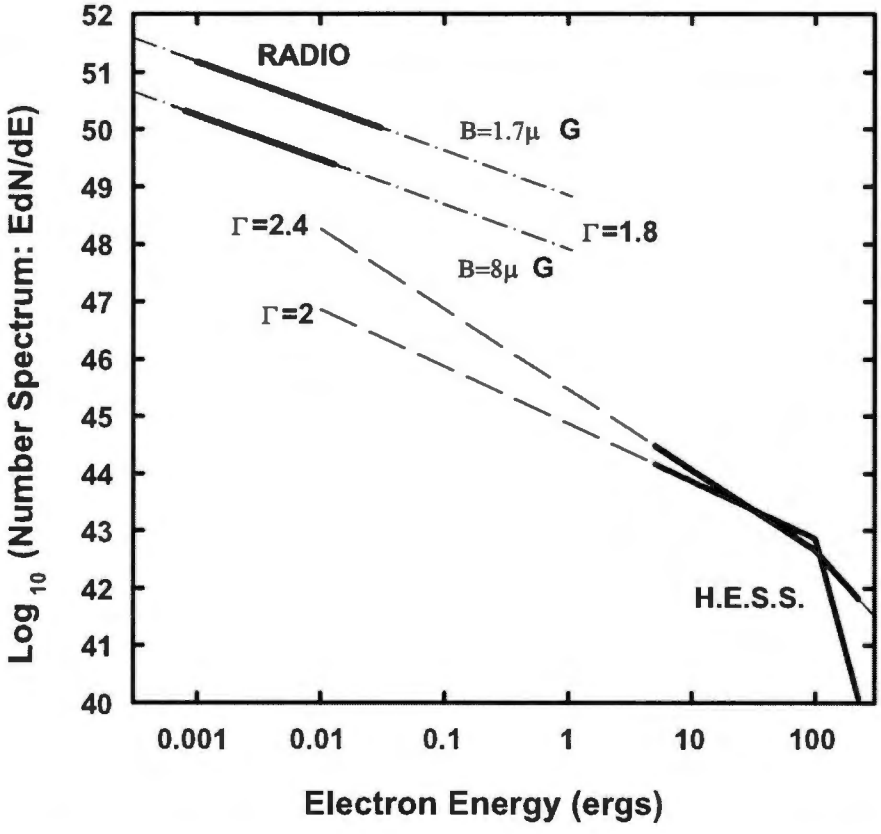

Figure 2.12: Electron spectra of Vela X derived from H.E.S.S. and radio observations. The two top thick solid lines represent the electron energy ranges that contribute to the observed radio synchrotron emission between 30 MHz and 8.5 GHz for the two field strengths of 1.7 μG and 8 μG. The two lower H.E.S.S. lines correspond to the two possible spectral fits discussed by Aharonian et al. (2006b), with $\Gamma = 2.0$ and 2.4 representing the two possible electron spectral indices (assuming IC scattering of VHE electrons, mostly on the cosmic microwave background (CMB)). The missmatch between the electron spectra in the low-energy and high-energy ranges argues for two distinct electron populations responsible for the broadband emission from Vela X. From De Jager (2007).

of the pulsar since birth; (3) Horns et al. (2006) noted that the conversion efficiency of pulsar spin-down energy to leptons was very low. However, by decreasing B, reasonable values were found for this efficiency. Using radio and γ-ray data, De Jager (2007) constrained the pair production multiplicity factor to $0.5 < M < 5 \times 10^5$. He used the VHE γ-ray spectrum of Vela X, since the IC-generated γ-ray spectrum is free from assumptions about the associated nebular magnetic field strength. On the other hand, the extreme brightness of Vela X in radio indicated that most of the electrons from the pulsar have been reprocessed into the radio synchrotron domain, which leads to an upper limit of $\langle M \rangle < 5 \times 10^5$ (corresponding to a minimal field strength of 1.7 μG). He argued for two electron populations being responsible for the radio SR and γ-ray IC emission, on the basis that the electron spectra inferred from these two radiation components did not match after extrapolation (see Figure 2.12).

LaMassa et al. (2008) applied a leptonic model, and found that two spectral components were required to fit the broadband spectrum, namely: (1) the radio and nonthermal X-ray emission

could be explained by SR; (2) the γ-ray emission was explained by IC scattering of electrons on CMB photons. They used a three-component broken power-law electron injection spectrum to account for the SR and found an intrinsic break in the electron spectrum at $\sim 5{\times}10^6$ keV and a cooling break at $\sim 5.5 \times 10^{10}$ keV. They noted that the cooling break together with a magnetic field strength of 5 μG indicated that a synchrotron break should occur at ~ 1 keV.

De Jager et al. (2008) constructed a time-dependent postshocked injection spectrum $Q(E,t)$, where E is the lepton energy, consisting of two components: $Q_{\rm R}(E,t)$ as a source for the extended radio emission, and $Q_{\rm X}(E,t)$ as a source for the X-ray and VHE γ-ray emission, confined to the cocoon region. They derived $B = 5$ μG from the VHE spectral break, while the radio spectral index of $\alpha = -0.39$ required a particle index of $p = 1.78$ for SR. Their lepton spectrum for the X-ray/VHE γ-ray emission region was constrained as follows: the injection (uncooled) lepton spectral index should be $p = 2.0$ to reproduce the uncooled photon spectral index of 1.5; the IC normalization of the cocoon spectrum as provided by Aharonian et al. (2006a); the multi-TeV break energy observed by H.E.S.S.; spin-down from P_0 to the current period of 89 ms within a time of $T \sim 11 - 15$ kyr implying a time-averaged conversion efficiency of $\eta_{\rm X} = 3 \times 10^{-3}$; and a field strength of $B = 5$ μG to produce the observed VHE break energy. In Figure 2.13, one observes that the modelled X-ray synchrotron spectrum has a break around 1 keV about ($2 - 3 \times 10^{17}$ Hz) and also matches the 20 keV to 300 keV *INTEGRAL* flux to within a factor of 2. (This ccorrespondence between the model and the *INTEGRAL* spectrum may be even closer when the pulsar flux contribution is carefully subtracted; private communication, W. Hermsen.) The H.E.S.S. spectrum is matched, while a spectral component is predicted in the *Fermi* range (observations seem to favour the top prediction for the radio and HE γ-rays; Abdo et al. (2010)).

Qiao et al. (2009b) calculated SR and IC radiation by electrons coming directly from the pulsar magnetosphere, and being accelerated at the termination shock. They applied this model to produce the observed multi-waveband photon spectrum of Vela X. The results of Qiao et al. (2009b) indicated that nonthermal emission ranging from the radio to X-ray band may originate from the SR of nonthermal electrons, while the VHE γ-rays may be produced through IC scattering.

Zhang & Yang (2009) studied nonthermal emission properties of Vela X in both a leptonic and hadronic-leptonic model. Their (single-component) leptonic calculations (following closely the work of Büsching et al. (2008) and Zhang et al. (2008)) implied two sets of model parameters, where the first set could only reproduce the observed spectrum in the TeV band, while the second set could only reproduce the feature in the X-ray band. They could, however, reproduce the SED of Vela X in the framework of the hadronic-leptonic model (building on results of Bednarek & Bartosik (2003)), finding that the TeV photons mainly originate from π^0 decay following proton-proton interactions. Zhang & Yang (2009) lastly noted that their model predicts a weaker GeV source if its TeV photons have a hadronic origin, compared to a leptonic origin.

Hinton et al. (2011) developed a model that for the first time related the X-ray cocoon and the extended radio nebula (ERN) through continuous injection of particles with a fixed spectral shape and fixed conversion efficiency. They argued that the diffusive escape of particles from the ERN can explain the steep *Fermi* LAT spectrum, and also noted that energy-dependent escape from Vela X should produce a distinct feature in the locally measured cosmic ray (CR) electron spectrum in the VHE band. Hinton et al. (2011) noted three unexplained observational facts: (1) the steep GeV spectrum indicating an unexplained absence of > 100 GeV energy particles from the ERN; (2) the relative dimness of the TeV nebula; (3) the lack of spectral variation across Vela X above 1 TeV,

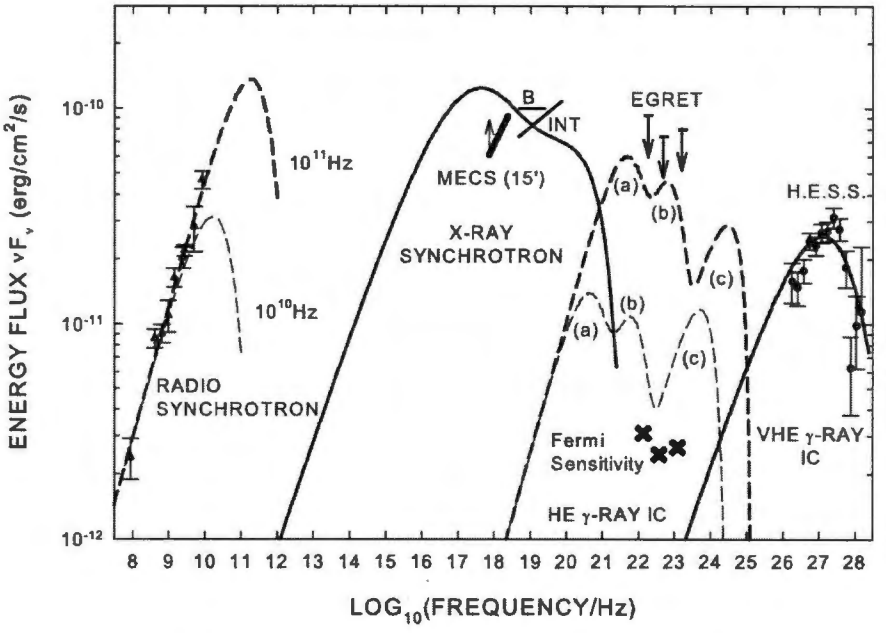

Figure 2.13: Dashed lines represent the radio SR and HE IC γ-rays of the total $2^\circ \times 3^\circ$ Vela X structure corresponding to the cutoffs of 10^{10} Hz (thick dashed line) and 10^{11} Hz (thin dashed line). Also, the features due to scattering on (a) the CMBR, (b) FIR, and (c) starlight are visible. The X-ray synchrotron and VHE γ-ray IC spectra include the pulsar spin effect of evolution. Triangles represent the radio flux measurement from Alvarez et al. (2001), circles represent H.E.S.S. data from Aharonian et al. (2006a), the short thick solid lines represent *INTEGRAL* data. The *BeppoSAX* "MECS" observation is shown as a lower limit for an extraction radius of 15′, and the PDS ("B") measurement is from Mangano et al. (2005). Arrows represent *EGRET* Vela X upper limits from De Jager et al. (1996a), crosses represent the *Fermi*-LAT 1 year sensitivity. From De Jager et al. (2008) .

which is not readily explained in any model in which the TeV size is limited by cooling. They proposed a scenario which may address these questions, postulating that the HE particles diffused out of the ERN, while the cocoon is a relatively recent feature of the PWN. They suggested that the maximum energy of particles in the cocoon spectrum is probably determined by cooling in a high B-field (100 μG) close to the pulsar, before they are injected into the low-B field cocoon. Also the ERN probably contains particles injected over the full lifetime of the system (this is not the case for the cocoon). Bulk escape of particles from ERN is required to explain the steep *Fermi* spectrum. This may happen when the reverse shock interacts with the PWN and halts effective electron confinement in the ERN. The inferred diffusion coefficient required to explain the absence of > 100 GeV particles is of order 1 000 times lower than that inferred for CRs in the ISM, but much faster than Bohm diffusion for the assumed magnetic field in the ERN. In the Hinton et al. (2011) model, diffusive transport is switched on at time $\sim 70\%T$, with T the age when the reverse shock from the SNR is believed to start interacting with ERN, and with particles initially uniformly distributed in a spherical PWN, after which time particles injected at the termination shock are assumed to be confined within the cocoon. They assumed diffusion to be a factor $\delta = 2\ 000$ faster than Bohm diffusion, with the magnetic field in the nebula falling continuously as $t^{-0.5}$.

2.4 Conclusions

In this chapter we first gave a summary of the identification controversy surrounding Vela X. Next, we discussed the multiwavelength properties of the Vela PWN, as well as the broadband modelling of this plerion.

2.4.1 Identification Controversy

Rishbeth (1958) observed three strong nonthermal radio sources of enhanced brightness temperature, and designated them Vela X, Vela Y, and Vela Z. To determine the nature of these sources many authors have tried to find their spectral indices (Milne, 1968a, 1980; Weiler & Panagia, 1980; Milne & Manchester, 1986; Dwarakanath, 1991). A controversy among Milne (1968a); Milne & Manchester (1986); Milne (1995) and Weiler & Panagia (1980) erupted. The first group claimed that there was no significant difference between the indices of Vela X and that of Vela YZ, and concluded that Vela X was associated with the Vela SNR. Conversely, Weiler & Panagia (1980) maintained that Vela YZ exhibited a steeper index compared with that of Vela X, and concluded that Vela YZ is part of the shell SNR, while Vela X is a plerion. Dwarakanath (1991) attempted to solve this mystery by re-measuring the spectral indices and estimating the free-free absorption at 85 MHz. He confirmed the plerion classification. Frail et al. (1997) found that Vela X consisted of a network of fine, overlapping, linear, synchrotron-emitting filaments ubiquitous in other plerions. Bietenholz et al. (1991) clinched the plerion identification by showing that there are significant morphological differences between the nebula and the shell filaments. Alvarez et al. (2001) obtained spectral indices for Vela X, Vela Y, and Vela Z which were consistent with a spherical SNR containing a central plerion. The radio observations by Dodson et al. (2003b) of a highly-polarized radio nebula (implying a wound-up toroidal magnetic field) which is symmetrical with respect to the projected pulsar axis, as well as two surrounding lobes furthermore argue strongly for a plerion identification of Vela X.

2.4.2 Multiwavelength Properties of the Vela PWN

Bietenholz et al. (1991) discovered a localized, elongated ridge of highly polarized radio emission in a direction northeast of the Vela pulsar position. This feature is probably part of the shock produced by the termination of the relativistic MHD pulsar wind into the ambient medium. Frail et al. (1997) found a very bright radio filament nearly coinciding with the X-ray cocoon. Lewis et al. (2002) found two radio lobes oriented about the spin axis of the pulsar, in agreement with models where the emission is driven by particles from magnetic poles. They also found that the northern lobe exhibited a bright edge, while the southern lobe was more diffuse. Dodson et al. (2003b) also found radio emission from two lobes around the pulsar, differing in size and brightness, with the radio emission starting where the X-ray emission stops. Hales et al. (2004) found that the orientation of the 31 GHz PWN is in agreement with that of the radio lobes observed at higher resolution but at lower frequencies. They also found a filament southeast of the PWN, ending in an anchor-like feature, which is situated in the direction of the proper motion and spin axis of the pulsar.

Ögelman et al. (1989) claimed a marginal detection of an optical counterpart to the compact Vela X-ray nebula. Mignani et al. (2003), however, found much deeper upper limits of 28.1 HST mag arcsec^{-2} for the inner nebula, and 28.0 – 28.5 HST mag arcsec^{-2} for the outer

nebula, while Sefako (2002) obtained an optical plerionic excess for Vela and also observed an Hα feature at the bow shock of Vela, as well as an apparent excess around the pulsar position in R band. Danilenko et al. (2011) resolved an IR knot-like source northwest of the pulsar, and a faint counterjet extended by a few arcseconds southeast of the pulsar, features which may associated with the PWN. They also likely saw an interface between the pulsar wind and the SNR ejecta supported by a pressure balance between these two members of the remnant.

Kellogg et al. (1973) detected the X-ray source 2U 0832−45 above 9σ, being less than 1°.2 in extent. Various authors found spectral indices ranging from $\Gamma = 1.7$ to $\Gamma = 2.17$ for different regions of the Vela X plerion (See Table 2.4). Ögelman & Zimmermann (1989) found a compact nebula with extension $\sim 1'$ and also found an emission region extending from the pulsar in the south western direction out to $\geq 3'$. Willmore et al. (1992) detected an elongated region of diffuse hard X-rays around the Vela pulsar and argued that this 1° extended emission was a synchrotron nebula. Markwardt & Ögelman (1995) found an X-ray emitting "jet" (cocoon) begining at the pulsar, with a size of $45' \times 12'$, extending towards the south-southwest. Markwardt & Ögelman (1997) found that the cocoon's X-ray spectrum was similar to that of the surrounding Vela SNR. Comparison of two noncontemporaneous *Chandra* observations by Pavlov et al. (2001) of some of the Vela PWN features revealed displacement of the arcs and southwest knot, brightnening of the southeast jet, dimming of the northeast knot, and brightening dimming of the diffuse emission towards the northeast and southeast, and also provided evidence for hardness ratio changes in the southeast jet. Helfand et al. (2001) found a well-resolved synchrotron nebula with a toroidal morphology similar to the one observed in the Crab nebula, as well as an axial, Crab-like jet (the outer part which Pavlov et al. (2003) later observed to be highly variable). They also found evidence for a counterjet with a position angle of 130° measured east of north, and aligned to within $8° \pm 5°$ with the proper motion vector. Using *Chandra*, Helfand et al. (2001) also found two arcs and diffuse emission in a "kidney-bean shape". LaMassa et al. (2008) found a two-component X-ray spectrum consisting of a thermal and a nonthermal component. The spectrum was steepening with distance from the pulsar, rather than softening, which may be caused by the crushing of the cocoon against the PWN, leading to adiabatic heating that may harden the spectrum. Mattana et al. (2011) lastly reported the discovery of extended emission beyond the inner PWN by *INTEGRAL*, with the northern side (where emission may be due to freshly injected particles following the passage of the reverse shock) appearing larger and more significant than the southern one which partially overlaps the cocoon.

Following the upper limits on the unpulsed flux from the Vela PWN produced by *COS-B* (Grenier et al., 1988) and *EGRET* (Kanbach et al., 1994), De Jager et al. (1996a,b); Strickman et al. (1996) obtained an unpulsed power-law spectrum with a photon index of $\Gamma = 1.6 \pm 0.5$ in the energy range between 0.061 MeV and 0.4 MeV. These results were consistent with an extrapolation of the $\sim E^{-1.7}$ spectrum of the $1'$ compact nebula (in the optical to 25 keV range). Strickman et al. (1996) concluded that the total Vela spectrum (corresponding to the extended nebula) had a spectral index of ~ 2.2 below ~ 20 keV, which steepened significantly above ~ 20 keV, having a spectral index of $\Gamma = 2.7$, and which then hardened above ~ 60 keV to meet the spectrum of index $\Gamma = 1.8$ as measured by *OSSE* (corresponding to the $1'$ compact nebula). Enomoto et al. (2006) obtained an upper limit on the flux from the putative source offset by 0°.13 from the pulsar position which was a factor of 5 less than the flux reported earlier by Yoshikoshi et al. (1997). They did however observe extended VHE emission from a position 0°.5 south of the pulsar at the 4σ level. Aharonian et al. (2006a) observed the Vela X region to the south of the Vela pulsar, and fitted a

spectrum between 550 GeV and 65 TeV with a photon index of $\Gamma = 1.45 \pm 0.09_{stat} \pm 0.2_{sys}$ and an exponential cutoff at an energy of $13.8 \pm 2.3_{stat} \pm 4.1_{sys}$ TeV for an integration region of 0°.8. They also obtained an integral flux above 1 TeV of $(1.28 \pm 0.17_{stat} \pm 0.38_{sys}) \times 10^{-11}$ cm^{-2} s^{-1} for this VHE source which coincided with the hard X-ray source seen by *ASCA* and *ROSAT*. The best-fit intrinsic width of the VHE source was $0°.48 \times 0°.36$ (i.e., 58×43 arcmin^2 vs. the X-ray size of 45×12 arcmin^2; Markwardt & Ögelman, 1995). Yoshikoshi et al. (2009) detected Vela X at 4.5σ after reanalysis of CANGAROO-I data. Re-observation of Vela X by H.E.S.S. revealed γ-ray emission up to a radius of 1°.2, with the spectrum of the outer annulus being consistent with that found by Aharonian et al. (2006a) for the central source ($r < 0°.8$). Using *AGILE*, Pellizzoni et al. (2010) defined the off-pulse window for the Vela pulsar to be 0.65 to 1.05 in normalized phase, and detected the source AGL J0834−4539 in this window at $\sim 5.9\sigma$ significance with a flux of $(3.5 \pm 0.7) \times 10^{-7}$ cm^{-2} s^{-1} above 100 MeV, located $\sim 0.5°$ southwest of the pulsar, and having an extent of $1°.5 \times 1°$. Abdo et al. (2010) detected γ-ray emission at the 14σ level from a $2° \times 3°$ area south of the Vela pulsar using *Fermi* LAT. They found a best-fit source radius of $0°.88 \pm 0°.12$ for a uniform disc morphology, and a spectrum which was well-described by a power law $\Gamma = 2.41 \pm 0.09 \pm 0.15$, giving an integral flux above 100 MeV of $(4.73 \pm 0.63 \pm 1.32) \times 10^{-7}$ cm^{-2} s^{-1}. Abramowski et al. (2012) re-observed Vela X with H.E.S.S. above 0.75 TeV, obtaining a source extent of 1°.2 in radius. The spectra of the inner and outer regions showed no significant variations. The VHE morphology now seems to be intemediate between the X-ray cocoon and radio morphologies and this may possibly be explained by two distinct electron populations, one being responsible for the radio and part of the VHE emission, and the other giving rise to the X-ray as well as contributing toward the VHE emission.

2.4.3 Modelling

De Jager et al. (1996a) constrained the Vela PWN magnetic field using *OSSE* data and found an average B-field of $30 - 100$ μG. They also found $W_{\rm particle} \sim 0.5 W_{\rm pulsar}$, where $W_{\rm particle}$ is the total energy of the particles, and $W_{\rm pulsar}$ is the total energy of the pulsar. Blondin et al. (2001) modelled the evolution of a PWN inside an SNR. They found that the crushing and reexpansion phases of the PWN are subject to Rayleigh-Taylor instabilities and that an inhomogeneous ambient medium may result in PWNe that are offset from the pulsar position. They applied this scenario to Vela X. By modelling the Vela synchrotron compact nebula, Sefako & De Jager (2003) inferred the pair multiplicity M (number of secondary pairs spawned by a single accelerating primary) to be between $300 < M < 700$, and constrained the wind magnetization parameter to $0.05 < \sigma < 0.5$. Mangano et al. (2005) found a larger X-ray luminosity, implying a higher value of M. Helfand et al. (2001) applied the MHD model of Kennel & Coroniti (1984a), originally developed for the Crab to Vela X (allowing $\sigma \sim 1$) and found that this model provides a reasonable explanation for the toroidal arcs and nebula but not for the jet and counterjet. Bednarek & Bartosik (2003) constructed a time-dependent radiation model for PWNe in SNRs where heavy nuclei excite waves just beyond the pulsar wind shock and resonantly transfer this energy to positrons. They calculate SR, IC, and bremsstrahlung radiation spectra originating from the leptons, in addition to a hadronic component invoking π^0 decay. They found that the HE γ-ray emission is mainly due to leptons in the SNR, while the hadronic contribution is significantly lower in their model (contributing only in the VHE band). Horns et al. (2006) applied a hydronic model (with the hadrons having a nearly mono-energetic distribution) to the VHE component of Vela X, requiring $\sim 10^{49}$ erg in proton energy and

a plasma density of 0.6 cm^{-3}. They furthermore found that the secondary electrons resulting from the inelastic (proton-proton) interactions may produce SR in the optical to X-ray band. De Jager (2007) criticized this hadronic scenario in terms of the required B-field, ion budget, and lepton conversion efficiency. He furthermore constrained the pair multiplicity to be $0.5 < M < 5 \times 10^5$, and lastly argued for two electron populations being responsible for the radio SR and γ-ray IC emission. LaMassa et al. (2008) applied a leptonic model and fitted the broadband spectrum by invoking SR and IC resulting from a three-component broken power-law injection spectrum. They inferred an intrinsic break at $\sim 5 \times 10^6$ keV and a cooling break at 5.5×10^{10} keV. De Jager et al. (2008) implemented a time-dependent two-component leptonic model and was able to accurately model the radio, X-ray and VHE data, also predicting a spectral component in the *Fermi* range (note, however, that this model needs to be revisited in view of the larger TeV extent of Vela X as revealed by new H.E.S.S. results – Abramowski et al. 2012). Similarly, Qiao et al. (2009b) modelled radio to X-ray data using SR and VHE data using IC scattering. Zhang & Yang (2009) modelled the SED of Vela X using both a leptonic and hadronic-leptonic model. Their single-component leptonic model fit either the X-ray or TeV spectral components (for different model parameters), but not both, while their hadronic-leptonic model could reproduce the total SED. Hinton et al. (2011) modeled the X-ray cocoon and the extended radio nebula (ERN) by invoking continous injection of particles with a fixed spectral shape and conversion efficiency. They proposed enhanced diffusive escape of accumulated HE particles from the ERN after interaction with the reverse shock to explain the steep *Fermi* LAT spectrum, and also that the cocoon is a relatively young structure. They lastly suggested that freshly-injected particles lose the bulk of their energy in the high B-field close to the pulsar, before being confined within the cocoon. They also noted that the energy-dependent escape of particles from Vela X should produce a distinct feature in the local CR electron spectrum in the VHE band.

In the following chapter we are going to discuss the multiwavelength properties of the Vela SNR and pulsar, as well as the proper motion of the latter.

Chapter 3

Multiwavelength Properties of the Vela System

The Vela SNR is one of the nearest Galactic objects to Earth, lying at a disatance of only 290 pc. It has a large angular diameter of $\sim 8^{\circ}$ seen in several wavebands, and many filaments and nebulosities are also visible. In this chapter we will give an overview of observational results regarding this SNR. The Vela pulsar represents a source of energy to the adjacent PWN. We will briefly discuss its spectral and light curve properties, proper motion and parallax, as well as its glitching behaviour. This chapter therefore describes more pieces of the puzzle of the very complex Vela source, including the plerion, SNR, and pulsar.

3.1 The Vela SNR

3.1.1 Radio

Following earlier radio studies, Dwarakanath (1991) perfomed low-frequency observations of the Vela SNR. Using these data along with ealier observations at higher frequencies, he found a relatively steeper spectrum for Vela X compared to that of Vela YZ. Dwarakanath (1991) therefore concluded that the Vela SNR had a filled-centre morphology (see Section 2.1 for details).

Dubner et al. (1992) used the 30 m IAR radio telescope to map the HI region in the direction of the Gum nebula. They inferred that the Vela SNR was interacting along its northwestern border with a corner of the observed HI shell, which is ten times denser than its environment. They noted that this intersection may be responsible for the bright UV and optical arches and filaments observed on the northwestern side of the remnant (see Section 3.1.2), and also for the off-centre position of the Vela pulsar (however, see paragraph on the work of Dubner et al. 1998 below). Dubner et al. (1992) also noted that the Vela pulsar was found within an HI cavity. They concluded that the Vela SNR is located at a distance between 500 pc and 800 pc, expanding inside a cavity created 2.6×10^6 years ago. In this scenario, it is the SNR envelope expansion that was asymmetrical, rather than the pulsar motion (see Section 3.2.2).

Duncan et al. (1996) surveyed part of the southern Galactic Plane at 2.4 GHz and found that the total-power and the linear polarization emission of the region surrounding the Vela remnant were consistent with the radio observations of the brighter sections of this SNR by Milne (1968a, 1980). The total-power image of Vela exhibited many filaments and loop-like structures. At the northern side of the SNR, they found a pair of bright concentric arcs, defining the northern edge of

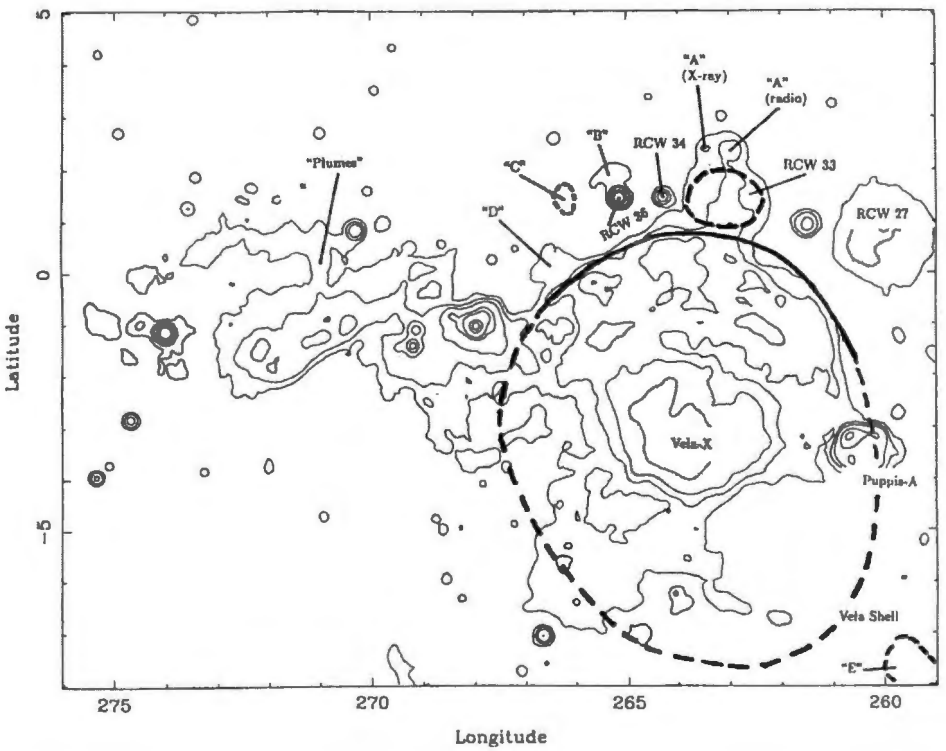

Figure 3.1: A contour plot and sketch of the total-power 2.4 GHz emission surrounding the Vela SNR, highlighting prominent features. Axes markings are in degrees. From Duncan et al. (1996).

the shell. This region appeared to be much brighter than the southern region, with the boundary between the high and low surface brightness regions occurring at the southern edge of Vela X. On the southern edge, the emission faded smoothly into the background, making it difficult to identify the southern remnant boundary unambiguously (see Figure 3.1). Duncan et al. (1996) proposed that the interaction of the Vela remnant with the ambient northern region of increased density (as indicated by CO observations by Dame et al., 1987) is responsible for enhanced shell emission to the north, as well as for the asymmetrical SNR shape (an $8°.6 \times 7°.4$ ellipse, with the centre being offset by $40'$ from the pulsar position). The low-intensity polarized emission extended towards the edge of the SNR, with particularly intense emission from Vela X. Duncan et al. (1996) also argued that the observed polarization position angles are the result of directional variation of the intrinsic magnetic field, rather than Faraday rotation. They lastly observed a remarkable similarity between this radio image and the X-ray image abtained by *ROSAT* (Aschenbach et al., 1995), both on small and large scales.

Using the VLA, Frail et al. (1997) resolved many fine overlapping filaments in the Vela X region. They also found a bright filament tracing the eastern boundary of the X-ray cocoon first detected by Markwardt & Ögelman (1995).

Bock et al. (1998) conducted a high-resolution radio continuum survey at 843 MHz of the Vela SNR using MOST, allowing them to identify this SNR as a member of the composite class. The radio plerion consisted of both diffuse and filamentary emission, while the SNR showed concentric shell filaments having $H\alpha$ and X-ray counterparts.

As noted in Chapter 2, Alvarez et al. (2001) calculated integrated flux densities for the Vela

SNR region for the range 30 to 8 400 MHz using archival data. They succeeded in separating the spectra of Vela X, Vela Y, and Vela Z. Their map of brightness temperature spectral index showed a circular structure with a flat spectrum near Vela X, steepening towards the outer edge (Vela Y and Vela Z). This reinforces the plerionic nature which is distinct from the surrounding SNR.

Dubner et al. (1998) studied the distribution and kinematics of the neutral hydrogen in the direction of the Vela SNR using the Parkes 64 m radio telescope. They observed a thin, roughly circular shell of radius ~22 pc that delineates the outer border of the thermal X-ray emission detected by Aschenbach et al. (1995). They concluded that the low systemic velocity suggested a source distance of less than 500 pc (see Section 3.2.2), and inferred that the HI shell expands into an ambient medium of density $\sim 1 - 2$ cm^{-3}. Dubner et al. (1998) furthermore compared HI and Hα emission from the Vela SNR direction, and found that the HI shell probably contains embedded dust that might be responsible for increased optical absorption in this region. The brightest arc-shaped optical filaments associated with the western side of the SNR, however, showed good association with the HI features. Dubner et al. (1998) lastly suggested that the surrounding medium has not significantly affected the remnant's morphology or dynamics, based on the fact that the SNR has a well-defined spherical shape at different wavelengths (contrary to the suggestions of other authors; Section 2.1).

Dodson et al. (2003b) discovered that the radio nebula surrounding the Vela pulsar was more extended (in the GHz range) than previously thought (e.g., Bock et al. 1998). This nebula exhibited a symmetrical morphology with respect to the pulsar, consisting of a northern and southern lobe. They observed a highly polarized structure, with the polarization vectors revealing a symmetry with respect to the spin axis of the pulsar. They lastly noted that there is an absence of radio emission at the centre where the *Chandra* inner torus was found.

3.1.2 Optical, UV, and IR

Milne (1968b) observed faint optical background emission from the Vela X region which is embedded within the Vela SNR, with many bright, sharp filaments located at the northern and western boundaries, and more diffuse nebulosities on the eastern side.

Miller (1973) obtained photographs of the Vela SNR in ultraviolet (UV) light, and observed a complete circular outline for the first time. He found that the centre of the X-ray shell coincided well with the optical centre of the SNR, and that the position of the Vela pulsar PSR lay approximately 1°.5 to the west of this centre. Miller (1973) also observed scallop-like arches and filaments forming the western and northwestern rim. Interestingly, an unusual feature was found near the eastern rim of the SNR: a feather-like structure with thin wisps of material trailing off towards the west. Lastly, he noted that the filamentary structure of the SNR was more prominent in UV than in red light.

Van den Bergh et al. (1973) presented photographs of known optical SNRs and inferred that the region covered by the Vela SNR filaments had a diameter of 270′, and that the centre was close to the pulsar position. This led Van den Bergh et al. (1973) to speculate that this pulsar was the stellar remnant of the supernova that produced the Vela filaments. They lastly noted that optical filaments occurred more densely near Vela X, and that this filaments did not appear to correspond to the observed radio hot spots.

Elliott et al. (1976) considered Vela XYZ to be the radio manifestation of a single SNR with a 6° diameter. They found filamentary nebulosities in Hα, with some of these filaments being

perpendicular to the circumference of a 6°-diameter circle. They also found a diffuse nebulosity which was at its brightest in the Vela X and pulsar vicinity. Vela XYZ therefore exhibited the filamentary structure typical of many optically identified SNRs, with this structure outlining a shell which covers the area of the radio emission (see Weiler & Panagia, 1980).

Using very-high-resolution spectroscopy of optical lines, Shull (1983) argued that the velocity dispersion of knots in the filaments associated with the Vela SNR resulted mainly from turbulence, rather than from thermal effects within the emitting region. He found that the line-of-sight velocity dispersions for the observed knots were about $20 - 30$ km s^{-1}. This included a thermal velocity dispersion of about 16 km s^{-1} for hydrogen, and 4 km s^{-1} for nitrogen. The knots were also observed to move randomly relative to each other, with speeds of up to 30 km s^{-1}.

Sankrit et al. (2001) reported on the results of a Far Ultraviolet Spectroscopic Explorer (*FUSE*) observation of an X-ray knot in the Vela SNR. They detected two kinematic components, one of which had a central velocity of -50 km s^{-1}, and a shock velocity of about 180 km s^{-1} while the other had a central velocity of about $+100$ km s^{-1} and a shock velocity of 140 km s^{-1}. They identified the former component with the X-ray knot, and suggested that the presence of reverse shocks created these localized regions of high pressure within the remnant.

Nishikida et al. (2006) detected the Vela SNR using the *Spectroscopy of Plasma Evolution from Astrophysical Radiation* (*SPEAR*) instrument, also known as *FIMS*. The *SPEAR* map indicated Far Ultraviolet (FUV) emission over most of the Vela SNR extending to $\sim 8°$. The FUV and X-ray features were not correlated, but their extent was the same. Nishikida et al. (2006) noted that the SNR's global FUV spectra were dominated by shock-induced emission lines, and that the overall radiation rate was dominated by shocks in higher density regions traced by the FUV emission.

3.1.3 X-rays

Seward et al. (1971) used a Terrier-Sandhawk rocket to conduct scans in two directions through the Vela region. From the first scan, they obtained diffuse emission below 2 keV coming from a region of $\sim 5°$. The second scan required a point source close to the pulsar position, in addition to a shell source.

Gorenstein et al. (1974) observed soft X-rays from the Vela SNR and studied its spectrum and structure in the 0.1 keV to 1.5 keV range. They found that the spectral data below 1.5 keV were consistent with thermal radiation from a hot plasma (with a temperature of $\sim 10^6$ K), and inconsistent with a simple power-law function. They noted that the X-ray structure of the Vela SNR was a fragmentary shell resembling the UV filaments, and also that the Vela pulsar was outside the region of soft X-ray emission. X-ray absorption measurements along the line of sight as well as shock-wave model interpretations implied an average density of interstellar material of about 0.1 cm^{-3} between the Sun and the Vela SNR.

Moore & Garmire (1975) observed the Vela SNR using an Aerobee 170 sounding rocket. They found that the 0.15 keV to 1.0 keV emission exhibited two principal regions of enhancement (with an extent of ~ 4 deg^2) and a general limb brightening which possibly implied a shell-like source structure. The first region which lay north of Vela X and slightly southwest of Vela Y had an intensity of $(2.1 \pm 0.3) \times 10^{-9}$ ergs cm^{-2} s^{-1}, and the second region which lay east of both Vela X and Vela Z had an intensity of $(1.6 \pm 0.2) \times 10^{-9}$ ergs cm^{-2} s^{-1}. They found that the gross features were consistent with the structure determined by Seward et al. (1971), although they found more fine-scale structure.

Kahn et al. (1983) presented the 0.15 keV to 2.0 keV spectrum of the Vela SNR using the low-energy detectors (LEDs) of the A−2 experiment, flown on *HEAO 1*. They found no evidence for abundance anomalies of oxygen or iron in the Vela remnant spectrum. They observed a discrete spectral feature in the spectrum at ∼0.6 keV which was identified with O VII and O VIII emission. This was the first unambiguous detection of oxygen X-ray line emission from the Vela remnant, and confirmed the view that the soft X-ray emission from the source arises from hot gas at $\sim 10^6$ K.

Kahn et al. (1985) generated spatially-resolved X-ray maps of the Vela SNR using the Imaging Proportional Counter (IPC) of the *Einstein Observatory* in the 0.2 keV to 1.0 keV and 0.8 keV to 2.0 keV spectral bands. They found that the maps exhibit a highly asymmetrical and inhomogeneous structure, and their spectral analysis showed that the emission from the remnant could be consistently described as thermal radiation from hot gas which is nonuniform in density and temperature, but in approximate pressure equilibrium. The softest and brightest X-rays were associated with bright optical [O III] filaments, but not perfectly.

Willmore et al. (1992) detected hard X-ray emission (2.5 − 25 keV) from a number of bright knots in the Vela SNR shell which was associated with the bright features in the lower-energy *Einstein Observatory* and Hα images. The features at different wavelengths were not coincident, suggesting the presence of blobs of material at a wide range of temperature.

Aschenbach et al. (1995) scanned the Vela SNR region using the *ROSAT* X-ray telescope in the 0.1 keV to 2.4 keV range. Their results revealed a faint X-ray shell, well described by a circle of $\sim 8^\circ.3$ diameter, showing that the pulsar was $\sim 25'$ from the centre of the SNR. This implied that the pulsar plausibly resulted from the same explosion. They also observed six extended X-ray features located outside the blast-wave front having conal shapes, which apparently originated close to the pulsar. They proposed that the these features were the result of fragments coasting through the surrounding medium, the first being created by instabilities during the stellar collapse, and subsequently expelled by the explosion of the progenitor star. Aschenbach et al. (1995) observed that the symmetry axes of these structures intersected each other close to the remnant geometric centre, favouring their common origin. They suggested that the X-ray emission was associated with these protruding objects, being produced by shock heating of the ambient medium by the supersonic motion of the objects. The angular offset of the objects' origin divided by their proper motion velocity of 0.049 arcsec yr^{-1} implies an SNR age of $\tau = 18 \pm 9$ kyr and distance of $d = (400 \pm 200)$ pc.

3.2 The Vela Pulsar (PSR J0833−4510)

The Vela SNR is the nearest one ($d = 290$ pc) to contain a young active pulsar – the Vela pulsar. This pulsar is a famous rotation-powered neutron star (NS). It has been identified in different spectral domains ranging from radio to hard γ-rays, and represents the brightest persistent source in the GeV sky. In soft X-rays, its emission is dominated by thermal blackbody radiation believed to have originated from the cooling surfaces of the NS's hot polar caps (Danilenko et al., 2011). Conversely, the radio, optical, and γ-ray emission is nonthermal, generated by relativistic particles that are accelerated in the magnetosphere of the rapidly-rotating and strongly-magnetized NS. The Vela pulsar's period of $P = 89$ ms and period derivative of $\dot{P} = 1.25 \times 10^{-13}$ s s^{-1} imply a characteristic age of $\sim$ 11 000 yrs and a spin-down luminosity of $\dot{E} = 7 \times 10^{36}$ erg s^{-1} (LaMassa et al., 2008).

3.2.1 Multiwavelength Properties – a Chronological Overview

While searching for southern pulsars using the Molonglo Radio Observatory, Large et al. (1968) discovered the short-period Vela pulsar in the vicinity of the Vela SNR. Radhakrishnan et al. (1969) observed the Vela pulsar between 1 720 MHz and 2 700 MHz using the Parkes 210 foot reflector. They found that the pulsar had narrow pulse width, high and constant intensity, and a very high degree of linear polarization.

Harnden & Gorenstein (1973) observed the X-ray structure of the Vela SNR between 0.1 keV to 1.5 keV. They found an extended region and a concentrated one which was consistent with a point source at the position of PSR J0833−4510. Albats et al. (1974) observed pulsed emission from PSR J0833−4510 in the 10 MeV to 30 MeV energy range. Culhane et al. (1974) presented observations of the Vela pulsar in the energy range 0.7 keV to 1.5 keV using the MSSL X-ray telescopes on board the *Copernicus* satellite. They found that their spectrum was consistent with the one obtained by Kellogg et al. (1973) for the source 3U 0833−45, and suggested that there should be a low-energy turnover in the spectrum.

Thompson et al. (1975) detected pulsed γ-ray emission at the radio period from the Vela pulsar, as well as an unpulsed flux from the Vela region using the *Second Small Astronomy Satellite* (*SAS−2*). The pulsed emission consisted of two peaks lagging the single radio peak by about 13 ms and 48 ms, respectively. They found that the luminosity of the pulsed emission above 100 MeV from Vela was about 0.1% of that from the Crab pulsar. On the other hand the pulsed emission from Vela at optical wavelengths was less than 2×10^{-4} of that from the Crab.

Wallace et al. (1977) detected optical emission from the Vela pulsar using the $f/15$ focus of the 3.9 m Anglo-Australian Telescope (AAT). They found that the Vela pulsar emission in different wavelength regimes occurred at different phases, and that the optical pulses were symmetrical between the γ-ray pulses. They estimated the time-averaged pulsed emission brightness in the blue filter to be 25.2 magnitude. Kanbach et al. (1980) observed HE γ-ray emission from the Vela pulsar using *COS-B*. They obtained a spectrum described by a power law with a spectral index of 1.89 ± 0.06 in the energy range 50 MeV and 3 GeV, with signs of a spectral flattening at low energy and steepening above a few hundred MeV. Harnden et al. (1985) used the imaging detectors of the *Einstein* X-ray observatory (0.1 keV to 4.5 keV) and found a pointlike object coinciding with the pulsar (however, no pulsations; see also Pravdo et al., 1978), possibly due to blackbody emission, implying a $\sim 10^6$ K surface temperature.

Ögelman & Zimmermann (1989) observed the vicinity of the Vela pulsar in the range 0.03 keV to 2.4 keV using the imaging *EXOSAT* telescope. Their results indicated that the central source was softer than surrounding regions, and its spectrum was fitted by a blackbody, implying surface temperatures in the range $(0.6 - 1.0) \times 10^6$ K. Ulmer et al. (1991) used the *High Energy Astrophysics Observatory* (*HEAO 3*) γ-ray spectrometer, and reported 2σ upper limits to γ-ray pulsations from PSR J0833−4510 in the energy range 3.2 MeV to 10 MeV. Using the Birmingham coded mask telescope, Willmore et al. (1992) inferred a spectral index of 1.55 ± 0.06 for the pulsar (2.5 − 25 keV), which was consistent with the value of 1.7 ± 0.2 obtained by Harnden et al. (1985) in the 0.1 keV to 4.5 keV range.

Kanbach et al. (1994) detected the Vela pulsar using *EGRET*, and an average flux of $(7.8 \times 1.0) \times 10^{-6}$ photons cm^{-2} s^{-1} was found in the range 100 MeV to 2 GeV. They obtained a power-law spectrum with index $\Gamma = 1.70 \pm 0.02$ between 30 MeV to 2 GeV, and the extrapolation of this spectrum to the 3 MeV to 30 MeV range agreed well with the observations by *COMPTEL*.

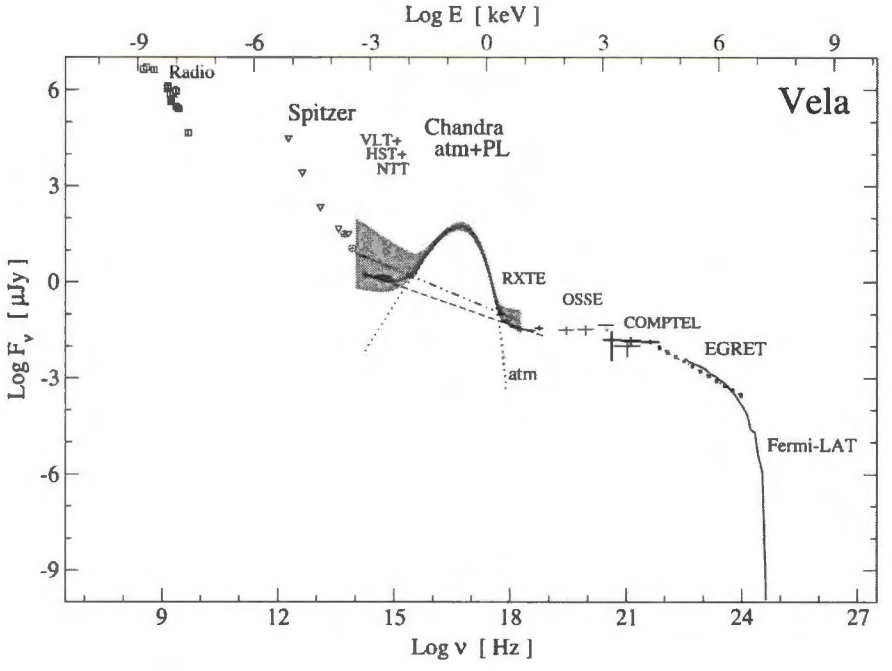

Figure 3.2: Multiwavelength unabsorbed spectrum for the Vela pulsar from the radio to hard γ-rays compiled from data obtained with different instruments, as shown in the plots. The red circles represent Mid-IR. Downward-pointing triangles represent *Spitzer* upper limits. From Danilenko et al. (2011). The *Fermi* spectrum is lower than the *EGRET* one at HE energies (Abdo et al., 2009).

Yoshikoshi et al. (1997) derived a 95% confidence flux upper limit to the pulsed emission from the pulsar of $(3.7 \pm 0.7) \times 10^{-13}$ photons cm^{-2} s^{-1} above 2.5 ± 1.0 TeV.

Strickman et al. (1999) observed the Vela pulsar using *RXTE*. They detected pulsed emission in the range 2 keV to 30 keV, as a well as a pulse profile which showed two peaks that are roughly in phase with the *EGRET* peaks, without any significant interpeak emission above 30 MeV. The phase of the second peak was energy-dependent, moving to a higher phase with increasing energy in the *RXTE* band. They found that the average pulsed spectrum joined smoothly to the HE spectrum of *OSSE*, *COMPTEL* and *EGRET*, which provided strong evidence for a thermal rather than a nonthermal origin for the *ROSAT* data (see Figure 3.2).

Pavlov et al. (2001) reported the spectral analysis of two observations of the Vela pulsar using the *Chandra X-ray Observatory*. They found that the pulsar spectrum did not show statistically significant lines (0.2 keV to 8.0 keV). They obtained a power-law spectral index for the soft component of $\Gamma = 1.5 \pm 0.3$, and for harder component $\Gamma = 2.7 \pm 0.4$. They also noted that the extrapolation of the power-law component of the first fit towards lower energies matched the optical flux.

Harding et al. (2002) reported on observations of the Vela pulsar using *RXTE* between the energy 2 keV and 30 keV, and identified two separate hard and soft nonthermal emission components: (1) a harder spectrum which connected smoothly with the *OSSE*, *COMPTEL*, and *EGRET* spectra; (2) a softer component which was consistent with an extrapolation to the pulsed optical flux. They found five peaks in the light curve, with no variation in pulse width in the 2 keV to 30 keV band. Harding et al. (2002) also noted that the *RXTE* soft component suggested continuous emission from optical to hard X-rays, which was an important feature to be explained by a pulsar

model of Vela.

Shibanov et al. (2003) were the first to detect the Vela pulsar in the near-IR using the *VLT / ISAAC*. Their results confirmed the nonthermal origin of the pulsar emission in the IR to optical range (with the index in the optical range being -0.12 ± 0.05). They also found that the IR to optical spectrum and the phase-averaged power-law spectral component detected in the HE tail of the pulsar X-ray emission could not be fitted with a single power law. They suggested either a spectral break in the near ultraviolet to extreme ultraviolet (NUV-EUV) range, or the presence of an additional spectral component with a flatter spectrum dominating in the optical range. If the latter is true, the IR and the X-ray spectrum can be fitted with a single power law, implying the same origin of the nonthermal pulsar emission in the second pulse of the pulsar light curve in both the IR and X-ray range.

Mori et al. (2004b) observed the Vela pulsar using *XMM-Newton*, and analysed thermal emission from the pulsar which dominates below ~ 1 keV. The thermal spectrum was featureless, and the EPIC-PN spectrum was fitted by a magnetized hydrogen atmosphere model with $B = 10^{12}$ G, suggesting the presence of a hydrogen atmosphere, as indicated by *Chandra*. They found a temperature of $T^{\infty} \simeq (6.4 - 7.1) \times 10^5$ K at an age of $\sim 10^4$ yr, which is below the standard cooling curve.

Romani et al. (2005) observed the Vela pulsar using the *HST, STIS* and *MAMA-UV* detectors. They obtained an NUV light curve and crude FUV phase-resolved spectrum. The pulse was dominated by complex nonthermal emission throughout the pulse period. Romani et al. (2005) observed four distinct pulse peaks in the NUV band; peaks 3 and 4 were also observable in the optical. They also found that a power-law was a poor fit to the phase-averaged spectrum, with a substantial excess in the shortest wavelength bins. They found an upper limit on the Rayleigh-Jeans component at UV pulse minimum, which suggested a low mean surface temperature of $T_{\rm eff}^{\infty} \lesssim 4.6 \times 10^5$ K.

Aharonian et al. (2006a) found a 99.9% upper limit of 7.6×10^{-13} cm^{-2} s^{-1} for the integral flux above 1 TeV for an assumed point source at the position of the pulsar.

Manzali et al. (2007) studied the phase-resolved spectrum of the Vela pulsar using *XMM-Newton*. The phase-integrated spectrum of Vela was well described by a three-component model, consisting of two blackbodies ($T_{\rm bb} = 1.06 \pm 0.03 \times 10^6$ K, $R_{\rm bb} = 5.1^{+0.4}_{-0.3}$ km) and ($T_{\rm BB} = 2.16^{+0.06}_{-0.07} \times 10^6$ K, $R_{\rm BB} = 0.73^{+0.09}_{-0.07}$ km) plus a power law ($\Gamma = 2.2^{+0.4}_{-0.3}$). Their results showed that the cooler blackbody was probably related to the bulk of the neutron star surface, had a complex modulation, with two peaks per period separated by ~ 0.35 in phase and the radio pulse occuring in between. The hotter blackbody originating from a hot polar region had a nearly sinusoidal modulation with a single, broad maximum aligned with the second peak of the cooler blackbody, trailing the radio pulse by ~ 0.15 in phase. The nonthermal component, magnetospheric in origin, was present during only 20% of the pulsar's phase and appeared to be opposite to the radio pulse.

Abdo et al. (2009) used the Vela signal to verify *Fermi's* timing and angular resolution. They obtained a high-quality pulse profile, with photon energies above 0.03 GeV, which resolved pulse structure as fine as 0.3 ms, and a distinct third peak which shifted in phase with energy (see Figure 3.3). They furthermore found a phase-averaged power-law index of $\Gamma = 1.51^{+0.05}_{-0.04}$ with an exponential cutoff at $E_{\rm c} = 2.9 \pm 0.1$ GeV.

Using the *SST*, Danilenko et al. (2011) detected a pointlike object that is likely the IR counterpart of the Vela pulsar. The measured flux from the available multiwavelength spectrum of the

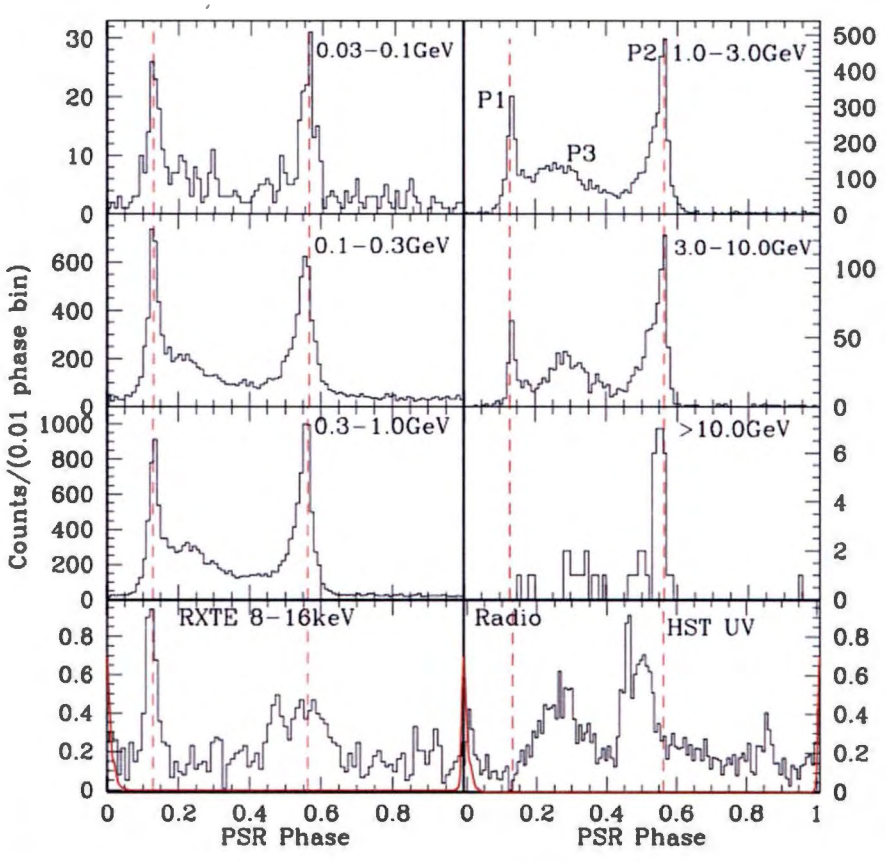

Figure 3.3: The energy-dependent pulse profile of the Vela pulsar. The dashed line shows the phases of the P1 and P2 peaks determined from the broadband light curve. The top right panel indicates the main peaks P1, P2, and P3. The bottom left panel shows the 8 keV−16 keV *RXTE* pulse profile of Harding et al. (2002) along with the radio pulse profile (in red). The lower right panel shows the 4.1 eV−6.1 keV *HST/STIS NUV* pulse profile of Romani et al. (2005). From Abdo et al. (2010).

Vela pulsar revealed a steep flux increase towards the IR.

3.2.2 Proper Motion of the Vela Pulsar

The proper motion of a star is its change in angular position over time. The study of the Vela pulsar's proper motion is important for the measurement of its distance as well as its offset from the centre of the SNR. It is furthermore seems that Vela's proper motion is roughly co-aligned with its spin magnetic axis (see Section 2.2.3).

Bignami & Caraveo (1988) compared the optical data from La Silla with the optical discovery plate of 1975.2 of the Vela pulsar (Lasker, 1976) to study its proper motion, and found an upper limit of 60 mas per year. This implied that, if its true age is comparable to its characteristic age ($P/2\dot{P}$ ~11 000 years), it was born no more than 10′ from its present position. The SN explosion which supposedly generated both the remnant and the pulsar must then have happened somewhere within a 10′ circle around the pulsar, so that the SN event must have taken place at a highly asymmetric position with respect to the current SNR. Alternatively, they suggested that pulsar PSR J0833−4510 and the Vela SNR are completely unrelated and are superposed by chance (Bailes et al. 1989 disputed this and estimated the probability of a chance association to be $\sim 10^{-3}$).

Another suggestion was that the Vela SNR and PSR J0833−4510 were much older than previously thought. (Bailes et al. 1989 estimated an age of 4 500 − 8 000 years for the SNR, implying a birth period of $P_0 = 43$ ms − 68 ms for the pulsar.)

Bailes et al. (1989) measured the proper motion of the Vela pulsar using the Parkes-Tidbinbilla Interferometer, and obtained a value of 49 ± 5 mas per year at a position angle of 305°. This proper motion implied that the pulsar was not born at the geometric centre of the Vela SNR, nor at the peak of radio emission in Vela X, and they therefore argued that Vela X is not pulsar-driven (plerionic). However, this view does not take into account that an SNR expanding in an inhomogeneous ambient medium will exhibit an asymmetric morphology. (e.g., Blondin et al., 2001).

Ögelman et al. (1989) found a proper motion of $\mu_\alpha \cos\delta = -26 \pm 6$ and $\mu_\delta = 28 \pm 6$ mas per year using ESO data, indicating that the Vela pulsar was born 7′ away from its present position towards the southeast. They concluded that the projected velocity (assuming a distance of 500 pc) was 90 ± 15 km/s . This is larger than the value of 52 ± 5 km/s derived from interstellar scintillation data (Cordes, 1986), and they therefore argued for a smaller distance of 290 ± 80 pc to make these velocities consistent.

Nasuti et al. (1997) used 20 years of optical data and found $\mu_\alpha \cos\delta = -47 \pm 3$ mas per year and $\mu_\delta = 22 \pm 3$ mas per year. They concluded that the Vela pulsar proper motion was 52 ± 5 mas per year at a position angle of 295°. De Luca et al. (2000) used 2 two years of *HST* WFC/WFC2 data of the Vela field to re-assess the proper motion and their measurement of $\mu = 52 \pm 3$ mas per year (with a position angle of $297° \pm 2°$) confirms the results obtained by Nasuti et al. (1997). Caraveo et al. (2001) reported the first optical measurement of the annual parallax of the Vela pulsar using *HST* Wide Planetary Camera 2 observations. They obtained a parallax of 3.4 ± 0.7, which implied a distance of 294^{-50}_{+76} pc, and a proper motion of $\mu_\alpha \cos\delta = -37.2 \pm 1.2$ mas per year, and $\mu_\delta = 28.2 \pm 1.3$ mas per year. Refer to Table 3.1 for a summary of proper motion measurements.

Dodson et al. (2003a) used the results from the very long baseline interferometry (VLBI) observations at 2.3 GHz and 8.4 GHz and obtained $\mu_\alpha \cos\delta = -49.68 \pm 0.06$, $\mu_\delta = 29.9 \pm 0.1$ mas per year and a parallax of 3.5 ± 0.2 mas, which implied a distance of 287^{+19}_{-17} pc. After they had subtracted the Galactic rotation and solar peculiar velocity, they obtained $\mu_* = 45 \pm 1.3$ mas per year with a

Table 3.1: Measurements of the Vela pulsar proper motion (e.g., De Luca et al., 2000).

Reference	μ (mas yr^{-1})	$\mu_\alpha \cos\delta$ (mas yr^{-1})	μ_δ (mas yr^{-1})	Waveband
Bignami & Caraveo (1988)	< 60	–	–	Optical
Ögelman et al. (1989)	38 ± 8	-26 ± 6	28 ± 6	Optical
Markwardt & Ögelman (1994)	49 ± 4	-41 ± 3	26 ± 3	Optical
Nasuti et al. (1997)	52 ± 5	-47 ± 3	22 ± 3	Optical
De Luca et al. (2000)	52 ± 3	-46 ± 2	24 ± 2	Optical
Caraveo et al. (2001)	46.7 ± 1.8	-37.2 ± 1.2	28.2 ± 1.3	Optical
Bailes et al. (1989)	49 ± 4	-40 ± 4	28 ± 2	Radio
Fomalont et al. (1992)	116 ± 62	-67 ± 20	-95 ± 75	Radio
Fomalont et al. (1997)	53 ± 7	-50 ± 5	-16 ± 18	Radio
Dodson et al. (2003a)	45 ± 1.3^a	-49.68 ± 0.06	29.9 ± 0.1	Radio

[a]This measurements take into account rotation of the Galaxy as well as the peculiar motion of the Sun in the local Galactic potential.

position angle of $301° \pm 1°.8$. This implied that the proper motion had a small but significant offset from the X-ray nebula's symmetry axis. These results are more accurate than those of Caraveo et al. (2001) and were derived by an independent method involving an unambiguous radio reference frame.

3.2.3 Vela Pulsar Glitches

Lyne (1987) commented that pulsars display irregularities in rotation rate of two main types: (i) random fluctuations known as 'noise', and (ii) a discrete discontinuity in rotation rate known as a 'glitch'. Glitches have been generally ascribed to the variable coupling between an NS's crust and its superfluid interior (e.g., Larson & Link, 2002). Alternatively, Jones (1998) argued that glitches might not originate in the crust, but rather in the stellar core due to interaction between neutron and proton vortices.

Vela was the first pulsar to exhibit the phenomenon of glitching (Helfand et al., 2001). Alpar et al. (1981) described how the regularities in the Vela pulsar timing data could be explained by a theory of giant glitches resulting from catastrophic unpinning events in the pinned crustal neutron super fluid, with post-glitch behaviour resulting from glitch-induced vortex creep. (Refer to Haskell et al. (e.g., 2012) for recent work on giant glitch models using a two-fluid hydrodynamical approach, involving realistic pinning forces.) Helfand et al. (2001) observed the Vela pulsar using *Chandra*, obtaining observations $\sim 3 \times 10^5$ s and $\sim 3 \times 10^6$ s after the 2001 glitch. They found that the glitch energy of the Vela pulsar had to be less than 10^{42} ergs.

3.3 Conclusion

3.3.1 The Vela SNR

Dwarakanath (1991) found a relatively steeper spectrum for Vela X compared to that of Vela YZ, concluding that the Vela SNR had a filled-centre morphology. Dubner et al. (1992) inferred that the Vela SNR was interacting along its northwestern border with a corner of an observed HI shell which is ten times denser than its environment. Duncan et al. (1996) found that the total-power image of Vela exhibited many filaments and loop-like structures, and that the northern side of the SNR displayed a pair of bright concentric arcs, defining the northern edge of the shell. They also found that on the southern edge, the emission fades smoothly into the background making it difficult to identify the remnant boundary unambiguously. Frail et al. (1997) resolved many fine overlapping filaments in the Vela X region and also found a bright filament tracing the eastern boundary of the X-ray cocoon first detected by Markwardt & Ögelman (1995). Dubner et al. (1998) observed a thin, roughly circular shell of radius ~22 pc in HI that delineates the outer border of the thermal X-ray emission. Bock et al. (1998) next identified this SNR as a member of the composite class, as the radio plerion consisted of both diffuse and filamentary emission, while the SNR showed concentric shell filaments having $H\alpha$ and X-ray counterparts.Alvarez et al. (2001) confirmed the plerionic nature of Vela X by showing that the spectrum of Vela X was relatively flat, steepening towards the outer edge (Vela Y and Vela Z). Dodson et al. (2003b) found that the Vela radio nebula consisted of a northern and a southern lobe, being more extended (in the GHz range) than previously thought (e.g., Bock et al. 1998). They observed a highly polarized structure, with the polarization vectors revealing a symmetry with respect to the spin axis of the pulsar. They lastly

noted that there is an absence of radio emission at the centre where the *Chandra* inner torus was found.

Milne (1968b) detetced faint optical emission together with bright, sharp filaments and diffuse nebulosities from the Vela X region. Miller (1973) found that the centre of the X-ray shell coincided with that of the optical SNR, and also observed scallop-like arches and filaments forming the western and northwestern rim. Van den Bergh et al. (1973) detected a region covered by the Vela SNR filaments spaning a diameter of 270′, its centre being enclosed by pulsar position. They also observed that the optical filaments increased in density near Vela X. Elliott et al. (1976) observed filamentary nebulosity of Hα, typical of many optical SNRs.Shull (1983) observed optical knots in filaments associated with a Vela SNR, and Sankrit et al. (2001) similarly studied the FUV counterpart of an X-ray knot.Nishikida et al. (2006) detected FUV emission from the Vela SNR having the same extent ($\sim 8°$) as the X-ray features.

Seward et al. (1971) detected diffuse emission from a region of about 5° below 2 keV in the Vela direction, as well as a point source close to the pulsar position. Gorenstein et al. (1974) found that the spectral data below 1.5 keV were consistent with thermal radiation from a hot plasma. They also observed that the X-ray Vela SNR was a fragmentary shell resembling the UV filaments. Moore & Garmire (1975) observed two bright regions of X-ray emission, the first lying north of Vela X, and the second slightly southwest of Vela Y. Kahn et al. (1983) found a discrete spectral feature around 0.6 keV and identified it with O VII and O VIII emission, confirming a scenario were the soft X-ray emission is due to a hot gas ($\sim 10^6$ K). Kahn et al. (1985) observed a highly asymmetrical and inhomogeneous X-ray structure, the spectrum of which could be described as thermal emission from hot gas which is nonuniform in density and temperature, but which is in approximate pressure equilibrium. Willmore et al. (1992) detected emission ($2.5 - 25$ keV) from several bright knots in the SNR shell suggesting the presence of blobs of material at a wide range of temperature. The observations of Aschenbach et al. (1995) revealed a faint X-ray shell, which was well described by a circle with a $\sim 8°.3$ diameter, indicating that the pulsar was $\sim 25'$ from the SNR centre. They furthermore detected six extended X-ray features outside the blast-wave front, possibly resulting from stellar fragments expelled by the explosion of the progenitor star.

3.3.2 The Vela Pulsar

The Vela pulsar is a famous rotation-powered NS with a period of $P = 89$ ms, spin-down luminosity of $\dot{E} = 7 \times 10^{36}$ erg s^{-1} and characteristic age of $\sim 11\,000$ years. Large et al. (1968) first discovered this pulsar at radio wavelengths, while Radhakrishnan et al. (1969) observed a narrow pulse and complete linear polarization. Harnden & Gorenstein (1973) found a point source at the pulsar position ($0.1 - 1.5$ keV), while Albats et al. (1974) claimed pulsed emission in the $10 - 30$ MeV range. Culhane et al. (1974) found that the $0.7 - 1.5$ keV spectrum was consistent with the one obtained by Kellogg et al. (1973) and suggested a low-energy turnover in the spectrum. Thompson et al. (1975) detected pulsed γ-ray emission consisting of two peaks lagging the single radio peak. Wallace et al. (1977) detected optical pulsations from Vela and noted that the Vela light curve were energy dependent. Kanbach et al. (1980) obtained a power-law spectrum with $\gamma = 1.89 \pm 0.06$ (50 MeV $- 3$ GeV). Harnden et al. (1985) found evidence for thermal emission in the $0.1 - 4.5$ keV band implying a surface temperature of $\sim 10^6$ K. Ögelman & Zimmermann (1989) observed the vicinity of the Vela pulsar, and their results indicated that the central source was softer than the surrounding regions, its spectrum being fitted by a blackbody. Ulmer et al. (1991) reported 2σ

upper limits to γ-ray pulsations from Vela (3.2 – 10 MeV). Kanbach et al. (1994) detected an average flux of $(7.8 \times 1.0) \times 10^{-6}$ photons cm^{-2} s^{-1} from the Vela pulsar, and also obtained a power-law spectrum with index $\Gamma = -1.70 \pm 0.02$. Yoshikoshi et al. (1997) found an upper limit to the pulsed emission from the pulsar of $(3.7 \pm 0.7) \times 10^{-13}$ photons cm^{-2} s^{-1} above 2.5 ± 1.0 TeV. Strickman et al. (1999) detected pulsations in the 2 – 30 keV band. They noted that the average pulsed *RXTE* spectrum joined smoothly to HE spectrum of *OSSE*, *COMPTEL*, and *EGRET*, providing strong evidence for a thermal rather than a nonthermal origin for the *ROSAT* data. Pavlov et al. (2001) found two nonthermal X-ray components ($\Gamma_1 = 1.5 \pm 0.3$ and $\Gamma_2 = 2.7 \pm 0.4$). Harding et al. (2002) confirmed these two components using *RXTE*, and also detected five peaks in the light curve. Shibanov et al. (2003) were first to detect nonthermal emission from the Vela pulsar in the near-IR, and suggested either a spectral break in the NUV-EUV range or the presence of an additional components dominating in the optical range. Mori et al. (2004a) probed the thermal pulsar emission using *XMM-Newton* and inferred the presence of a hydrogen atmosphere, with a surface B-field of 10^{12} G, temperature of about 7×10^5 K, and age of $\sim 10^4$ years. Romani et al. (2005) obtained an NUV light curve (observing 4 distinct peaks) and FUV phase-resolved spectrum. Aharonian et al. (2006a) published a 99.9% integral flux upper limits above 1 TeV of 7.6×10^{-13} cm^{-2} s^{-1} of the pulsar. Manzali et al. (2007) fitted a three-component model to the phase-integrated spectrum of Vela, consisting of two blackbodies (originating from the hot stellar surfaces) and a power law (of magnetospheric origin). Abdo et al. (2009) obtained a high-quality pulsed profile using *Fermi* LAT and found an exponentially cut-off phase-averaged spectrum with $\Gamma = 1.51^{+0.05}_{-0.04}$ and cut-off energy of $E_c = 2.9 \pm 0.1$ GeV. Danilenko et al. (2011) detected a pointlike object that is likely the IR counterpart of the Vela pulsar.

Several authors have studied the proper motion of the Vela pulsar over the past three decades using optical and radio data. The most accurate optical measurements yielded a proper motion of 52 ± 3 mas per year with a position angle of $297° \pm 2°$ (De Luca et al., 2000). In the case of the radio, Dodson et al. (2003a) obtained $\mu = 45 \pm 1.3$ mas per year with a position angle of $301° \pm 1°.8$, as well as a parallax of 3.5 ± 0.2 mas, implying a distance of 287^{+19}_{-17} pc.

Vela was the first pulsar to exhibit the phenomenon of glitching, which is thought to be related to variable coupling between an NS's crust and its superfluid interior. Helfand et al. (2001) observed the Vela pulsar using *Chandra* within days of the 2001 glitch and limited the glitch energy to $< 10^{42}$ erg.

Having summarized the multiwavelength properties of the Vela PWN as well as its surroundings in this and the previous chapter, we move on to the description of our optical observations and data analysis in the next chapter.

Chapter 4

Observations, Data Reduction and Analysis

In this chapter we are going to discuss our analysis of DSS data (Section 4.1) which was done in an attempt to localise the Vela X substructures, and as a "first look" approach to see if there are any hints of structure which may be associated with the putative Vela X synchrotron nebula. Next, we also discuss our optical observations using the SAAO 1.0 m telescope (Section 4.2), including our processing technique (Section 4.3) and the derivation of optical upper limits (Section 4.4). We lastly assess the effect of extinction (Section 4.5).

4.1 DSS Data and Analysis: Source Location and Preliminary Search for Vela X PWN Emission

Digital Sky Survey (DSS) is a set of all-sky photographic surveys in *E, V, J, R* and *N* bands done with a palomar and UK Schmidt telescope. Each plate covers 6.5° × 6.5°. The plates were scanned using a PDS microdensitometer to pixel sizes of either 25 or 15 micrometers, corresponding to 1.7″ or 1.0″ per pixel. The images from the different parts of the sky may be extracted from the DSS in either Flexible Image Transport System (FITS) format (Wells et al., 1981) or GIF format. In this study the FITS format was used. Bucciarelli et al. (2001) published the photometric sequence in the Johnson-Kron-Cousins standard system, which is useful for the calibration of photographic Schmidt survey plates. They calibrated the Second Guide Star Photometric Catalog (GSP-II), which is an all-sky catalog of photometric stellar sequence, with a limiting magnitude of $V=19$ or fainter in the B, V and R passbands, and standard photometric errors are at the level of ~ 0.07 for $V \sim 19$ magnitude.

ASCII plate list files contain limited metadata. The primary metadata are the plate identifiers and the right ascension and declination of the plate centre. These separate plate list files are used

Table 4.1: Positions of Vela X substructures (Dodson et al., 2003b).

Name	RA	Dec	size (arcminute^2)
Northern lobe	$08^h\ 35^m\ 11^s$	$-45°\ 07'\ 11''$	5.3
Southern lobe	$08^h\ 35^m\ 30^s$	$-45°\ 12'\ 59''$	18
Pulsar	$08^h\ 35^m\ 20^s$	$-45°\ 10'\ 35''$	Point source

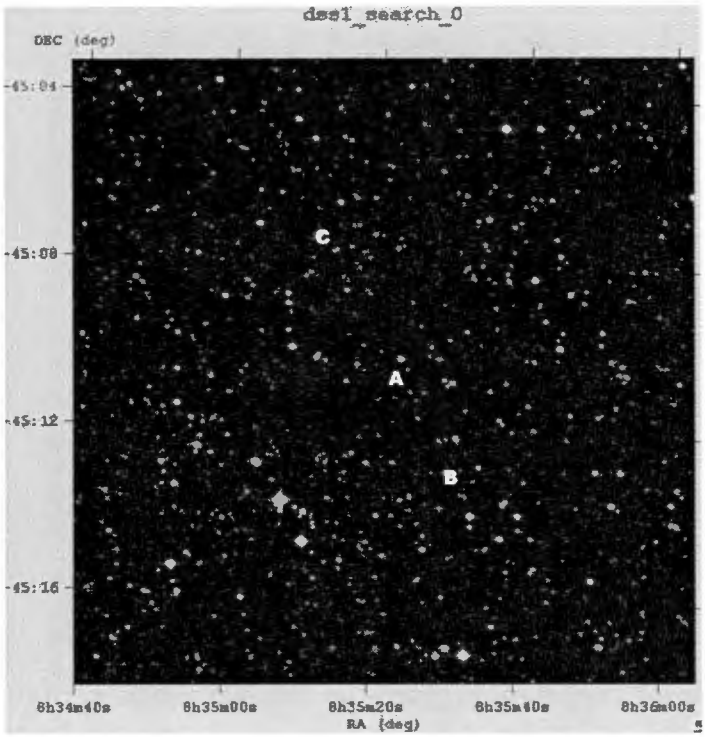

Figure 4.1: A DSS map around Vela X showing the position of the Vela pulsar (A), the southern lobe (B), and the northern lobe (C) covering an area of 15×15 arcminutes^2. Source positions are taken from Dodson et al. (2003b), see Table 4.1.

to separate the various surveys e.g., *R, B* or *NIR*.

We accessed public data from the DSS webpage (http://archive.stsci.edu/cgi-bin/dss). We used the pulsar source position from Dodson et al. (2003b) as given in Table 4.1 to select our data. We retrieved a 15×15 arcmin^2 image in FITS format as shown in Figure 4.1. The image size was $1\ 188 \times 1\ 190$ pixels^2. The field was centred on the Vela pulsar position (A). The northern (C) and southern (B) lobe positions are also shown, as inferred from Table 4.1. We wanted to test whether constructing contour plots of intensity using our SAAO data, similar to Figure 4.1, would be feasible. The size chosen was large enough to comprise all these structures we were interested in.

Since we are only interested in the source positions of the lobes and the Vela pulsar, we took a subset of the data of 594×594 pixels^2 centred on the pulsar. This smaller image encapsulates all of these sources. We then binned these DSS data by taking the average intensity for blocks of 9×9 pixels, and constructed an image plot spanning 66 rows and 66 columns (See Figure 4.2). Figure 4.3 shows a histogram of the number of pixels vs. intensity before subtraction of bright stars. From this distribution, we set an upper limit of 6 800 counts, removing bright stars exceeding this limit, and replacing these pixel values by a background level of 6 400 counts. The resulting intensity distribution is shown in Figure 4.4; note that the maximum of the y-axis extends up to about 2 500. For clarity, we set the axis maximum to 40. Note that the intensity distributions (before and after bright star subtraction) obtained for the prebinned 594×594 pixel^2 image resemble those for the binned image spanning 66 rows and 66 columns, and are therefore not shown.

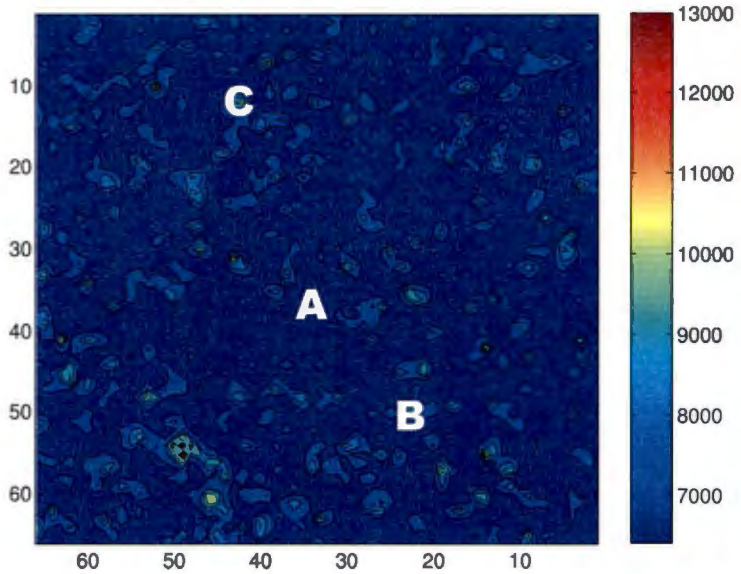

Figure 4.2: The same DSS map as in Figure 4.1, showing counts across the field of view, but with the data being binned to form an image spanning 66 rows by 66 columns. Bright stars have not been subtracted yet.

Figure 4.2 indicates contours of the binned DSS counts before subtraction of bright stars. This figure shows a 7.5×7.5 arcminute^2 field, indicating the positions of the Vela pulsar, the northern lobe and the southern lobe as indicated by "A", "B" and "C". These positions are also seen on the contour plot of the binned data, after subtraction of bright stars (Figure 4.5). We therefore localised the substructures by estimating these positions as follows. First, we used the results from Dodson et al. (2003b) in order to locate the position of the Vela pulsar, northern and southern lobes. Next, we compared the unbinned data (Figure 4.1) and the binned data (before subtraction of bright stars; Figure 4.2) to obtain the positions by noting the patterns made by the bright stars. Finally, we transferred these positions to Figure 4.5, where the bright stars have been removed. From this figure, we wanted to see if there is any detectable optical counterpart of Vela X (without calculating actual flux upper limits), but we also used this as a preliminary excercise and preparation for the observations and data analysis that were eventually done with the SAAO 1.0 m telescope at Sutherland (Section 4.2).

Near the estimated position of the Vela pulsar (A), only a background level of emission is observed and there is no structure visible that could be associated with a putative Vela X optical counterpart. This may be due to the fact that the diffuse PWN of Vela X is very faint at $\lesssim$ 27.5 mag arcsec^{-2} (Mignani et al., 2003). It is difficult to conclude that there is any emission from the Vela X southern lobe. From Figure 4.5 it is clearly evident that there is no visible optical counterpart to Vela X as observed from the DSS data.

4.2 Optical Observations and Instrumentation

Optical observations of Vela X were done at the SAAO in Sutherland using the 1.0 m telescope in February 2010 and March 2011 using the imaging CCD STE4, and BV filters. The 1.0 m telescope has two SITe back-illuminated detectors, which are a 1024×1024 pixel^2 CCD designated STE4 (see Table 4.2), or a 512×512 pixel^2 CCD designated STE3. The detector is contained within a cryostat

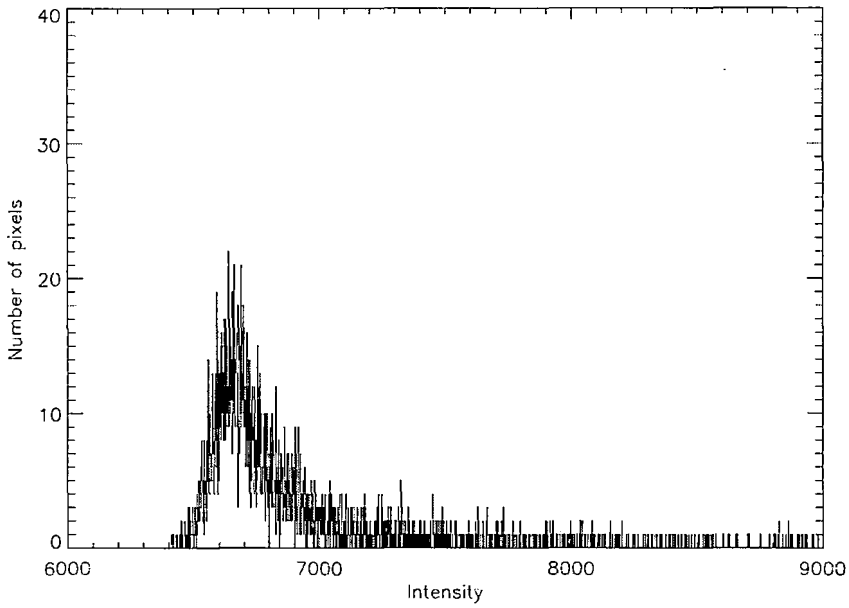

Figure 4.3: The intensity distribution of the DSS map in Figure 4.1 before subtraction of bright stars.

mounted at the Cassegrain focus with f-ratio from $f/20$ to $f/16$, together with a remotely-operated filter box and an autoguider. Bessell *UBVRI* filters are available for use with the SAAO CCD and are installed at all times, with an empty slot in the filter wheel for white light observations.

Vela X observations were done with exposure times of 120 seconds per frame for February 2010 observations in BV filters, and 1 200 seconds for the B filter and 600 seconds for V filter for March 2011 observations. The two sets of observations have different background levels given that they were taken at different times and for different exposures.

Flatfields were taken in twilight sky after sunset for both February 2010 and March 2011 observations. For each filter, several flatfields were combined to make a master flatfield that was used to flatfield the object's data in order to correct for pixel-to-pixel variations. All the data were trimmed and overscan subtracted before using the combined flatfields on the object frames. Data were all taken in a 2×2 binning mode.

Given that STE4 has a relatively small field of view of about $5'.3 \times 5'.3$, it was necessary to take a number of frames forming a mosaic around the pulsar position for each of the filters used in order to try and cover both the southern and the northern lobes of the Vela X PWN as detected in radio (Dodson et al., 2003b). The total mosaic around the pulsar was 3×3 frames covering an area of about $10' \times 10'$, after taking into account a $2'$ region of overlap between adjacent frames. This, unfortunately, still missed the northern lobe in 2010 and the southern lobe in 2011 observations, mainly due to the coordinates chosen as the centre of the field in both sets of observations.

Biases and dark counts were not used given that the STE4 is quite stable and de-biasing generally does not seem to improve the quality of the STE4 observations. An overscan region of the CCD frames was, instead, used for bias correction. The data were later reduced using Image Reduction and Analysis Facility (IRAF). The reduced data were kept as FITS files, which were later analyzed using both IRAF and Matlab.

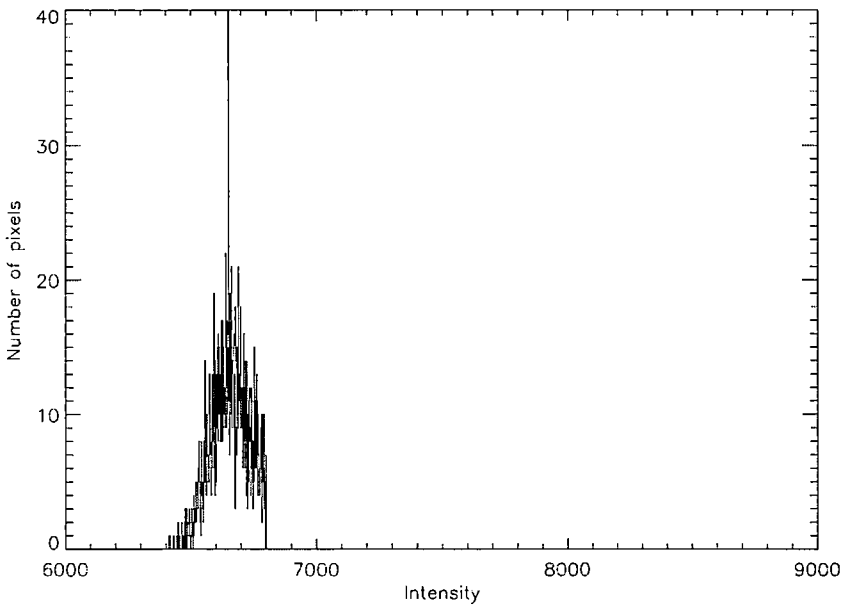

Figure 4.4: The intensity distribution of the DSS map in Figure 4.1 after subtraction of bright stars. The high-intensity pixels are replaced by the average background level of 6 400. Note that the maximum of the y-axis goes up to about 2 500.

Both 2010 and 2011 sets of observations were taken during moonless nights, and therefore only natural night sky brightness contributed to the sky background. The 1.0 m telescope can reasonably detect 18th magnitude stars within reasonable exposure times. The apparent magnitude of the Vela pulsar is 23.6, which would be relatively faint to detect with the 1.0 m telescope within reasonable exposure times. Vela is also in a very crowded region of the sky, the Galactic Plane, and therefore a considerable amount of background emission is expected from field objects in addition to the expected weak diffuse emission from the Vela X nebula (as was indeed the case also for the DSS data).

Table 4.2: Properties of the CCD, STE4 (SAAO, 2012).

Device Name	STE4
Manufacturer	SITe
Chip Type	Back-illuminated
Number of Pixels	1024×1024
Pixel Size	24 microns^2
Scale	0.31 arcsec/pixel
Field of View	317×317 arcsecs^2
Read Noise	6.5 electrons
Scale Factor	2.8 electrons/ADU
Linear Count Limit	65535 ADU
Readout Time	43 sec
Prebin Option	1×1 or 2×2
B	22.0 mag
V	22.4 mag

4.3 Data Processing

Following the application of reduction procedures to the SAAO data, we subtracted bright stars from all the flatfielded object frames (Table 4.3), replacing the subtracted pixel counts with a predetermined average background count level for each frame. We cut the intensities of the brightest stars at full width half maximum for each of the histograms as, e.g., presented in Figure 4.6 for the B filter. After the cut, we observe a large number of pixels at the intensity of 45 (Figure 4.7) which represents the pixels where we have replaced high intensities by the background level. The limit above which stars were removed was different for different frames.

We reduced the single-frame raw data of the illuminated detector comprising 512×512 pixel^2 to 510×510 pixel^2 to avoid null and empty values. Subsequently, we averaged blocks of 15×15 pixels, resulting in a 34×34 matrix. This was done for all 9 individual frames obtained in 2010 (for each filter), and also for the frames obtained in 2011. Next, we mosaicked these 9 frames (from 2010). First, we just added all 9 frames to give a 102×102 matrix. We took an overlap between frames of about $1'.0 - 2'.5$ into account and obtained averages at positions where overlapping occurred. This happened from left to right where columns 19 to 34 overlapped with columns 35 to 50, and 53 to 68 overlapped with 69 to 84. On the other hand, we found overlapping to occur from top to bottom, with row 39 to 49 overlapping with row 34 to 20, and 69 to 83 with 68 to 54. After overlapping the separate frames, and removing bright stars as described above, we obtained a final matrix of 70 rows and 72 columns from which the intensity contours were constructed (Chapter 5).

Table 4.3: Summary of observations, including position, date, coordinates, exposure time, and airmass.

Frame Name	Date	Coordinate (RA, DEC)	exposure time (s)	airmass
fba8050254.fits	2010-02-15	08:35:00 -45:12:36	120	1.04
fba8050259.fits	2010-02-15	08:35:00 -45:15:43	120	1.03
fba8050265.fits	2010-02-15	08:35:17 -45:15:43	120	1.03
fba8050271.fits	2010-02-15	08:35:17 -45:12:36	120	1.03
fba8050277.fits	2010-02-15	08:35:17 -45:09:33	120	1.03
fba8050354.fits	2010-02-16	08:35:34 -45:09:32	120	1.04
fba8050360.fits	2010-02-16	08:35:34 -45:12:36	120	1.03
fba8050366.fits	2010-02-16	08:35:34 -45:15:43	120	1.03
fba8050372.fits	2010-02-16	08:35:00 -45:09:32	120	1.03
fba8050255.fits	2010-02-15	08:35:00 -45:12:36	120	1.04
fba8050261.fits	2010-02-15	08:35:00 -45:15:43	120	1.03
fba8050267.fits	2010-02-15	08:35:17 -45:15:43	120	1.03
fba8050273.fits	2010-02-15	08:35:17 -45:12:36	120	1.03
fba8050280.fits	2010-02-15	08:35:17 -45:09:33	120	1.03
fba8050356.fits	2010-02-16	08:35:34 -45:09:32	120	1.04
fba8050362.fits	2010-02-16	08:35:34 -45:12:36	120	1.03
fba8050368.fits	2010-02-16	08:35:34 -45:15:43	120	1.03
fba8050374.fits	2010-02-16	08:35:00 -45:09:32	120	1.03
fba7800570.fits	2011-03-01	08:35:25 -45:09:12	1 200	1.03
fba7800571.fits	2011-03-01	08:35:25 -45:09:12	600	1.03

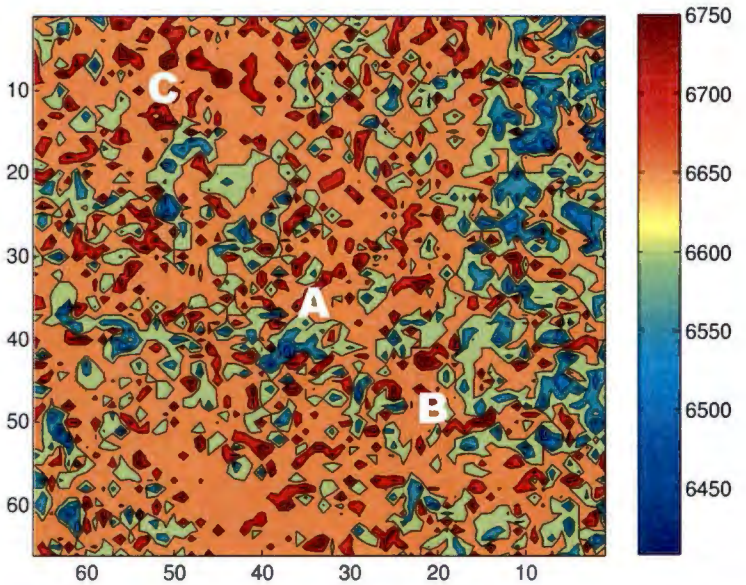

Figure 4.5: The contour of the same DSS map as in Figure 4.1, but with the bright stars subtracted. The background level counts are averaged over 9×9 pixels as explained in the text.

4.4 Upper Limit Calculation

The zero-point of an instrument is the magnitude of an object that produces one count (or data number, DN) per second. The zero-point magnitudes of the STE4 on the 1.0 m telescope for B and V are 22.0 and 22.4, respectively (Table 4.2). The upper limit magnitude for Vela X of both B and V were determined from the following expression (Baggett et al., 2002):

$$m = -2.5 \log_{10} \left(I/(2AB)^2 T \right) + m_0, \tag{4.1}$$

where I is the total number of counts in a selected block, m_0 is a zero-point magnitude for a given filter, T is the exposure time in seconds, A is the scale (given as 0.31 arcsec per pixel for STE4 on 1.0 m telescope) and B is a chosen block size expressed in number of pixels ($B = 15$ in our case). The factor 2 is included because the data were binned in the 2×2 mode. The total area of the 70×72 matrix with cells comprising 15×15 pixel^2, is about 100 arcsec^2. SA 98 standard stars (Landolt, 2009) were observed before and after the observations of the Vela X region in 2011. We corrected our instrumental magnitudes using the expression

$$m = 1.03m' - 0.8, \tag{4.2}$$

which was derived from plotting the instrumental magnitudes m' against actual catalogued magnitudes m of the known standard stars in SA 98.

It was actually not easy to find standard stars given that the PWN is an extended source and covers a large area. They were assumed to be the same for 2010, given that the same instrument/telescope combination was used and with similar setup for the two years, so that the correction of magnitudes could not have varied significantly. The standard stars were used to scale the estimated instrumental magnitudes of the Vela region to the standard system. The results of standard star corrections are given in the following chapter.

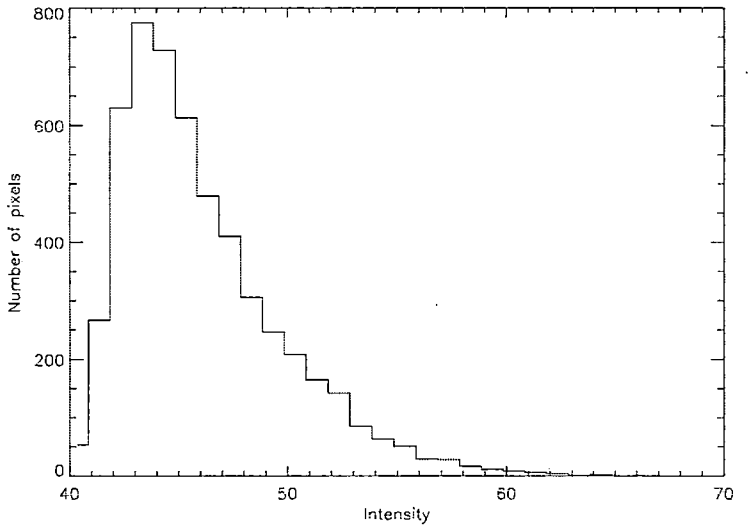

Figure 4.6: Intensity distribution of the Vela X region for the mosaic containing 3 × 3 frames for the B filter of the 1.0 m SAAO telescope, for the 2010 observations (before bright star subtraction).

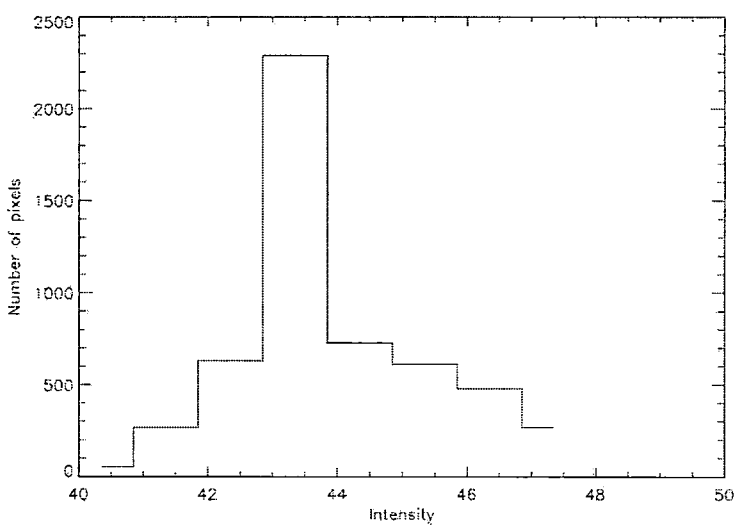

Figure 4.7: Intensity distribution of the Vela X region for the mosaic containing 3 × 3 frames for the B filter of the 1.0 m SAAO telescope, for the 2010 observations (after bright star subtraction).

Finally, we calculated the implied flux using

$$F_\nu = F_{\nu,0} 10^{-0.4m}, \tag{4.3}$$

where $F_{\nu,0} = 4260$ Jy for the B band, and $F_{\nu,0} = 3640$ Jy for the V band are fluxes for a standard star with $m = 0$ in both B and V (Bessell, 1979). To derive an upper limit for the full cocoon size, we scaled our flux to extend over an area of 45×12 arcmin^2, making the implicit assumption that the background is roughly similar for the region centred on the pulsar and the cocoon region.

4.5 The Effect of Extinction

Extinction is the loss of light in the atmosphere from a directly transmitted beam. When light travels through the earth's atmosphere some photons collide with atoms, molecules, water droplets, grains of dust, and other objects. The results of these collisions may lead to photons being absorbed or scattered into different directions. This loss causes the photons to no longer reach the observer on the ground and fewer light rays may be detected from the star than expected on an air-free planet (Richmond, 2012). We consider three sources of extinction and their impact on our observations below.

Circumstellar extinction is the scattered radiation of the central star which can be caused by three processes: (1) screening of the stellar light by dust, (2) screening by the IR excess, and (3) scattering of the light of the central star in the visual and in the UV band. In this case the intrinsic properties of the central star cannot be determined accurately because of the dust around the object (Voshchinnikov et al., 1996). Circumstellar extinction is unlikely to be significantly important for Vela X region.

Interstellar extinction is the obscuration of stars by dust in the Galaxy as we see them on earth. The stars which are close enough to earth are partially obscured, i.e., interstellar extinction depends on the position and the distance of the source. Notably, different wavelengths will also suffer different amounts of obscuration for a given distance through the dust (Pasachoff, 2002). For Vela, interstellar extinction will not necessarily be crucial due to the fact that Vela is not far from the earth, lying at about 0.29 kpc. Interstellar extinction, for example, would be an issue for objects which are far much farther away in the direction of Vela.

Lastly, the average atmospheric extinction for the B band is 0.3 and for the V band is 0.2 as determined from Sutherland site. Therefore, atmospheric extinction is not expected to have a serious impact on the upper limits we obtained for Vela X. Correcting for atmospheric extinction would result in our upper limit magnitudes becoming even less constraining, and would have no impact on the models.

Chapter 5

Results

In this chapter we discuss our results, specifically our attempts to resolve the optical counterpart of Vela X (Section 5.1), and our upper limit calculations using data from the 1.0 m telescope at Sutherland (Section 5.2). We also briefly discuss the reasons for not combining multiple images in cases where several images were taken for the same source location and wavelength (Section 5.3).

5.1 Resolving the Optical Morphology of Vela X

Following similar arguments as in Section 4.1 for the DSS data, we analysed data obtained from Sutherland using the SAAO 1.0 m telescope (Section 4.2 and 4.3). We developed similar contour plots using data from our Sutherland observations. The results were data matrices of 70 rows and 72 columns for each of the B and V bands, with the cells of these matrices comprising blocks of 15×15 pixels^2 as discussed in Chapter 4. We constructed the intensity contour plots to see whether there were any structures related to the optical counterpart of Vela X, and also to find optical upper limits for this PWN.

We first attempted to resolve the optical structure in our image mosaic consisting of 9×9 frames, for both B and V filters. As explained in Chapter 4, we removed the bright stars and replaced them with the average background level (See Figure 4.6 and 4.7 for the intensity distributions before and after the bright stars has been removed).

Figure 5.1 shows a contour plot of counts for the B filter of the STE4 CCD from 2010 observations, similar to Figure 4.5 constructed using DSS data. The plot for the V filter is very similar, and therefore not shown. The observations covered an area of about 10 arcminutes^2, including the Vela pulsar (A) and the southern lobe (B). This field of view is very small compared to the size of the X-ray cocoon, which has a size of $45' \times 12'$ extending towards the southern direction (Markwardt & Ögelman, 1995). This implies that our contour plot is entirely located inside the cocoon. There is no evidence of any structures around the Vela pulsar position. Around the position of the southern lobe there is nothing much that can be attributed to the optical counterpart either. From Figure 5.1, we therefore conclude that there is no significant structure or emission that could be interpreted as an optical counterpart close to the Vela pulsar, or coinciding with the southern radio lobe of Vela X, from our 2010 observations.

Figure 5.2 shows an intensity contour plot for the B filter for our 2011 observations, with a background level of about 400 counts. Note that the average number of counts is about 10 times larger than that of Figure 5.1. This is due to the fact that our exposure time was 10 times longer during our 2011 observations, compared to those performed in 2010. When looking at the position

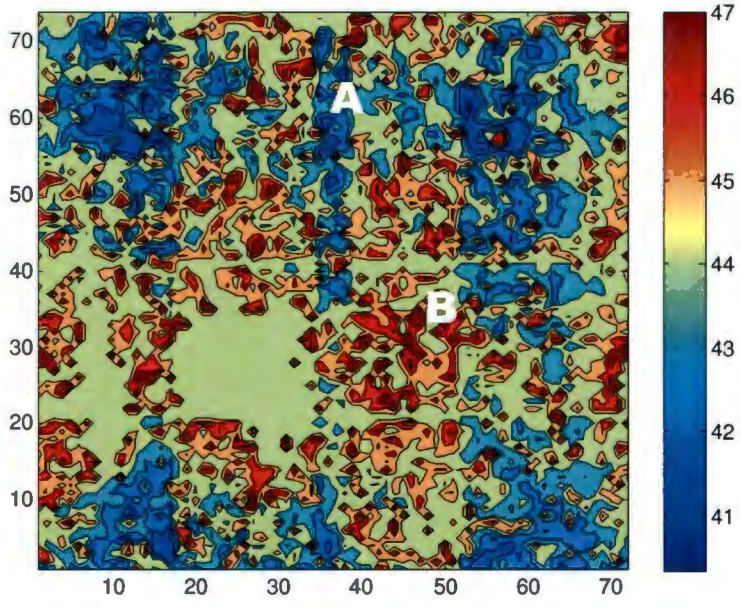

Figure 5.1: The region around Vela X, with the position of the Vela pulsar and the southern lobe in the B filter from 2010 observations, indicated by "A" and "B".

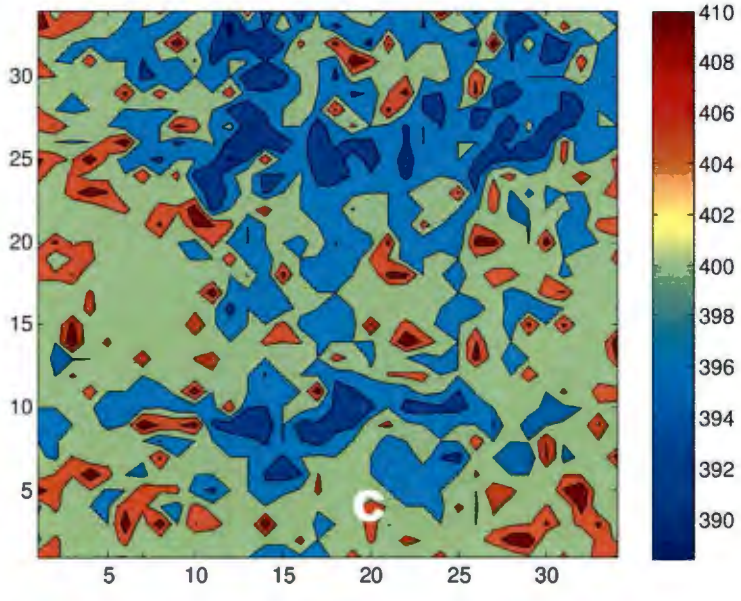

Figure 5.2: The B filter intensity contour of Vela X from 2011 observations, with the northern lobe indicated by "C".

of the northern lobe (C), one only sees background-level emission. This is similar to the case of the V filter. We therefore conclude that there is no structure related to the Vela PWN from observations taken at Sutherland in 2011. We find that there are no apparent structures in our optical observations of Vela that could be associated with either the X-ray cocoon or the radio lobes of the Vela X PWN.

The nondetection of the optical counterpart with the combination of telescope (1.0 m), and instrument (STE4) that was used could be due to a number of reasons, including the fact that the 1.0 m telescope is not big enough for this kind of observation. Vela X is in a very crowded region

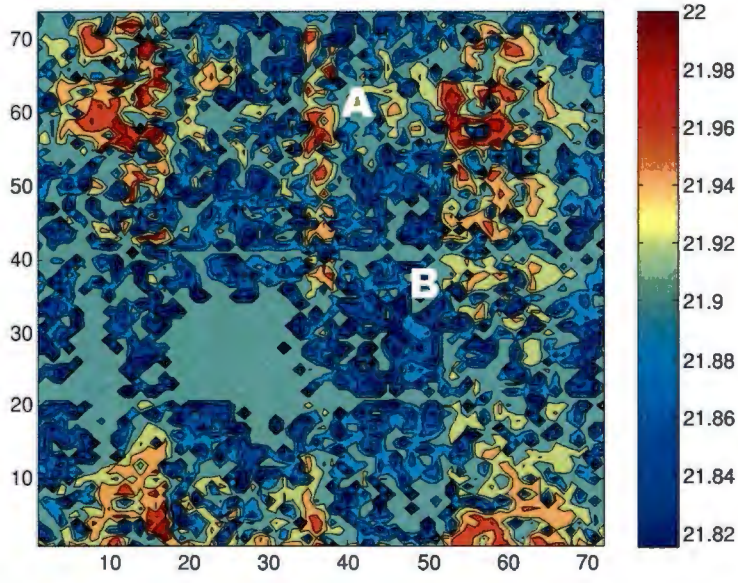

Figure 5.3: Magnitude upper limits (mag arcsec^{-2}) in the B band obtained for the region around the Vela pulsar (A) and southern radio lobe (B) using 2010 SAAO data. Axes labels indicate the block number.

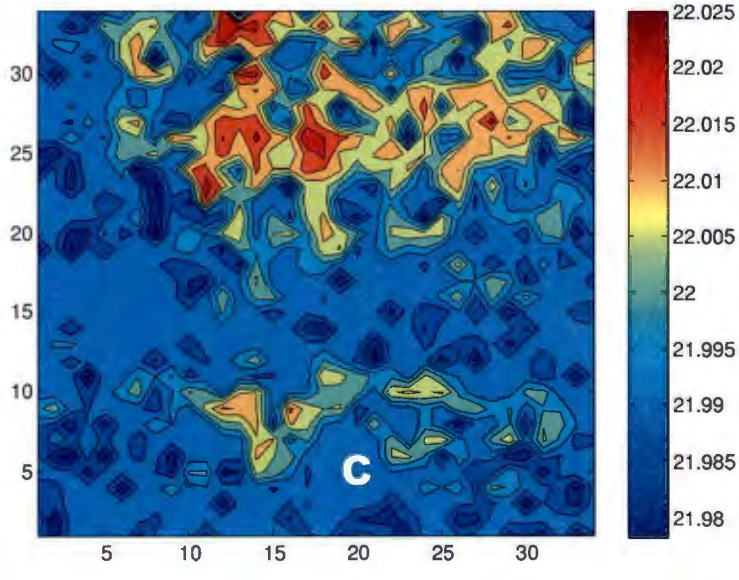

Figure 5.4: Magnitude upper limits (mag arcsec^{-2}) in the B band obtained for the region around the northern radio lobe (C) using 2011 SAAO data. Axes labels indicate block number.

of the sky. It is therefore possible that the Vela X nebula extends beyond the size of the region that was observed, and that any background subtraction resulted in subtracting the source diffuse emission as well.

5.2 Optical Upper Limits

The zero-point magnitudes on the 1.0 m telescope using the STE4 are specified as $B = 22.0$, and $V = 22.4$ (SAAO, 2012). Using these and the data collected during February 2010, we obtained

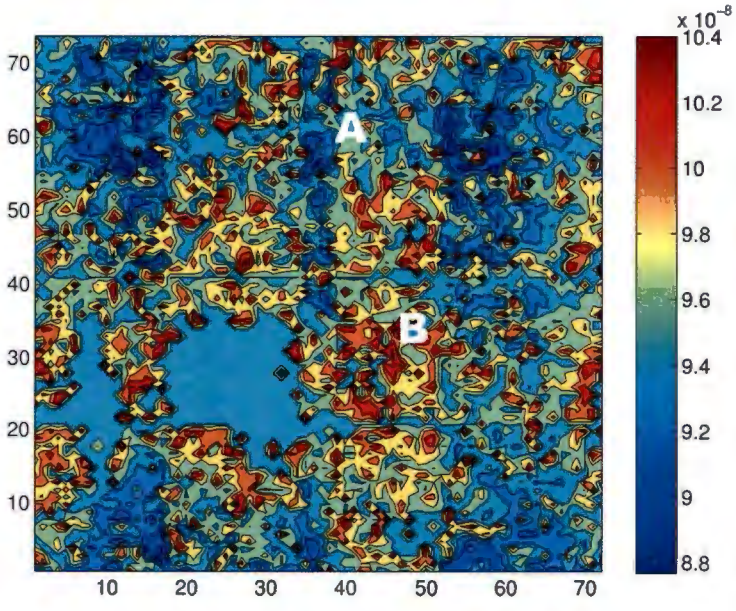

Figure 5.5: Flux upper limits (νF_ν in units of erg s^{-1} cm^{-2}) in the B band obtained for the region around the Vela pulsar (A) and southern radio lobe (B) using 2010 SAAO data.

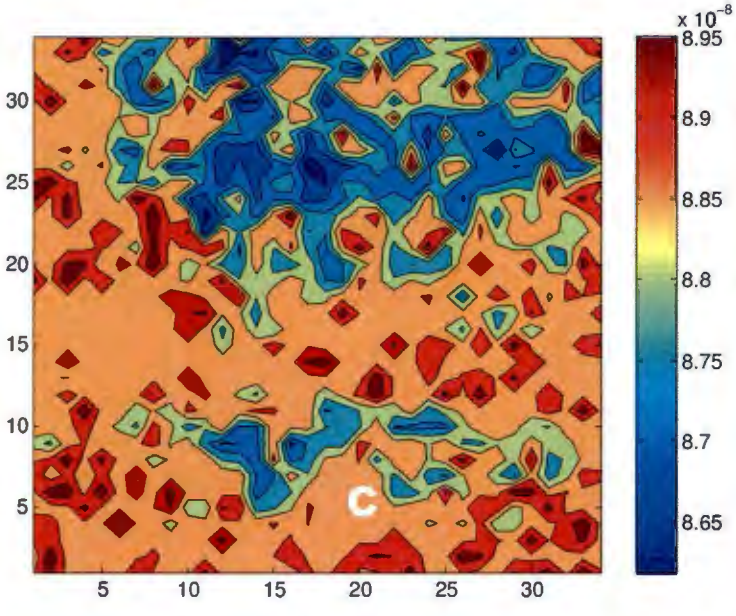

Figure 5.6: Flux upper limits (νF_ν in units of erg s^{-1} cm^{-2}) in the B band obtained for the region around the northern lobe (C) using 2011 SAAO data.

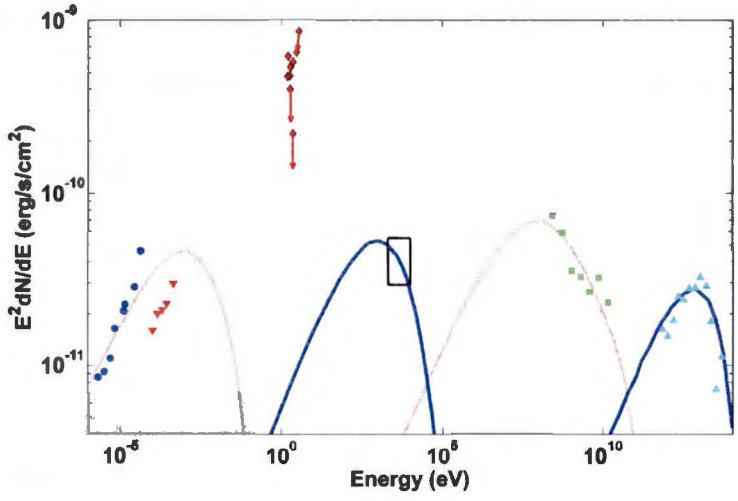

Figure 5.7: Spectral energy density plot of Vela X. Data and models are taken from Hinton et al. (2011). The optical upper limits (red diamonds with arrows) have been calculated using Mignani et al. (2003). The red dashed lines are for the extended radio nebula (ERN) while the blue lines are for the X-ray cocoon.

upper limits for B and V filters of 21.8 (Figure 5.3) and 21.6 mag arcsec^{-2}, respectively, around the Vela pulsar (A) and the southern radio lobe (B). The lowest values of magnitude for B and V filters are 21.7 and 21.0 mag arcsec^{-2}, respectively, while the highest (dimmest) magnitudes obtained for both B and V filters are 21.9 and 21.9 mag arcsec^{-2}. The lowest magnitudes for both B and V filters are similar to the average natural night sky brightness measurements at Sutherland for a dark/moonless night.

The data collected in March 2011 lead to slightly different upper limits for both B and V, compared to the ones obtained from February 2010 data. The upper limits for the March 2011 data for the B and V filters are 22.0 and 21.6 mag arcsec^{-2}, respectively. The lowest magnitudes for both B and V are 22.0 (Figure 5.4)and 21.6 mag arcsec^{-2}, while, on the other hand, the highest (dimmest) values of magnitude around the field for B and V are just above 22.0 and 21.7 mag arcsec^{-2}. Figure 5.3 and 5.4 represent the contour plots of the magnitude per arcsec^2 of the B filter, for 2010 and 2011 data, respectively. We applied the same procedure for all filters. It should be noted that these upper limits were not airmass or extinction corrected.

Our νF_ν upper limits for March 2010 were $\sim 9.6 \times 10^{-8}$ erg s^{-1} cm^{-2} for the B band, and $\sim 7.5 \times 10^{-8}$ erg s^{-1} cm^{-2} for the V band, around positions A and B. The lowest fluxes for B and V for the 2010 observations are 8.7×10^{-8} erg s^{-1} cm^{-2} and 6.9×10^{-8} erg s^{-1} cm^{-2}, and the highest fluxes are 1.0×10^{-7} erg s^{-1} cm^{-2} for B and 8.1×10^{-8} erg s^{-1} cm^{-2} for V. On the other hand, the νF_ν upper limit fluxes for the 2011 observations around the northern radio lobe are 8.8×10^{-8} erg s^{-1} cm^{-2} for B and 8.4×10^{-8} erg s^{-1} cm^{-2} for V. The lowest fluxes for B and V are 8.6×10^{-8} and 8.1×10^{-8} erg s^{-1} cm^{-2}, respectively, while the highest values for the fluxes are 9.0×10^{-8} erg s^{-1} cm^{-2} for B and 8.6×10^{-8} erg s^{-1} cm^{-2} for V (see Figure 5.5 and 5.6).

In order to compare with other optical studies, we converted U, B, V, R, and I upper limits found in Mignani et al. (2003), using *Hubble Space Telescope (HST)*, *NTT*, and *Very Large Telescope (VLT)*, to νF_ν values assuming the optical source size to be the same as that of the X-ray cocoon. These upper limits are indicated as red triangles in Figure 5.7, along with multiwavelength data and models for the broadband spectrum of Vela X (Hinton et al., 2011). We note that our upper

and models for the broadband spectrum of Vela X (Hinton et al., 2011). We note that our upper limits are much less constraining than the ones obtained by Mignani et al. (2003), and are therefore not indicated on Figure 5.7. Even the upper limits from Mignani et al. (2003) did not constrain the broadband SED models (see Chapter 6, where we discuss the implications of this more fully).

5.3 Stacking of Several Images

Apart from the frames discussed above that we obtained in 2010, we actually obtained two additional frames at each position in the B and V bands during that time. We however used only one exposure per position. The reason for taking three exposures for each position was that we planned to eventually combine the frames to increase signal-to-noise ratio. However, comparison with observations done in 2011, where exposure times were up to 10 times longer, made us decide that combining the three frames per position, taken in 2010, would not give significantly better results. The upper limits will remain unconstraining even after stacking 3 frames totalling about 360 seconds per position (instead of 120 seconds). There is no visible source on the single-exposure frames, so even if we did stack 3 frames, we believe that there would be little improvement, and this did not warrant us to pursue the matter any further.

Chapter 6

Conclusions

The search for the Vela PWN in optical wavelengths is crucial to understanding its morphology, and how energy is distributed throughout the multiwavelength spectra. If the optical counterpart were to be found, it would be possible to investigate morphological changes between the radio and optical lobes. This investigation was going to contribute to the understanding of the dynamic Vela X compact nebula.

It is a challenge to resolve the extended structure of Vela X in the optical waveband, given that many sources contribute to the background radiation, as well as its apparent intrinsic faintness. For example, Mignani et al. (2003) reported relatively deep optical upper limits using *HST, NTT,* and *VLT* data. It is very likely that just a slightly deeper optical observation would have allowed them to detect the outer/inner arc (and the other bright elements of the inner PWN), while much deeper optical observations are needed to detect the emission from the Vela PWN at large. In our observations, on the other hand, we attempted to increase our resolving sensitivity by probing a relatively larger area in the direction of Vela by taking multiple optical images forming a mosaic around the Vela X radio lobes and the pulsar position. We also tried relatively long exposure times of up to 20 minutes per frame in order to increase the possibility of detecting the system. In spite of all these efforts, we only detected background-level optical emission near the Vela pulsar position, and there was no structure visible that could be associated with a possible Vela X optical counterpart. When comparing the X-ray and radio emission, it is found that the radio emission starts at a distance from the centre where X-ray emission terminates (Dodson et al., 2003b). It is not clear from our results where the optical emission would be and what shape it would take.

Another aim was to see whether the leptonic spectrum responsible for producing the radio synchrotron lobe also extends into the optical domain. Published results from optical, radio and X-ray observations from different telescopes such as *NTT*, *Spitzer*/IRAC, *Chandra*/HRC-I, and ATCA were used to attempt to constrain the spectral shape in the radio, optical, and X-ray bands (Figure 5.7). In addition, we obtained optical νF_ν upper limits of approximately 10^{-7} erg s^{-1} cm^{-2}, which are not constraining for a multiwavelength model of Vela X's emission.

We note that our upper limits suffer from several observational factors that introduce uncertainties. Removal of bright or even fainter unresolved point sources remains problematic. While our integration times were not long enough to resolve Vela X, they were too long in the sense that bright stars in the fields that we observed saturated the CCD. Furthermore, the field of view of the telescope is too small to capture the full extent of the source, and we had to use a method of mosaicking several single images in order to obtain one large image that includes the probable ex-

tension of the optical source. Changing conditions between the constituent frames add complexity and uncertainty to our analysis.

Neither our optical limits nor those of others have proved to be constraining for a spectral model of Vela X. Barring the γ-ray data for the moment, one may model the radio, optical, and X-ray data with *either* a single or double synchrotron component, implying *either* a single or multi-component electron spectrum interacting with the PWN magnetic field. On the other hand, the *Fermi* LAT and H.E.S.S. data are consistent with a *two-component* leptonic interpretation (Abdo et al., 2010) first put forward by De Jager (2007) and subsequently elaborated on by De Jager et al. (2008). We were hoping to confirm the two-component leptonic interpretation, as suggested by the γ-ray data, by our optical observations.

A second model (Hinton et al., 2011) invokes a single electron population, but then assumes different diffusive properties for the $2^\circ \times 3^\circ$ extended radio nebula (ERN) and $45' \times 12'$ X-ray cocoon regions (although the H.E.S.S. cocoon is quite more extensive). In essence, this is a different way of constructing a two-component electron injection spectrum. The particles are assumed to be contained within the ERN until the reverse shock from the SNR interacts with the ERN, and diffusive transport starts to take place. Older particles escape from the ERN, while newly-injected particles are thought to suffer significant cooling in the high B-field region near the pulsar before being injected into the low B-field cocoon. Within such a scenario, each substructure (the ERN or cocoon) is responsible for different components of the multiwavelength spectrum (radio and GeV vs. X-ray and TeV).

New H.E.S.S. observations (Abramowski et al., 2012) revealed that the VHE morphology seems to be intermediate between the X-ray and radio morphologies, being even more extended than previously thought. Furthermore, no evidence of electron cooling is found in the VHE data. This new information implies a revision of earlier broadband models of Vela X, possibly including energy-dependent diffusive escape (as done by Hinton et al. 2011) and/or stochastic re-acceleration.

Our optical limits are not violated by models such as those of De Jager et al. (2008) and Hinton et al. (2011), although the available limits support the idea of particle escape from the ERN (i.e., a lower synchrotron flux component). Deeper optical observations as well as refined multiwavelength modelling should continue to enhance our understanding of this complex source.

We conclude that deeper optical observations are needed to detect the emission from the Vela PWN, which may allow detection of the inner and the outer arc in optical, as detected in X-rays. A relatively large field of view that would, for example, cover the entire radio (both southern and northern) lobes simultaneously would be ideal to reduce the complexity resulting from taking multiple images around the system. A future optical detection would lastly prove very valuable to constrain the acceleration properties of relativistic particle within the complex Vela X source.

Bibliography

Abdo, A. A., et al. 2009, *ApJ*, 696, 1084

—. 2010, *ApJ*, 713, 146

Abramowski, A., et al. 2012, *ArXiv:1210.1459*

Ackermann, M., et al. 2011, *ApJ*, 726, 35

Aharonian, F., et al. 2006a, *A&A*, 448, L43

—. 2006b, *A&A*, 448, L43

Albats, P., Frye, G. M., & Thomson, G. B. 1974, *Nature*, 251, 400

Allen, R. H. 1963, Star names: Their lore and meaning (New York: Dover)

Alpar, M. A., Anderson, P. W., Pines, D., & Shaham, J. 1981, *ApJ*, 249, L29

Alvarez, H., Aparici, J., May, J., & Reich, P. 2001, *A&A*, 372, 636

Aschenbach, B., Egger, R., & Trümper, J. 1995, *Nature*, 373, 587

Baade, W., & Zwicky, F. 1934, *Proc. Nat. Acad. of Science*, 20, 259

Baggett, S., et al. 2002, In HST WFPC2 Data Handbook, v.4.0, ed. B. Mobasher, (Baltimore: STSci)

Bailes, M., Manchester, R. N., Kesteven, M. J., Norris, R. P., & Reynolds, J. 1989, *ApJ*, 343, L53

Bednarek, W., & Bartosik, M. 2003, *A&A*, 405, 689

Bessell, M. S. 1979, *PASP*, 91, 589

Bietenholz, M. F., Frail, D. A., & Hankins, T. H. 1991, *ApJ*, 376, L41

Bignami, G. F., & Caraveo, P. A. 1988, *ApJ*, 325, L5

Blondin, J. M., Chevalier, R. A., & Frierson, D. M. 2001, *ApJ*, 563, 806

Blumenthal, G. R., & Gould, R. J. 1970, *Rev. Mod. Phys.*, 42, 237

Bock, D. C.-J., Sault, R. J., Milne, D. K., & Green, A. J. 2002, in Neutron Stars in Supernova Remnants, Vol. 271, *ASP. Conf. Ser*, ed. P. O. Slane & B. M. Gaensler, 187

Bock, D. C.-J., Turtle, A. J., & Green, A. J. 1998, *ApJ*, 116, 1886

Bowers, R., & Deeming, T. 1984, Astrophysics II: Interstellar matter and Galaxies (New York: Jones & Bartlet)

Branch, D., et al. 1982, *ApJ*, 252, L61

Bucciarelli, B., et al. 2001, *A&A*, 368, 335

Büsching, I., de Jager, O. C., Potgieter, M. S., & Venter, C. 2008, *ApJ*, 678, L39

Cameron, A. G. 1959, *ApJ*, 130, 884

Caraveo, P. A., De Luca, A., Mignani, R. P., & Bignami, G. F. 2001, *ApJ*, 561, 930

Chevalier, R. A. 1977, in *Astrophys. and Space Science Lib.*, Vol. 66, *Supernovae*, ed. D. N. Schramm, 53

Chevalier, R. A. 1982, *ApJ*, 258, 790

Clark, D. H., & Caswell, J. L. 1976, *MNRAS*, 174, 267

Condon, J. J., & Ransom, S. M. 2010, http://www.cv.nrao.edu/course/astr534/ERA.shtml, [accessed: 1 October 2012]

Cordes, J. M. 1986, *ApJ*, 311, 183

Culhane, J. L., Cruise, A. M., Rapley, C. G., & Hawkins, F. J. 1974, *ApJ*, 190, L9

Cutnell, J. D., & Johnson, K. W. 1995, Physics, 3rd ed. (New York: John Wiley & Sons)

Dame, T. M., et al. 1987, *ApJ*, 322, 706

Danilenko, A. A., Zyuzin, D. A., Shibanov, Y. A., & Zharikov, S. V. 2011, *MNRAS*, 415, 867

Davies, R. D., & Gardner, F. F. 1970, *Aust. J. Phys*, 23, 59

Day, G. A., Caswell, J. L., & Cooke, D. J. 1972, *Aust. J. Phys. Astrophys. Suppl*, 25, 1

Dazeley, S. A., Patterson, J. R., Rowell, G. P., & Edwards, P. G. 2001, *Astropart. Phys*, 15, 313

De Jager, O. C. 2007, *ApJ*, 658, 1177

De Jager, O. C., & Djannati-Ataï, A. 2008, *ArXiv:0803.0116*

De Jager, O. C., & Harding, A. K. 1992, *ApJ*, 396, 161

De Jager, O. C., Harding, A. K., Sreekumar, P., & Strickman, M. 1996a, *A&A*, 120, C441

De Jager, O. C., Harding, A. K., Sreekumar, P., & Strickman, M. S. 1995, in *ICRC*, Vol. 2, 174

De Jager, O. C., Harding, A. K., & Strickman, M. S. 1996b, *ApJ*, 460, 729

De Jager, O. C., Slane, P. O., & LaMassa, S. 2008, *ApJ*, 689, L125

De Luca, A., Mignani, R. P., & Caraveo, P. A. 2000, *A&A*, 354, 1011

Dodson, R., Legge, D., Reynolds, J. E., & McCulloch, P. M. 2003a, *ApJ*, 596, 1137

Dodson, R., Lewis, D., McConnell, D., & Deshpande, A. A. 2003b, *MNRAS*, 343, 116

Dubner, G., Giacani, E., Cappa de Nicolau, C., & Reynoso, E. 1992, *A&AS*, 96, 505

Dubner, G. M., Green, A. J., Goss, W. M., Bock, D. C.-J., & Giacani, E. 1998, *AJ*, 116, 813

Duncan, A. R., Stewart, R. T., Haynes, R. F., & Jones, K. L. 1996, *MNRAS*, 280, 252

Dwarakanath, K. S. 1991, *A&A*, 12, 199

Elliott, K. H., Goudis, C., & Meaburn, J. 1976, *MNRAS*, 175, 605

Enomoto, R., et al. 2006, *ApJ*, 638, 397

Erber, T. 1966, *Rev. Mod. Phys.*, 38, 626

Fomalont, E. B., Goss, W. M., Lyne, A. G., Manchester, R. N., & Justtanont, K. 1992, *MNRAS*, 258, 497

Fomalont, E. B., Goss, W. M., Manchester, R. N., & Lyne, A. G. 1997, *MNRAS*, 286, 81

Frail, D. A., Bietenholz, M. F., Markwardt, C. B., & Ögelman, H. 1997, *ApJ*, 475, 224

Gaensler, B. M., & Slane, P. O. 2006, *ARAA*, 44, 17

Giacobbe, F. W. 2005, *Electronic Journal of Theoretical Physics*, 2, 060000

Gorenstein, P., Harnden, J. F. R., & Tucker, W. H. 1974, *ApJ*, 192, 661

Green, A. J. 1974, *A&AS*, 18, 267

Grenier, I. A., Hermsen, W., & Clear, J. 1988, *A&A*, 204, 117

Hales, A. S., et al. 2004, *ApJ*, 613, 977

Harding, A. K., Strickman, M. S., Gwinn, C., Dodson, R., Moffet, D., & McCulloch, P. 2002, *ApJ*, 576, 376

Harnden, F. R., & Gorenstein, P. 1973, *Nature*, 241, 107

Harnden, J. F. R., & Grant, P. D. 1983, in *BAAS*, Vol. 15, 1006

Harnden, J. F. R., Grant, P. D., Seward, F. D., & Kahn, S. M. 1985, *ApJ*, 299, 828

Harnden, J. F. R., Hertz, P., Gorenstein, P., Grindlay, J., Schreier, E., & Seward, F. 1979, in *BAAS*, Vol. 11, 424

Hartle, J. B. 2003, *An introduction to Einstein's general relativity* (San Francisco: Addison Wesley)

Haskell, B., Pizzochero, P. M., & Sidery, T. 2012, *MNRAS*, 420, 658

Haslam, G., Wielebinski, R., & Priester, W. 1982, *S&T*, 63, 230

Helfand, D. J., Gotthelf, E. V., & Halpern, J. P. 2001, *ApJ*, 556, 380

Hewish, A., Bell, S. J., Pilkington, J. D. H., Scott, P. F., & Collins, R. A. 1968, *Nature*, 217, 709

Hinton, J. A., Funk, S., Parsons, R. D., & Ohm, S. 2011, *ApJ*, 743, L7

Horns, D., Aharonian, F., Santangelo, A., Hoffmann, A. I. D., & Masterson, C. 2006, *A&A*, 451, L51

Jones, F. C. 1968, *Phys. Rev.*, 167, 1159

Jones, P. B. 1998, *MNRAS*, 296, 217

Kahn, S. M., Brodie, J., Bowyer, S., & Charles, P. A. 1983, *ApJ*, 269, 212

Kahn, S. M., Gorenstein, P., Harnden, J. F. R., & Seward, F. D. 1985, *ApJ*, 299, 821

Kanbach, G., et al. 1980, *A&A*, 90, 163

—. 1994, *A&A*, 289, 855

Kargaltsev, O. 2004, PhD thesis, The Pennsylvania State University

Kaspi, V. M., Roberts, M. S. E., & Harding, A. K. 2006, in Compact stellar X-ray sources, ed. W. H. G. Lewin & M. van der Klis, 279–339

Kellogg, E., Tananbaum, H., Harnden, J. F. R., Gursky, H., Giacconi, R., & Grindlay, J. 1973, *ApJ*, 183, 935

Kennel, C. F., & Coroniti, F. V. 1984a, *ApJ*, 283, 694

—. 1984b, *ApJ*, 283, 710

Knight, F. K., Matteson, J. L., Peterson, L. E., & Rothschild, R. E. 1982, *ApJ*, 260, 553

LaMassa, S. M., Slane, P. O., & De Jager, O. C. 2008, *ApJ*, 689, L121

Landolt, A. U. 2009, *AJ*, 137, 4186

Large, M. I., Vaughan, A. E., & Mills, B. Y. 1968, *Nature*, 220, 340

Larson, M. B., & Link, B. 2002, *MNRAS*, 333, 613

Lasker, B. M. 1976, *ApJ*, 203, 193

Levine, A. M., et al. 1984, *ApJS*, 54, 581

Lewis, D., Dodson, R., McConnell, D., & Deshpande, A. 2002, in Neutron Stars in Supernova Remnants, Vol. 271, *ASP. Conf. Ser.*, ed. P. O. Slane & B. M. Gaensler, 191

Longair, M. S. 1994, Volume I: Particle, photons and their detection (Cambridge University Press)

Lyne, A. G. 1987, *Nature*, 326, 569

Manchester, R. N. 1987, *A&A*, 171, 205

Manchester, R. N., Hobbs, G. B., Teoh, A., & Hobbs, M. 2005, *AJ*, 129, 1993

Mangano, V., Massaro, E., Bocchino, F., Mineo, T., & Cusumano, G. 2005, *A&A*, 436, 917

Manzali, A., De Luca, A., & Caraveo, P. A. 2007, *ApJ*, 669, 570

Markwardt, C. B., & Ögelman, H. 1995, *Nature*, 375, 40

Markwardt, C. B., & Ögelman, H. B. 1994, in *BAAS*, Vol. 26, 871

Markwardt, C. B., & Ögelman, H. B. 1997, *ApJ*, 480, L13

Mason, K. O., & Culhane, J. L. 1978, *MNRAS*, 185, 673

Mattana, F., et al. 2011, *ApJ*, 743, L18

McGee, R. X., Slee, O. B., & Stanley, G. J. 1955, *Aust. J. Phys.*, 8, 347

McKee, C. F. 1974, *ApJ*, 188, 335

Mészáros, P. 1992, High energy radiation from magnetized neutron stars (Chicago: The University of Chicago Press)

Mignani, R. P., De Luca, A., Kargaltsev, O., Pavlov, G. G., Zaggia, S., Caraveo, P. A., & Becker, W. 2003, *ApJ*, 594, 419

Miller, E. W. 1973, *PASP*, 85, 764

Milne, D. K. 1968a, *Aust. J. Phys.*, 21, 201

—. 1968b, *Aust. J. Phys.*, 21, 501

—. 1980, *A&A*, 81, 293

—. 1995, *MINRAS*, 277, 1435

Milne, D. K., & Manchester, R. N. 1986, *A&A*, 167, 117

Minkowski, R. 1941, *PASP*, 53, 224

Moore, W. E., & Garmire, G. P. 1975, *ApJ*, 199, 680

Mori, K., Burrows, D. N., Hester, J. J., Pavlov, G. G., Shibata, S., & Tsunemi, H. 2004a, *ApJ*, 609, 186

Mori, K., Hailey, C. J., Paerels, F., & Zane, S. 2004b, *Adv. Space Res.*, 33, 503

Nasuti, F. P., Mignani, R., Caraveo, P. A., & Bignami, G. F. 1997, *A&A*, 323, 839

Ng, C.-Y., & Romani, R. W. 2004, *ApJ*, 601, 479

Nishikida, K., et al. 2006, *ApJ*, 644, L171

Nolan, P. L., et al. 2012, *ApJS*, 199, 31

Ögelman, H., Koch-Miramond, L., & Auriere, M. 1989, *ApJ*, 342, L83

Ögelman, H., & Zimmermann, H.-U. 1989, *ApJ*, 214, 179

Padmanabhan, T. 2001, Volume II: Stars and stellar systems (Cambrige University Press)

Pasachoff, J. M. 2002, Astronomy: from the earth to the Universe, 6th ed. (Belmont: Brookes and Cole)

Pavlov, G. G., Teter, M. A., Kargaltsev, O., & Sanwal, D. 2003, *ApJ*, 591, 1157

Pavlov, G. G., Zavlin, V. E., Sanwal, D., Burwitz, V., & Garmire, G. P. 2001, *ApJ*, 552, L129

Pellizzoni, A., et al. 2010, *Science*, 327, 663

Phillips, A. C. 1997, The physics for stars (New York: John Wiley & Sons)

Poveda, A., & Woltjer, L. 1968, *AJ*, 73, 65

Pravdo, S. H., Becker, R. H., Boldt, E. A., Holt, S. S., Serlemitsos, P. J., & Swank, J. H. 1978, *ApJ*, 223, 537

Pravdo, S. H., et al. 1976, *ApJ*, 208, L67

Qiao, W.-F., Zhang, L., & Fang, J. 2009a, *RAA*, 9, 449

—. 2009b, *RAA*, 9, 449

Radhakrishnan, V., Cooke, D. J., Komesaroff, M. M., & Morris, D. 1969, *Nature*, 221, 443

Richmond, M. 2012, http://spiff.rit.edu, [accessed: 6 September 2012]

Rishbeth, H. 1958, *Aust. J. Phys.*, 11, 550

Romani, R. W., Kargaltsev, O., & Pavlov, G. G. 2005, *ApJ*, 627, 383

Rybicki, G. B., & Lightman, P. A. 1979, Radiative processes in astrophysics (New York: John Wiley & Sons)

SAAO. 2012, http://www.saao.ac.za/facilities/telescope [accessed: 1 October 2012]

Sankrit, R., Shelton, R. L., Blair, W. P., Sembach, K. R., & Jenkins, E. B. 2001, *ApJ*, 549, 416

Schawinski, K., et al. 2008, *Science*, 321, 223

Seeds, M. A., & Backman, D. E. 2008, Astronomy the solar system and beyond, 6th ed. (Belmont: Brookes and Cole)

Sefako, R. R. 2002, PhD thesis, Potchefstroomse Universiteit vir Christelike Hoër Onderwys

Sefako, R. R., & De Jager, O. C. 2003, *ApJ*, 593, 1013

Seward, F. D., Burginyon, G. A., Grader, R. J., Hill, R. W., Palmieri, T. M., & Stoering, J. P. 1971, *ApJ*, 169, 515

Shibanov, Y. A., Koptsevich, A. B., Sollerman, J., & Lundqvist, P. 2003, *A&A*, 406, 645

Shull, J. P. 1983, *ApJ*, 269, 218

Smith, A. 1978, *MNRAS*, 182, 39

Strickman, M., De Jager, O., & Harding, A. 1996, *A&A*, 120, C449

Strickman, M. S., Harding, A. K., & de Jager, O. C. 1999, *ApJ*, 524, 373

Tayler, R. J. 1994, The stars: their structure and evolution (Cambridge University Press)

Thompson, D. J., Fichtel, C. E., Kniffen, D. A., & Ögelman, H. B. 1975, *ApJ*, 200, L79

Turatto, M. 2003, in Supernovae and Gamma-Ray Bursters, Vol. 598, *Lecture Notes in Physics, Berlin Springer Verlag*, ed. K. Weiler, 21–36

Ulmer, M. P., Purcell, W. R., Wheaton, W. A., & Mahoney, W. A. 1991, *ApJ*, 369, 485

Van den Bergh, S., Marscher, A. P., & Terzian, Y. 1973, *ApJS*, 26, 19

Van den Bergh, S., & McClure, R. D. 1994, *ApJ*, 425, 205

Van der Swaluw, E., Achterberg, A., & Gallant, Y. A. 2001, in Young Supernova Remnants, Vol. 565, *AIP Conf. Ser*, ed. S. S. Holt & U. Hwang, 379–382

Vink, J. 2012, *A&A*, 20, 49

Voshchinnikov, N. V., Molster, F. J., & The, P. S. 1996, *A&A*, 312, 243

Wakely, S., & Horan, D. 2012, http://tevcat.uchicago.edu, version 3.400 [accessed: 1 September 2012]

Wallace, P. T., et al. 1977, *Nature*, 266, 692

Weiler, K. W., & Panagia, N. 1978, *A&A*, 70, 419

—. 1980, *A&A*, 90, 269

Weiler, K. W., & Sramek, R. A. 1988, *A&A*, 26, 295

Wells, D. C., Greisen, E. W., & Harten, R. H. 1981, *A&A*, 44, 363

Willmore, A. P., Eyles, C. J., Skinner, G. K., & Watt, M. P. 1992, *MNRAS*, 254, 139

Wilson, R. W. 1963, *AJ*, 68, 181

Wilson, R. W., & Bolton, J. G. 1960, *PASP*, 72, 331

Yoshikoshi, T., et al. 1997, *ApJ*, 487, L65

—. 2009, *ApJ*, 702, 631

Zhang, L., Chen, S. B., & Fang, J. 2008, *ApJ*, 676, 1210

Zhang, L., & Yang, X. C. 2009, *ApJ*, 699, L153